From Gaseous Discs to Stellar Donors: A Spectroscopic Study of Accreting White Dwarfs with Companions Across Diverse Natures

by

Sergio Humberto Ramírez Ramírez

Thesis

Submitted to the University of Warwick

for the degree of

Doctor of Philosophy

Department of Physics

August 13, 2026

THE UNIVERSITY OF WARWICK

Contents

Acronyms

AGB Asymptotic Giant Branch. 4, 7, 15, 16, 36

AML Angular Momentum Loss. 13, 27–29, 31, 32

BD+WD Brown Dwarf+White Dwarf. 24, 32, 33, 124

BOA Bright Object Aperture. 45, 47

CEE Common Envelope Evolution. 14–16, 18, 26, 32, 33

CEW Cumulative Equivalent Width. 50

COS Cosmic Origins Spectrograph. viii, 45, 46, 77, 124

CV Cataclysmic Variables. 18–20, 23, 25–29, 31–33, 44, 50, 52, 62, 124, 125

DN Dwarf Novae. 19, 22, 58

ESPRESSO Echelle SPectrograph for Rocky Exoplanets and Stable Spectroscopic Observations. 47, 49

FAP False Alarm Probabilityy. 51

FUV Far-Ultraviolet. 45, 46

GR Gravitational Radiation. 27, 29, 32

HB Horizontal Branch. 4

HR Hertzprung Russel. 3, 4

HST *Hubble Space Telescope*. 45, 124

MB Magnetic Braking. 27–30

MEM Maximum Entropy Method. 55, 56

MS Main-Sequence. 2, 3, 14, 16, 18, 25, 26, 29, 30, 32, 34, 36, 124

NUV Near-Ultraviolet. 45

PCEB Post-Common Envelope Binaries. 15, 16, 25, 26, 32

PSA Primary Science Aperture. 45, 47

RGB Red Giant Branch. 4, 15, 16

RLOF Roche Lobe Overflow. 12, 18, 33

SAP Super Active Phase. 61

SED Spectral Energy Distribution. 66

SGB Subgiant Branch. 3, 15

UT Unit Telescope. 47, 48

UV Ultraviolet. 29, 38, 43, 45

VLT Very Large Telescope. 47, 48

WD White Dwarfs. 1, 2, 8, 9, 16–19, 21, 25–27, 29, 31–34, 36–45, 49, 50, 52, 58, 59, 61, 62, 124–126

List of Tables

List of Figures

Acknowledgments

I find writing the acknowledgments a herculean task. If I were to list the amount of people that generously offered their support throughout this experience, I'd be forced to write a few volumes, far exceeding the content of this Thesis. Despite knowing I'm destined to fail in such endeavour, I must still try.

There is absolutely no way I could have completed this work without the support, patience and mentorship from my supervisor, Boris T. Gänsicke. For some reason I have never had the courage to ask, he decided to take a bet on me, multiple times. I thank him for that trust. Through him, this work received funding from the European Research Council (ERC) under the European Union's Horizon 2020 research and innovation programme (Grant agreement No. 101020057).

I am very thankful to the members of the Department of Physics at the University of Warwick, in particular the Astronomy and Astrophysics group, for having created such a welcoming environment. In particular I thank my feedback supervisor, Dimitri Veras, for kindly providing support whenever I required. I also thank my Thesis examiners: Danny Steeghs and Stuart Littlefair, whose feedback greatly improved the content of this work. I unfortunately only had the chance of a few brief conversations with late professor Tom Marsh, but without his pioneering work on Doppler Tomography, I rather doubt I would have come to Warwick. I have much respect and admiration for his legacy.

I must list a few of the many collaborators (and friends) I had the pleasure of working with and learning from: Odette Toloza, Christopher Manser, Anna Pala, Snehalata Sahu, Timothy Cunningham, Kendall Ackley, Marina Lafarga Magro, Diogo Belloni, Andrew Swan, Ingrid Pelisoli, James Munday, Mairi O'Brien, Nicola

Gentile Fusillo, Amornrat Aungwerojwit, Juan Venancio Hernandez Santisteban, Juan Echevarría, among many others. Plenty were the times when they would drop their work to help me on my own. Many thanks.

I had the amazing fortune of sharing many a moment with a few other members of the department: Robert (the Bruce) Airey, Ioannis Apergis, Isobel (the Champ) Lockley, Eoin Haigney, Morgan (M.P.) Mitchell, James Blake, Jorge Fernández Fernández, Cameron Kelahan, Tafadzwa Zivave, Jamie Williams (thank you for that last-minute drive), Azib Norazman, Gareth Jones, Ben (Nevis) Davies, Cis Lagae, Matt Christensen, Óscar Barragán. From the bottom of my heart, thank you for all the laughs, heartfelt conversations and memories that I so fondly cherish.

For those with whom I would sometimes spend 25 hours per day, the gang of mischief: Cristina Madurga (Madurga) Favieres, Paula Izquierdo Sanchez, Rafael Martinez Brünner, Marcelo Aron Fetzner Keniger, Felipe Lagos Vilches, Phineas Whitlock, Laura Guzmán. Thank you for having my back in times of hardship. Thank you for the patience and unconditional friendship.

Now, the results in this work are fully reported in English, however, I must briefly switch to Spanish, begging the reader's indulgence.

A mis amigos en la gran ciudad: Julio Izquierdo y Eduardo Conde, Jazmín Tapia, Jorge Betancourt, Emmanuel Cruz. A pesar del tiempo y lejanía, ahí siguen.

A mis amigos en Tijuana (Dime con quién andas y te diré quién eres): Francisco Tiscareño, Orlando Sarmiento, Omar Gudiño, Javier Ramos, Arturo (Mochis) Vega, Jubal Lizárraga (buen colega de observaciones remotas), Ernesto Meza, Gabriel Velazquez, César López, Joel Espinoza, Miguel Reyna. Sepan todos que camino entre gigantes.

A los que ahora listo les agradezco que, aún a la distancia, están pendientes de mí: Paulo Carrillo, Óscar Cortés, Juan Pablo Cabezas, Kim Hegger, Maite Mañana, Delia Fleury, Rossana Torres, Alejandro Aviña, Néstor López. Los llevo siempre cerca.

En especial quiero agradecer a Rebecca Meadowcroft, por su cariño y apoyo incondicional, y por su actitud contagiosa de enfrentar la vida con una sonrisa; y a su familia, por hacerme sentir que aquella lejana nación, quizá no es tan lejana.

A mi familia, de esa incansable estirpe, con origen en las sierras de Durango, que de inmediato se percibe en mi mamá y sus hermanas, mis tías. Son bravas todas, pero al mismo tiempo tiernas. Protectoras de los suyos: Irene, Sara, Yoly, Elsa, Pati. Nunca nos dejen.

A mis tíos, de personalidad estoica pero divertida: Jorge, Walter, Jaime. Gracias por su guía.

A mis primos hermanos, que tienen más de hermanos que de primos: Zayra, Óscar, Víctor, Marko, Shantal, Talissa, Armenta, Kevin, Sasha, Markitos. Me es díficil no poder verlos tanto como quisiera.

A mi abuela Tina, que se encarga de que nos lluevan bendiciones, y a mi abuelo Dimas, que se nos adelantó ya hace algunos años; cuánto lo extraño. Los quiero mucho.

A mi papá, de sonidos iguales, pero de caminos distintos. Estaría orgulloso. A mi mamá, Imelda, que siempre lo entrega todo por nuestra causa; y mi hermano Carlo, menor en edad, pero mayor en ingenio. Ustedes son los pilares de mi vida.

Sin los aquí mencionados, y otros aparte que seguro escapan mi memoria, no habría logrado esta y otras tantas ambiciones mías. Gracias por tanto.

Here end the much needed paragraphs I would have struggled to write outside the realms of that language I call my own. Thank you, diligent reader, for your understanding. We may now proceed to review the fruits of my hard labour.

Declarations

I submit this thesis to the University of Warwick graduate school for the degree of Doctor of Philosophy. This thesis has been composed by myself and has not been submitted for a degree at another University.

An appreciable quantity of this thesis includes material from papers published, submitted or in preparation written by myself which are detailed below:

- Chapter 3: Ramírez, S. H., Gänsicke, B.T., Sahu, S., Belloni, D., Pala, O., Koester, D., Toloza, O., Lagos-Vilches, F. "V3101 Cyg: A Cataclysmic Variable Born with a Brown Dwarf Donor" (Submitted to Nature Astronomy)
- Chapter 4: Ramírez, S.H., Gänsicke1, B.T., Koester, D., Lafarga, M., Gentile-Fusillo, N.P., "ESPRESSO observations of the debris-accreting white dwarf WD 0141–675", MNRAS, 539, 2884.
- Chapter 5: Ramírez, S.H., Boris Gänsicke1, B.T., Manser C.J., Gentile-Fusillo, N.P., O'Brien, M., in preparation for submission to MNRAS

The work presented was carried out by the author except in the cases outlined below:

- Chapter 3: The white dwarf atmosphere models were computed by Boris Gänsicke and Detlev Koester. The white dwarf spectroscopic fitting was performed by Snehalata Sahu and Anna F. Pala. The abundance measurements were conducted by Snehalata Sahu and myself. The MESA modelling was performed by Diogo Belloni. The observations were reduced by both Odette Toloza and myself. Boris Gänsicke and Felipe Lagos-Vilches performed the disc emission line modelling.

- Chapter 4: The white dwarf atmosphere models and spectroscopic fit were computed by Boris Gänsicke and Detlev Koester. The reduction of the ESPRESSO observations was performed by Marina Lafarga, and the removal of telluric lines by Nicola Gentile-Fusillo.

- Chapter 5: A considerable set of observations were compiled and reduced by Chris Manser from spectroscopy published in (Dennihy et al., 2018), Manser et al. (2016a) and Manser et al. (2019). Follow-up X-Shooter observations were obtained by myself as P.I., which were reduced by Mairi O'Brien and Nicola Gentile-Fusillo.

Abstract

Accreting white dwarfs are an excellent laboratory to study interaction, dynamics and evolution of binaries and planetary systems. Three cases are showcased in this thesis:

The first case, V3101 Cyg consists of a cataclysmic variable that defies the standard evolutionary channel. HST spectroscopy allowed a direct measurement of its white dwarf parameters, which in particular yielded a very low mass value ($M_{\rm wd} \simeq 0.47\,{\rm M}_{\odot}$). Combining these measurements with the published mass ratio, implies a donor star mass well-below the hydrogen burning limit ($M_{\rm bd} \simeq 0.041\,{\rm M}_{\odot}$). MESA models show that this object likely descends from a detached brown dwarf plus white dwarf binary, making it the first confirmation of this evolutionary channel.

The second case was a study of the first alleged astrometric detection (albeit retracted) of a white dwarf planet: WD 0141–675. Using high-resolution, time-resolved ESPRESSO spectroscopy, I performed two independent period search studies on this object: Radial velocity and a violet-to-red ratio analysis. They reveal a tentative periodic signal of $P_{\rm orb} \simeq 16\,{\rm d}$, independently agreeing within their uncertainties, with half the period of the astrometric planet candidate. Combined with existing infrared photometry, our results imply possible solutions to the mass function within the planetary regime. I argue that despite the retraction, a *JWST* infrared constraint on the possible companion to WD 0141–675 remains of interest.

The last case is a small set of three white dwarfs harbouring gaseous debris discs. These systems provide evidence of planetesimals that have migrated inwards within the tidal disruption radius. So far only two of the $\sim$22 known WD gaseous discs have constraints on their precessional periods and have been previously mapped with Doppler Tomography. Owing to a long-term observational campaign, I include a new member to this small sample by producing the first Doppler map of SDSS J1043+0855, with a measured precessional period of $\simeq$4.7 yrs. I also updated the precession periods and tomography of the two previously characterised discs. Consistent with earlier findings, our tomography shows asymmetric emission, suggestive that these structures are common within the gas disc population. Such emission has been explained as the interplay of an embedded planetesimal with the dust debris disc. Therefore, a diversity of orbital architectures would naturally explain the wide range of found precessional periods ($\sim$1.2–25 yrs).

These results, laid out in three Chapters, show how standard spectroscopic methods are useful to constrain evolutionary models across sub-fields of accreting white dwarf systems: from cataclysmic variables, to planetesimals and gaseous discs.

Chapter 1

Introduction

"The report of my death was an exaggeration."

Mark Twain

White Dwarfs (WD)s, the endpoint of most main-sequence stars, have often been characterised as dead stars (Limbach et al., 2025a). This is true in the sense that nuclear fusion in their cores has ceased, but the physical processes they experience, such as the emergence of magnetic fields from their interiors (Camisassa et al., 2024), to the interruption of the cooling process for up to billions of years (Bédard, 2024), beckon, at the very least, a *last gasp* in their stellar lifetimes. A certain vitality is even more apparent in binary contexts, whereby these stellar embers are subjected to a reheating due to mass transfer (Townsley & Gänsicke, 2009; Ivanova & Taam, 2004); thermonuclear runaways in the envelope that rejuvenate the WD (Truran et al., 1977); mergers that completely reset the cooling age-clock (Coutu et al., 2019; Sala et al., 2026); and even pushed to highly energetic supernovae explosions (Blondin, 2026). And while the habitable zone of WDs can potentially sustain life (Shields et al., 2025), they have often been found draining it away from a plethora of mass donors: planetesimals that become ground down to gas (Manser et al., 2020) and dust (Swan et al., 2019); rocky minor planets (Vanderburg et al., 2015); giant gas planets (Gänsicke et al., 2019), brown dwarfs (Hernández Santisteban et al., 2016), main-sequence companions (Pala et al., 2020), red giants (Planquart et al., 2025), and even degenerate and semi-degenerate objects (Green et al., 2020).

This diversity in companion types and the high-density nature of WDs, makes them the perfect laboratory to study accretion physics, and binary and planetary evolution. However, despite the numbers and variety of confirmed WDs (Gentile Fusillo et al., 2019), considerable gaps remain, in particular, in the theory of evolution of WD binary (Nelemans & Tout, 2005; Ivanova et al., 2013) and planetary (Veras, 2021) systems. Hand in hand with big data studies, characterisation of individual objects remains a paramount endeavour to impose constraints on the theoretical models. In this spirit, three cases of WDs with companions of diverse nature were studied in this Thesis; which despite their differences, were spectroscopically characterised with standard methods. In this Introduction Chapter, I give a general framework to understand WD accreting systems, before moving on to the contributions made towards the field in the following Chapters. I am confident the reader will find this work a small but clear illustration that – even if linguistic purists were to dictate WDs are dead – their rich field of study is most certainly not.

1.1 White Dwarf Stars

Under standard stellar evolution, low and intermediate mass ($\lesssim 10\,\mathrm{M}_\odot$) stars will end their lives as WDs. This encompasses an overwhelming 97% of stars in the Milky Way (Althaus et al., 2010). In particular, when in close binary systems, their dense compact structure makes them optimal laboratories for the study of accretion physics and the measurement of planetary abundances. In this Section I will give a brief overview on (1) the journey a star must follow after the main sequence to become a white dwarf and (2) the general characteristics of white dwarfs. This will set the working framework for the following Sections that discuss white dwarfs in binary and planetary systems. For a detailed review on the physical processes in white dwarfs see Saumon et al. (2022).

1.1.1 Formation Path

The defining characteristic of a Main-Sequence (MS) star is hydrogen burning in the core. The time spent in this stage is critically dependent on the mass, with the more massive stars having a faster hydrogen consumption. As an example, a $1\,\mathrm{M}_\odot$ star spends $\sim 1 \times 10^{10}$ yrs on this stage, whereas a $5\,\mathrm{M}_\odot$ exhausts its core hydrogen in $\sim 7 \times 10^{7}$ yrs (Iben, 1967). Analogously, the post-main sequence evolutionary channels are also largely shaped by mass, with considerable changes already observed between $1\,\mathrm{M}_\odot$ and $5\,\mathrm{M}_\odot$ stars.

This section is intended only as a general outline of the processes experienced by low and intermediate stars ($M \lesssim 10 - 12\,\mathrm{M}_\odot$, Siess (2007)), bound to become white dwarfs. However, for a detailed description of various evolutionary pathways see Carroll & Ostlie (1996).

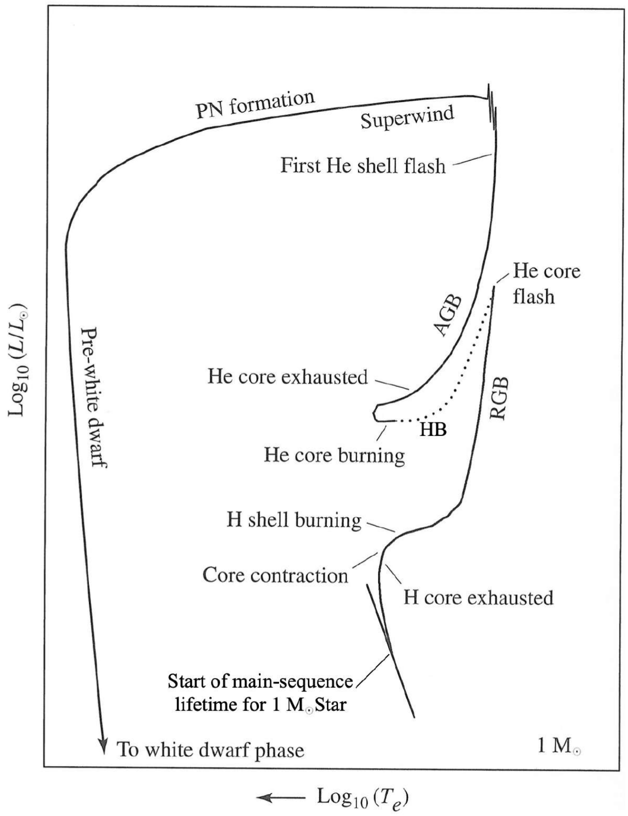

Figure 1.1: HR diagram showing the evolutionary stages of a $1M_\odot$star. Figure taken from Carroll & Ostlie (1996).

The MS lifetime ends when the hydrogen in the stellar interior becomes depleted. The star then begins to gravitationally collapse increasing the temperature of the core due to Kelvin-Helmholtz contraction[1](Freedman & Kaufmann, 2002).

The increase in temperature in the core triggers the ignition of hydrogen fusion in the surrounding shell. The photon diffusion rate limits the energy that can be transported by means of radiation, which is exceeded by the energy production of the nuclear reactions. This causes the outer layers to expand, resulting in a cool-down of the effective temperature, which translates in a redward evolution along the so-called Subgiant Branch (SGB) on the HR diagram, as shown in Fig. 1.1. This is a short-lived phase with timescales of the order of $\sim 10^7 - 10^9$ yrs.

The helium produced in the shell hydrogen burning sinks down to the core, increasing its pressure and density, causing it to contract further and heat up as it gains mass. The heat flows outward escalating the hydrogen burning rate in the

[1]Gravitational potential energy converted into thermal energy.

surrounding shell and making the outer layers expand to several AU. The luminosity now increases substantially and the star climbs vertically in the HR diagram along the Red Giant Branch (RGB), which lasts $\sim 10^7 - 10^9$ yrs (Iben, 1967).

Stars with initial masses of $M \lesssim 0.7\,\mathrm{M}_\odot$ are not expected to reach the temperature required for helium fusion into carbon and oxygen, so when shell hydrogen-burning ceases they leave behind a degenerate core, bound to become a helium white dwarf with $M \lesssim 0.4\mathrm{M}_\odot$. Nonetheless, the time for these objects to leave the main sequence exceeds the age of the Milky Way.

Stars with $0.7\,\mathrm{M}_\odot \lesssim$ M $\lesssim 1.8\,\mathrm{M}_\odot$ continue to experience core collapse until it becomes strongly degenerate. This implies that the ideal gas relationship no longer holds and the core does not expand following an increase of temperature. When the core heats enough to ignite helium-burning via the triple alpha process ($\simeq 10^8$ K), energy release happens suddenly and explosively, in what is known as the *helium flash*. Despite the name, however, most of the energy budget is expended in lifting the degeneracy. In contrast, stars with masses greater than $\simeq 1.8\,\mathrm{M}_\odot$ do not become degenerate due to the higher temperatures and instead experience gradual core helium-burning.

Once the core expands, the hydrogen-burning shell migrates outward to lower pressure regions reducing the hydrogen burning rate. The envelope contracts and the star settles in a new thermal equilibrium. The compression of the shell caused from the star's contraction causes the energy output to rise again increasing the surface temperature. With both core helium burning and shell hydrogen burning occurring in conjunction, the star becomes hotter at a constant radius, moving along the Horizontal Branch (HB) in the HR diagram. Stars traverse the HB in $\sim 10^8$yrs (Comins & Kaufmann, 1999).

Eventually helium burning ceases in the core, causing it to contract and triggering a new stage of helium burning in the surrounding shell, along with hydrogen burning in an outer shell. Analogous to the RGB, the energy output again causes the outer layers to expand substantially, with the star ascending vertically a second time along the so-called Asymptotic Giant Branch (AGB).

At this point the star develops an inert and degenerate carbon-oxygen core, with stars of $M \lesssim 8\mathrm{M}_\odot$ never reaching high enough temperatures to ignite further fusion in the stellar interior. Gradually, the outer layers become ejected, forming a planetary nebula. The exposed core contracts, thus heating up and migrating leftward across the HR diagram. With absent thermonuclear reactions the core becomes a cooling stellar ember; what we know as a white dwarf. If, however, the main sequence mass was in the range of $8\mathrm{M}_\odot \lesssim M \lesssim 12\mathrm{M}_\odot$, then carbon burning does occur in the core. And as with the past stages of core burning, a new shell burning period ensues along with yet another red giant phase, with the eventual ejection of the outer layers. Thus leaving behind an oxygen-neon white dwarf.

1.1.2 General Properties

Mass-Radius Relationship

Given the absence of nuclear fusion in the core of white dwarfs, gravitational collapse is only counterbalanced by electron degeneracy pressure. Thus, employing Fermi-Dirac statistics, the equation of state was modelled by Chandrasekhar (1931), who assumed a white dwarf as a self-gravitating gaseous sphere (known as a polytrope):

$$P \propto \rho^{1+n} \tag{1.1}$$

Where P and ρ are the pressure and density, respectively, and n represents the polytropic index. White dwarfs supported by non-relativistic electrons can be described by a polytropic index of $n = 3/2$. This leads to the well-known mass-radius relation of white dwarfs :

$$R \propto M^{-1/3} \tag{1.2}$$

On the other hand, by assuming a completely relativistically degenerate configuration (corresponding to polytropic index of $n = 3$), Chandrasekhar derived an upper limit on the mass of a stable white dwarf. The so-called *Chandrasekhar limit* depends on the white dwarf internal structure, but for the particular case of a fully ionised carbon-oxygen gas, the canonical limit stands at $M_{\rm Ch} \simeq 1.4\,{\rm M}_\odot$(Chandrasekhar, 1935).

Mass distribution

Well below the *Chandrasekhar limit*, the typical white dwarf mass is of $\simeq 0.6{\rm M}_\odot$ (e.g. Koester et al., 1979; Kilic et al., 2020; O'Brien et al., 2024, Figure 1.2) and is composed of a degenerate carbon-oxygen core. However, low-mass white dwarfs $\simeq$0.4 are likely to have helium-cores instead. These objects would have had low-mass progenitors (M$\lesssim$0.6 ${\rm M}_\odot$) that would not have been able to fuse He into C and O in their interiors during the post-main sequence evolution (see Section 1.1.1). In isolation, the main sequence phase of these low-mass stars is expected to be longer than the age of the universe. Nonetheless as observed in Fig. 1.2, low-mass helium-core white dwarfs have indeed been identified. Such objects are explained via close

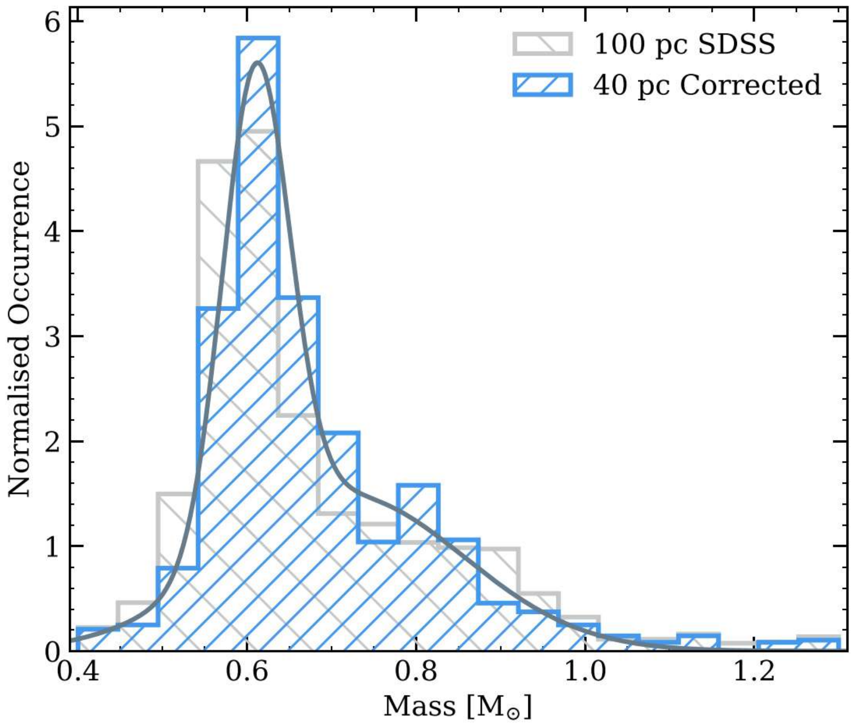

Figure 1.2: White dwarf mass distribution of the 40pc volume limited sample from *Gaia* DR3 (O'Brien et al., 2024), compared to the 100pc sample from SDSS (Kilic et al., 2020). Both distributions show a peak at a mass of $\simeq 0.6\,M_\odot$. Figure taken from O'Brien et al. (2024).

binary interactions (Iben & Livio, 1993; Marsh et al., 1995), whereby the companion would have stripped the outer layers of the white dwarf progenitor during its giant phase. On the opposite extreme, as remarked in Section 1.1.1, if a progenitor star mass lies above $\simeq 8M_\odot$, carbon fusion occurs in the core leading to ultra-massive oxygen-neon core white dwarfs ($M \gtrsim 1.1M_\odot$). Some of these O-Ne white dwarfs, at the high end of the mass distribution, are also expected to have been formed as a consequence of close binary evolution, via the merging of two carbon-oxygen white dwarfs.

Stratified Structure and Spectral Classification

These compact stellar remnants experience unique conditions of extreme density ($\rho \sim 10^6\,\mathrm{g\,cm^{-3}}$). This causes gravitational settling to take place in considerably shorter time-scales than the cooling age (e.g. Paquette et al., 1986a). Thus, these objects have pronouncedly stratified structures: in an ordinary white dwarf of $0.6\,M_\odot$,

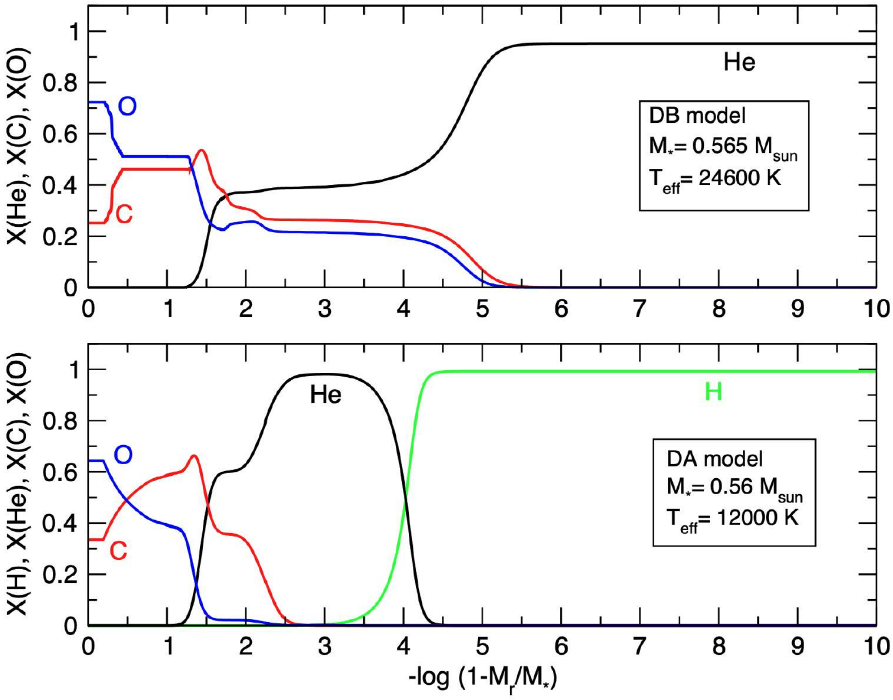

Figure 1.3: Stratified structure of a helium atmosphere white dwarf (DB, top) and a hydrogen atmosphere white dwarf (DA, bottom). Figure taken from Althaus et al. (2010).

99% of the mass is composed of a degenerate carbon-oxygen core, surrounded by a thin non-degenerate envelope of helium ($\simeq 0.01\,\mathrm{M}_\odot$), on top of which lies a thin *coating* of hydrogen ($\simeq 10^{-4}\,\mathrm{M}_\odot$) (Fig. 1.3, bottom panel). This structure gives rise to the so-called DA spectral type, that is, white dwarfs whose predominant features in the optical are the Balmer absorption lines.

The hydrogen-rich atmosphere, while predominant, is not universal. If the progenitor star experienced late thermal pulses at the end of the AGB, hydrogen fusion can be ignited in the top veneer (Herwig et al., 1999), exposing the helium shell underneath (Fig. 1.3, top panel). The dominant features in the spectra of helium-rich atmospheres are determined by the effective temperature: The hotter objects with $T_{\rm eff} \gtrsim 40\,000\,\mathrm{K}$ show mostly ionised helium transitions of He II, earning the DO spectral classification; the cooler counterparts in the range of $11\,000 \lesssim T_{\rm eff} \lesssim 40\,000$ display instead neutral He I absorption lines, and are classified as DBs.

As cautioned by Saumon et al. (2022), the spectral type and atmospheric composition are correlated but not equivalent. The spectral type only indicates the dominant species in the spectra. For example, Hydrogen-rich atmospheres below

$T_{\rm eff} \lesssim 5\,000\,{\rm K}$ do not display absorption features in the optical and are classified as having a DC spectral type. Further exemplifying this point are white dwarfs with Helium-rich atmospheres of $T_{\rm eff} \lesssim 11\,000\,{\rm K}$, that may not display absorption features, classifying as DCs; but may otherwise show the presence of detectable carbon since convection causes a dredge-up from the deep interior. The latter are classified as cool DQs; with the epithet coined to distinguish them from the so-called hot DQs ($\gtrsim 11\,000\,{\rm K}$), whose atmospheres are actually carbon dominated and form via double-white dwarf mergers (Dunlap & Clemens, 2015; Coutu et al., 2019). Finally, the DZ spectral type exhibit elements heavier than carbon, that have been linked to recent accretion of tidally disrupted planetesimals (e.g. Koester & Wolff, 2000; Jura, 2003; Gänsicke et al., 2019)

This comes to show that spectral types not only vary depending on the atmosphere temperature, but also the inherent chemical composition can change, thus altering the spectra (see Bédard, 2024, for a detailed review). The white dwarf temperature plays a protagonist role in this evolution, therefore, we must now turn our attention to the white dwarf cooling sequence.

Cooling Sequence

Despite the cessation of nuclear fusion in the interior of white dwarfs, these objects are extremely hot ($\simeq 120\,000\,{\rm K}$) due to the release of gravitational energy during the phases of contraction in the proto-white dwarf stellar core (D'Antona & Mazzitelli, 1990). At this stage the slow cooling processes set the pace for the structural evolution. The temperature decreases monotonically as a function of age, rendering white dwarfs as excellent cosmochronometers (Fontaine, 2001).

The early stages of white dwarf evolution are dominated by neutrino cooling (Chin et al., 1966; Savedoff et al., 1969). Neutrinos escape the central regions without interaction with the stellar plasma carrying significant amount of energy (Althaus et al., 2010). Neutrinos are formed in the denser central regions and do not interact with the stellar plasma. This effective energy sink ceases at a temperature of $\simeq 25\,000\,{\rm K}$. Below this threshold thermal cooling takes over with its efficiency depending on the radiative opacities of the envelope layers.

Further cool-down of the white dwarf causes the ions in the degenerate interior to undergo a phase transition and form a crystal lattice (Salpeter, 1961, Fig 1.4). This process occurs inside-out with a release of $\approx \frac{3}{2}k_{\rm B}T$ latent heat per ion (van Horn, 1968; Fontaine, 2001). The onset of cristallisation takes place between $\sim 0.5 - 5\,{\rm Gyr}$ of the cooling sequence, depending on the WD mass, lasting about $\sim 2\,{\rm Gyr}$ (see Fig. 1.4).

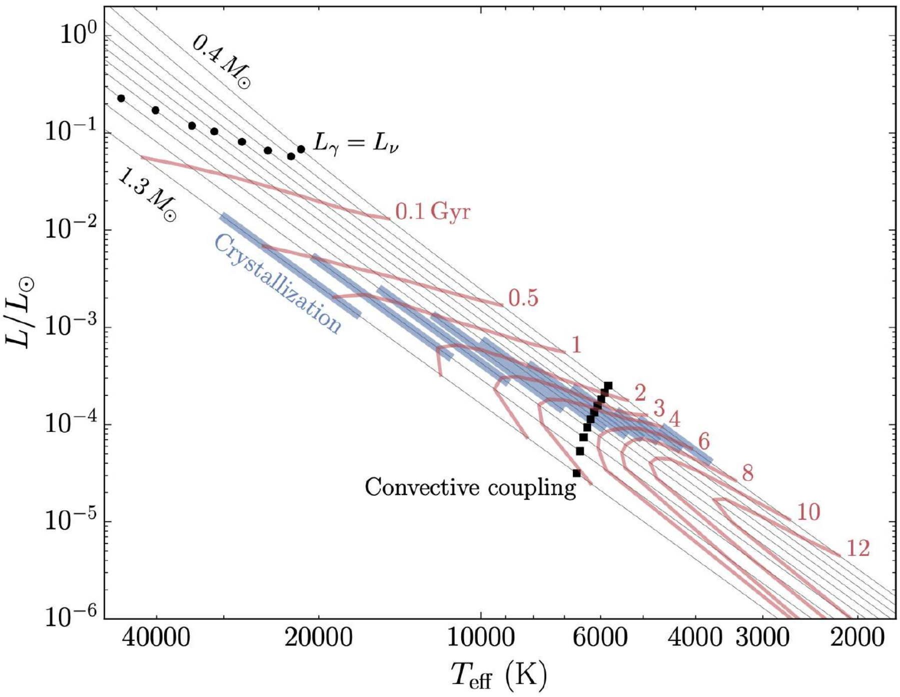

Figure 1.4: Cooling evolutionary tracks of C-O core white dwarfs for masses ranging from 0.4 to 1.3 $M_\odot$. Three important events in white dwarf evolution are marked: the end of neutrino cooling (black circles), crystallisation in the core (blue region) and convective coupling (squares). The red curves indicate isochrones with the labels in units of Gyr. It is worth noting that the age in all major events in the lifetime show a strong dependence on the white dwarf mass. Figure reproduced from Saumon et al. (2022).

Partial ionisation of hydrogen in H-rich white dwarfs cause convective instabilities to develop in the photosphere at temperatures of $\simeq 18\,000$ K. When the cooling decreases to $\simeq 6\,000$ K (after $\sim 2 - 6$ Gyr in the cooling sequence) the convective processes have extended past sub-photospheric layers all the way down to the degenerate interior. On the other hand, this so-called convective coupling occurs at temperatures of $\simeq 12\,000$ K in He-atmosphere white dwarfs (Rolland et al., 2018). Notably, energy release in this phase becomes dominated by convection.

As made evident in Fig. 1.4, the WD temperature reveals the age of the star, making these objects optimal cosmic clocks. Furthermore, as discussed in Section 1.3.5, the WD temperature in interactive binaries, such as Cataclysmic Variables, provides information on the average mass accretion rate, related to their evolutionary state. Our great reliance on this sequence makes it paramount to understand the phenomena that affect it.

1.2 Interacting WD Binaries

Volume-limited surveys have revealed that an overwhelming $\sim$ 50% of Sun-like FGK stars in the solar neighborhood ($\sim$ 25 pc) have at least one stellar companion (Duquennoy & Mayor, 1991; Raghavan et al., 2010; Offner et al., 2023). And while multiplicity fractions decrease at lower masses, even the low-mass population of M-dwarfs have a multiplicity fraction of ~20–25% (e.g., Winters et al., 2019).

The evolution of a double star is largely affected by the binary separation. When this exceeds $\simeq$ 10 au (e.g., Toloza et al., 2023), mass transfer is avoided and the components evolve independently as single stars. As outlined in Section 1.1.1, the more massive component will evolve faster through the nuclear phases, likely ending as a WD. Not only do these wide binaries never come in contact, but due to kicks from asymmetric mass loss of the WD progenitor, their separation tends to subtly widen (El-Badry & Rix, 2018).

On the other hand, if the initial binary separation lies below $\simeq$ 10 au, the components will influence each other's evolution via interactive processes. This shared evolution can ensue a plethora of outcomes. For example, giant stars stripped from their hydrogen envelope can halt mass growth of their helium core before helium burning occurs. This is the reason helium-core WDs are generally members of binary systems. Accreting stars can get rejuvenated and metal enriched and the mass gain can even alter the nature of their terminal evolutionary stage (Belloni & Schreiber, 2023a). Close binary interactions are a source of detectable gravitational waves, they can end as stellar mergers, or even culminate in supernovae events (e.g. Marchant, 2026).

In this Section, I will give a brief overview on the evolution mechanisms that these objects undergo, with an emphasis on the conditions that ultimately ensue an accreting WD component. These systems are optimal laboratories to understand high-energy phenomena and accretion processes, and present unique opportunities to delve into binary and even single star evolution. For a state-of-the-art review on the current theoretical understanding of accreting compact objects, the reader is referred to (Belloni & Schreiber, 2023a).

1.2.1 Roche Geometry

A good approximation to the behavior of binary star systems is made through the mathematical prescription of the Roche potential, which describes the gravitational potential in the co-rotating frame of the binary. Accounting for the sum of the gravitational potentials of both stars and the centrifugal potential, and assuming a

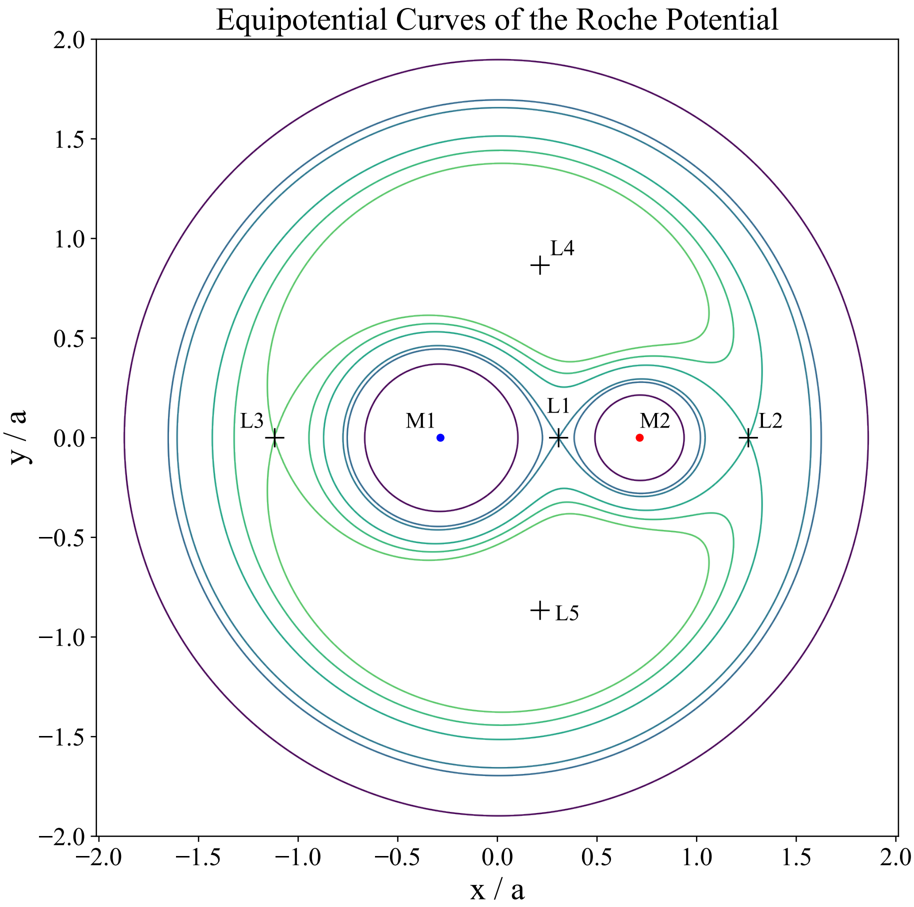

Figure 1.5: Roche geometry plotted for a mass ratio of q=M2/M1=0.4. The '+' symbols indicate the positions of the Lagrangian points (L1−L5), where a test mass experiences no force ($d\Phi/dx = 0$). The blue and red dots indicate the centre of mass of the primary (M1) and secondary (M2) components, respectively. The contours were plotted in Python following the `Wolfram` code developed by Bryant (2005).

distance between the centres of mass of a, the Roche potential is defined as (Pringle & Wade, 1985; Warner, 2003; Hellier, 2001):

$$\Phi_R = -\frac{GM_1}{(x^2+y^2+z^2)^{\frac{1}{2}}} - \frac{GM_2}{[(x-a)^2+y^2+z^2)]^{\frac{1}{2}}} - \frac{\Omega^2_{\rm orb}}{2}\left[(x-\mu a)^2+y^2)\right] \quad (1.3)$$

With $\mu = M2/(M1 + M2)$ and $\Omega_{orb} = 2\pi/P_{orb}$. Equation 1.3 is expressed in a Cartesian coordinate system (x,y,z).

The Roche equipotential curves, Φ_R = Const, depend only on the mass ratio $q = M2/M1$, and are scaled by the binary distance a. An example of the Roche equipotentials for $q = 0.4$ can be observed in Fig 1.5. The points where the potentials of the stars balance, i.e., $\partial\Phi_R/\partial x = 0$, are called the Lagrangian points.

Of particular importance is the equipotential curve that connects at the Lagrangian point L1. This curve defines the critical volumes known as Roche lobes. If a star expands and fills its respective Roche lobe, or if the orbit shrinks due to angular momentum loss and the Roche lobe shrinks, mass transfer will take place. This process is known as Roche-lobe overflow. An approximation (valid for $0.1 < q < 10$) to the distance from the center of mass of the WD to the inner lagrangian L1 is given by (Hellier, 2001):

$$R_{L_1} = a(0.500 - 0.227\ \log q) \tag{1.4}$$

It is also worth noting that the surface of a synchronously rotating star lies on $\phi_{\rm R} = const$, in other words, the shape of such star would be defined by the equipotential curves. Therefore, to approximate the star volume, it is sufficient to calculate the radius of a sphere containing the same volume as the Roche lobe (Eggleton, 1983) :

$$R_\star = \frac{0.49\, a\, q^{2/3}}{0.6q^{2/3} + ln(1 + q^{1/3})} \tag{1.5}$$

The Roche lobe geometry defines three types of mass transfer regimes:

(a) Detached binaries: The volume of both components is smaller than their respective Roche lobe, therefore no mass transfer occurs. However, interactions in the form of stellar winds and tides are still possible.

(b) Semi-detached binaries: One of the components fills its Roche lobe, and mass transfer happens through the L1 point. The so-called Roche Lobe Overflow (RLOF) has considerable effect in the evolution of the components.

(c) Contact binaries: Both stars fill an equipotential exceeding L1 (but not reaching L2) becoming wrapped in a common photosphere. Not only will there be transfer of mass between the components, but also heat exchange occurs.

1.2.2 Mass Transfer

As explained in the previous Section, if a binary component fills its Roche lobe, mass transfer will take place. Assuming a binary where M_1 is the mass of the accreting component (primary), M_2 the mass of the donor component (secondary), and a the binary separation, the systemic angular momentum can be expressed as (Hellier, 2001):

$$J = M_1 M_2 \left(\frac{Ga}{M}\right)^{\frac{1}{2}} \tag{1.6}$$

Where $M = M_1 + M_2$. Then, taking logarithmic differentiation we obtain:

$$\frac{\dot{a}}{a} = 2\frac{\dot{J}}{J} - 2\frac{\dot{M}_1}{M_1} - 2\frac{\dot{M}_2}{M_2} + \frac{\dot{M}}{M} \tag{1.7}$$

If conservative mass transfer ($\dot{M} = 0$) is assumed, that is, that all mass lost by one star is accreted by the other ($\dot{M}_1 = -\dot{M}_2$), then equation 1.7 can be rewritten as (King, 1988):

$$\frac{\dot{a}}{a} = 2\frac{\dot{J}}{J} - 2\frac{\dot{M}_2}{M_2}\left(1 - \frac{M_2}{M_1}\right) \tag{1.8}$$

$\dot{M}_2 < 0$, by definition. This implies that the binary separation increases ($\dot{a} > 0$) if the transfer of mass occurs from the less massive to the more massive component.

Now, the volume-averaged Roche lobe radius approximation of the donor is given by (Paczyński, 1971):

$$\frac{R_L}{a} = 0.462\left(\frac{q}{1+q}\right)^{1/3} \tag{1.9}$$

With $q = M_2/M_1$, as defined in Section 1.2.1. Logarithmic differentiation of Eq. 1.9, and then combining with Eq. 1.8 results in:

$$\frac{\dot{R}_L}{R_L} = 2\frac{\dot{J}}{J} - 2\frac{\dot{M}_2}{M_2}\left(\frac{5}{6} - q\right) \tag{1.10}$$

Assuming conservative mass transfer, Equation 1.10 defines two cases (Ritter, 1976):

(a) If $q \gtrsim 5/6 \sim 1$, the size of the Roche lobe is continually decreasing forcing the secondary to stay in contact with it. With the mass of the donor almost as large or larger than the accreting component, this scenario generally results in a runaway mass transfer event (Hellier, 2001).

(b) If $q \lesssim 5/6$, conservative mass loss causes the size of the Roche lobe to increase, thus detaching itself from the donor and cutting off the mass transfer event. However, as discussed in further detail in Section 1.3, the mass ratio in cataclysmic variables generally lies in this regime. Therefore, cataclysmic variables must experience Angular Momentum Loss (AML) in order to keep the Roche lobe in contact with the donor star and sustain stable mass transfer.

The stability of mass transfer depends strongly on the timescale in which the donor star adjusts its radius as a response to mass loss (Belloni & Schreiber, 2023a). Mass transfer will be stable if the donor with mass M_2, radius R_2 , and luminosity L_2, has a mass-loss rate ($t_{\dot{M}}$) that greatly exceeds the thermal timescale[2]($t_{\rm KH}$):

$$t_{KH} \sim \frac{GM_2^2}{R_2 L_2} << \frac{M_2}{\dot{M}_2} = t_{\dot{M}} \tag{1.11}$$

In the particular case of cataclysmic variables (Section 1.3), the mass-loss occurs at a rate of the order of the thermal timescale. This is sufficient to drive the MS donors out of thermal equilibrium and make them more bloated compared to their isolated counterparts (Knigge, 2006).

Further, in the extreme case where $t_{KH} >> t_{\dot{M}}$, mass transfer becomes unstable and proceeds instead on what is known as the dynamical timescale $t_{\rm dyn}$:

$$t_{KH} >> t_{\dot{M}} \sim t_{\rm dyn} \sim \left(\frac{R_2^3}{GM_2}\right)^{1/2} \tag{1.12}$$

This causes the donor to further expand and a runaway mass transfer process is triggered, engulfing the companion in a short-lived phase known as Common Envelope Evolution (CEE).

1.2.3 Common Envelope Evolution

A long-standing issue in binary evolution is to understand how is it possible that we observe compact objects in binary systems with separations of the order of $1\,\mathrm{R}_\odot$; far smaller than the radius of their giant progenitors ($\sim 100\,\mathrm{R}_\odot$, Postnov & Yungelson, 2014). The most widely accepted scenario is known as the CEE (Paczynski, 1976; Webbink, 1984; Hjellming, 1989). This is a short-lived phase ($\lesssim$ 1000 yrs) occurs after the most massive component leaves the MS and becomes a red giant filling its Roche lobe. This starts a phase of unstable mass transfer onto the less massive MS component. Since the thermal-timescale exceeds the mass transfer time-scale, the mass gainer component can also be driven out of thermal equilibrium, filling its Roche lobe. Regardless, the system becomes engulfed in a common envelope, which initiates a rapid inspiral towards the center of mass due to the exerted drag. If enough orbital energy is deposited into the envelope, it can be expelled from the system before a merger occurs (Ivanova et al., 2013). In the case of interest for this thesis, the more massive component, an intermediate/low-mass MS star,

[2]Also known as the Kelvin-Hemholtz timescale (Hellier, 2001; Warner, 2003)

emerges from the CEE as a He or CO white dwarf; whereas it is assumed that the evolutionary stage of the engulfed companion remains unaffected.

Observational (Shariat & El-Badry, 2026) and theoretical (e.g. Yarza et al., 2022, 2023; Gagnier et al., 2026) efforts have been carried out to better constrain CEE, which despite its cruciality, remains poorly understood. Modelling the outcome of this stage is computationally expensive due to the many physical processes involved and its short time-scale. To bypass this complexity a simplified analytical framework is used, the so-called *standard energy formalism* (Webbink, 1984; Livio & Soker, 1988; Iben & Livio, 1993). This prescription evaluates the change in orbital energy (ΔE_{orb}) caused by the CEE, and compares it with the energy required to eject the envelope, known as the binding energy E_{bind} (e.g. Ivanova et al., 2013):

$$E_{bind} = \Delta E_{\rm orb} = E_{\rm orb,i} - E_{\rm orb,f} = \frac{-Gm_1m_2}{2a_i} + \frac{Gm_{1,\rm c}m_2}{2a_i} \tag{1.13}$$

where a_i and a_f are the initial and final binary separations, m_1 and m_2 are the initial star masses and $m_{1,c}$ is the final mass of the star whose envelope became ejected. However, not all the orbital energy is used in the ejection of the envelope, thus, an efficiency parameter is introduced $\alpha_{\rm CE}$ (Tutukov & Yungelson, 1979). Furthermore, if the effect of the internal structure of the stars is also taken into account then a parameter λ (de Kool, 1990) is also included. Equation 1.13 is then rewritten as:

$$\frac{m_1 m_{1,\rm env}}{\lambda R_1} = \alpha_{\rm CE}\left(\frac{-Gm_1m_2}{2a_i} + \frac{Gm_{1,\rm c}m_2}{2a_i}\right) \tag{1.14}$$

where $m_{1,\rm env}$ is the mass of the ejected envelope. Constraining these parameters remains an on-going effort. Models compared against a large sample of Post-Common Envelope Binaries (PCEB) suggests low values for the efficiency parameter $\alpha_{\rm CE}$ $(0.2 - 0.3)$, with no indications for a dependence on the mass of the secondary nor the orbital period (Zorotovic et al., 2010). On the other hand, typical values for the structural binding energy parameter λ are within the range of $0.2 - 0.8$. This parameter is strongly dependent on the evolutionary stage and radius of the donor star. As it expands throughout the RGB, its λ parameter increases yielding much higher values of $\gtrsim 5$ for donors in the AGB phase, in other words, the binding energy decreases substantially in the latter phase (Dewi & Tauris, 2000). It has been argued that at the tip of the AGB the envelope becomes virtually unbound Chen et al. (2011), with envelope ejection occurring after an insignificant orbital decay (Nelemans et al., 2000). In contrast, the core of SGB stars is more compact, and therefore the ejection of the envelope would require a higher drain of orbital energy in this stage.

Another pivotal question remains unanswered: what is the minimum companion mass that could in principle survive engulfment? Hydrodynamical simulations suggest that companions with masses as low as $\sim 10\,\mathrm{M_J}$ can eject the envelope at the tip of the RGB avoiding a merger (Yarza et al., 2023), and as discussed above, this mass could potentially be even smaller if CEE starts in the AGB. Consistent results were found by Nelson et al. (2018) for sufficiently high WD masses. Observational agreement came with the recent detection of two eclipsing PCEBs, each composed of a white dwarf and a low-mass brown dwarf companion of $\sim 20\,\mathrm{M_J}$ (Parsons et al., 2025). As a matter of fact, CEE has even been theorised (Lagos et al., 2021) to explain the presence of the close-in planet ($\sim$6 $\mathrm{M_J}$) WD 1856+534 b (Vanderburg et al., 2020); requiring, however, an additional energy source to that drained from the orbit (Lagos et al., 2021), such as recombination, accretion, nuclear energy, enthalpy (Ivanova et al., 2013), or even jets (Sabach et al., 2017).

The above-mentioned question is particularly relevant for this thesis. As discussed in Chapter 3, the low masses of both the WD and substellar companion in V3101 Cyg ($\sim$0.47 and 0.041 $\mathrm{M_\odot}$, respectively) can help constrain CEE. And while this scenario is less likely to explain most planet accreting WDs (see Section 1.4 and Chapters 4 and 5), as was made evident by Lagos et al. (2021), it cannot be idly dismissed. Regardless, it is widely accepted that CEE is the likely culprit for the existence of accreting compact objects with stellar donors. I now turn my attention to a general classification of these objects.

1.2.4 Accreting White Dwarf Binaries

Binary compact stars are systems whereby at least one of the components has evolved past the MS and giant phases to become a compact object, be it a WD, neutron star or black hole. If the companion fills its Roche lobe and transfers matter onto the compact component, the system is then referred to as an accreting compact object. These objects are the keystones to understanding pivotal physical phenomena such as Type Ia supernovae, gravitational waves and X-ray and γ-ray bursts (Gänsicke et al., 2006a; Postnov & Yungelson, 2014; Webb, 2023; Belloni & Schreiber, 2023a). Initial separation, masses and composition generally determine the nature of the interactions between the components, leading to a plethora of distinct channels (e.g. Fig. 3 from Belloni et al., 2020). However, this Section is devoted to those resulting in a WD accretor (Fig. 1.6).

(a) Cataclysmic variables harbour a Roche-lobe filling low-mass MS donor, with typical accretion rates of $\sim 10^{-11} - 10^{-8}\,\mathrm{M_\odot yr^{-1}}$. The mode of accretion onto

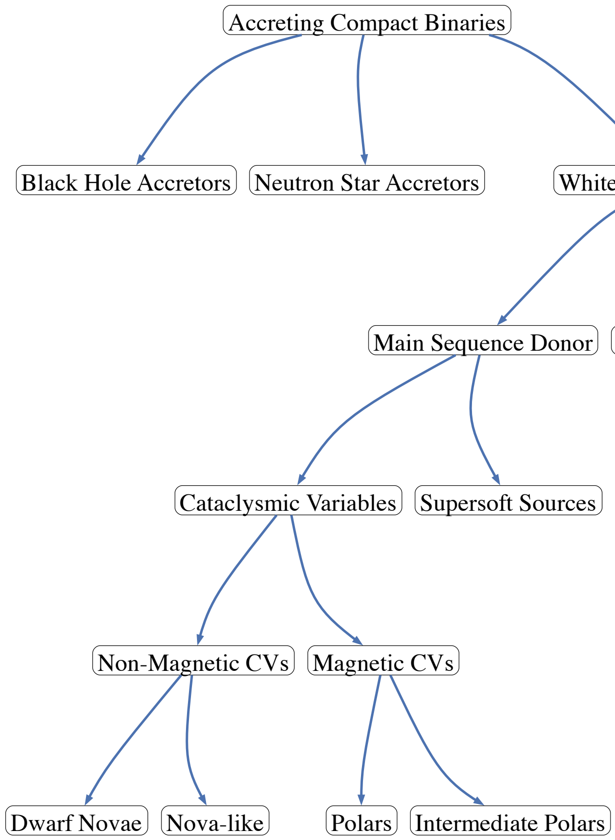

Figure 1.6: Tree Diagram of accreting compact binaries, particularly expanding on the branch of accreting WDs.

the white dwarf depends on the strength of the magnetic field, classifying them as either non-magnetic or magnetic cataclysmic variables (Hellier, 2001; Warner, 2003).

(b) Symbiotic stars are characterised by wind accretion onto a WD from a giant companion (Sokoloski, 2003). Symbiotics have orbital periods of the order of years. Some develop an accretion disc and show optical outbursts in decadal timescales. While they are sometimes thought as overgrown cataclysmic variables, they are not as well understood, given that their variability occurs in far longer timescales.

(c) Supersoft X-ray binaries are cataclysmic variable analogues with a high accretion rate ($\sim 10^{-7}\,\mathrm{M_{\odot}yr^{-1}}$), able to sustain quasi-steady hydrogen burning at the base of the accreted layer. In turn, the steady nuclear fusion generates supersoft x-ray emission (Long et al., 1981; van den Heuvel et al., 1992).

(d) AM CVn systems are similar in architecture to Cataclysmic variables, except that they are ultracompact and have very short periods (5−68 min). The WD accretes helium-rich material from a degenerate donor (He WD), or a semi-degenerate nuclear-evolved star (He star) (Solheim, 2010). The helium-rich nature makes the donor denser and hence more compact allowing the binary to exist at short orbital periods. The formation of these systems is through one or two CEE events, leaving them in a close-in but detached configurations. Gravitational waves then cause them to become semi-detached, eventually enabling stable RLOF (e.g. Green et al., 2020).

As the percipient reader may have noticed, all of these systems bear a resemblance in terms of architecture. How they relate (e.g. Schenker et al., 2002; Schenker, 2005; Belloni & Schreiber, 2023b), or what initial conditions ensue each outcome (Postnov & Yungelson, 2014) remain issues of ongoing research. And while an in-depth study of each of these classes is necessary to paint the complete picture, cataclysmic variables are a natural starting point. Indeed, they are the best-studied type of interacting compact binaries (Belloni & Schreiber, 2023a). This is because they are the most numerous. Therefore, volume-limited samples (Pala et al., 2020; Inight et al., 2021) enable strict constraints on theoretical models. These objects are a central part of this thesis and are described in further detail in the following Section.

1.3 Cataclysmic Variables

As briefly mentioned in the preceding Section, Cataclysmic Variables (CV) are close binaries whereby a WD (primary component) accretes matter via Roche-overflow of a low-mass MS companion (secondary component). When the WD magnetic field is weak (B$\lesssim$0.1 MG), the stream of material forms a ring around it, at a radius where angular momentum at the L1 Point is preserved. This is known as the circularisation radius. Viscous processes and conservation of angular momentum cause the ring to spread out until the inner edge reaches the WD. (Paczyński, 1971). The region where the gas stream impacts the outer rim of the fully-fledged disc is called the bright spot. It is worth noting that the disc not only transports matter inwards unto the white dwarf, but also angular momentum outwards (Hellier, 2001). Depending on the accretion rate (and orbital period), these systems get classified as either Dwarf novae or nova-likes.

On the other hand, strong magnetic fields ($B \gtrsim 10$ MG) completely inhibit the formation of the disc, and instead the inflowing material is channeled by the field.

These systems are known as Polars. Moderate fields ($0.1\,MG \lesssim B \lesssim 10\,MG$) are not sufficient to completely disrupt the formation of the disc, but they do truncate the inner regions, giving rise to the so-called intermediate Polars (Hellier, 2001; Warner, 2003).

Their relatively large numbers of several thousand confirmed objects (Pala et al., 2022; Inight et al., 2023) makes them optimal laboratories for binary evolution and accretion physics. In this Section I discuss how they are classified and the physical processes that drive their evolution. Given the nature of one of the objects of study of this thesis (V3101 Cyg, see Chapter 3), I will also delve into dwarf novae and in particular in the WZ Sagittae sub-class. However, for a detailed understanding of the phenomena occurring in CVs, the reader is referred to Warner (2003) and Hellier (2001).

1.3.1 A General Classification of Cataclysmic Variables

CVs are traditionally classified based on the behaviour of their lightcurves (Warner, 2003):

(1) Classical Novae: They have undergone only one observed novae eruption with a change of brightness of 6 to 19 magnitudes. Their eruptions are explained by thermonuclear runaways of the accreted material on the surface of the WD. The ejected layers create an expanding shell remaining for a long time (e.g. Rosenbush, 2020b; Chomiuk et al., 2021, see also Section 1.3.4).

(2) Recurrent Novae: these are classical novae that have been detected repeatedly in eruption (e.g. Rosenbush, 2020a).

(3) Dwarf Novae (DN): These systems show quasiperiodic outbursts of $2-5$ mag, and contrary to CN, they are caused by a thermal-viscous instability triggered in the accretion disc (e.g. Hameury, 2020, Section 1.3.2), which accelerates the mass transfer rate through the disc and onto the white dwarf, releasing considerable amounts of gravitational energy in the process. They have typical mass transfer values below $\sim 10^{-9}\,\mathrm{M_{\odot}\,yr^{-1}}$. Since the object of study of this project is a DN, it is worth listing the subtypes:

  - Z Cam: Their lightcurves show a succession of rapid outbursts with long standstills at a brightness below 0.7 of its maximum.
  - SU UMa: These systems show lightcurves with unusually long outbursts, called superoutbursts ($\sim$5 times the duration of ordinary outbursts and brighter by $\sim$0.7 magnitudes).

- U Gem: Their regular outbursts reveals them as DN, but they cannot be classified as Z Cam nor as SU Uma.

(4) Nova-like variables: the disc remains continuously in a hot, steady state (see Section 1.3.2) due to the persistently high mass transfer ($\dot{M} \gtrsim 10^{-9}\,\mathrm{M_\odot\,yr^{-1}}$, e.g. Patterson, 1984).

(5) Magnetic CVs: these are objects whose WD primary has a magnetic field that disrupts the accretion disk. Depending on the strength of the field they are subdivided in polars ($B \gtrsim 10\,\mathrm{MG}$) or intermediate polars ($0.1MG \gtrsim B \gtrsim 10\,\mathrm{MG}$).

Of particular relevance to this Thesis (Chapter 3), is the SU UMa sub-class of WZ Sge objects (see Kato, 2015, for a full review). They have short orbital periods, close to the period minimum cutoff in CVs ($\simeq$79 min, see Section 1.3.5); low mass ratios ($q \lesssim 0.1$); and a very low viscosity in the disc. Their lightcurves show superoutbursts that can reach up to $\sim$9 magnitudes and last weeks, with long intervals of quiescence in between, and sometimes showing multiple rebrightenings (e.g Amantayeva et al., 2021). The timescale of the long supercycle is believed to be rooted on a low mass-transfer rate and the low viscosity of the disc, that allow for more material to be accumulated before a thermal instability is triggered. I now turn my attention to the physical processes behind said instability.

1.3.2 Dwarf Novae and the Disc Instability Model

As mentioned before, the standard model of CVs (Warner & Nather, 1971; Smak, 1971), models the system as a secondary filling its Roche lobe and transfering matter to the primary through the L1 Lagrangian point. The material then orbits around the primary forming an accretion disc.

In dwarf novae, an increase in viscosity in the disc (Shakura & Sunyaev, 1973) is believed to trigger a thermal-viscous instability (Hameury et al., 1997, 2000; Hameury, 2020; Lasota, 2001) that causes inner annuli to slow down while outer annuli are sped up, thus transporting angular momentum outwards. Due to viscous processes, this mechanism also causes matter to flow inwards. In turn, this provokes an increase in the release of gravitational energy, dramatically raising the temperature of the disc.

However, if the mass transferred from the secondary is exceeded by the inward flow of material through the disc, the hot state is not sustained and the temperature drops back to its original quiescent state. This process is depicted by the surface density−temperature plot known as *the S-curve*. Its main features shown in Fig. 1.7 are described as follows (e.g. Hellier, 2001; Warner, 2003):

(1) $A \to B$: Point A represents a state of quiescence whereby the disc is stable. However, if the mass transfer exceeds the flow of matter in the low-viscosity disc, density to rise, from the outer disc, in an inward direction. This causes the system to move to point B, with a steady climb in temperature and viscosity, also triggering the ionisation of hydrogen.

(2) $B \to C$: The partial hydrogen ionisation causes the opacity to increase, which prevents energy to be radiated away, resulting in an abrupt increase in the temperature and further triggering ionisation. Once hydrogen is fully ionised a new equilibrium is reached at C. Note that the climb in temperature is practically vertical. This is cause the heating timescale is far shorter than the time it takes material to keep flowing, therefore surface density remains practically constant. At this point the hydrogen is fully ionised, and a new equilibrium of high state is reached, with high viscosity ensuing a high rate of inward flow. The release of gravitational energy results in an outburst of enhanced luminosity.

(3) $C \to D$: The high viscosity in point C allows for the inward flow of matter towards the WD to take place at an increased rate. However, the elevated accretion rate drains the excess material from the disc, as it exceeds the matter being transferred from the donor. The surface density in the disc and temperature decrease to point D, where partial recombination begins.

(4) $D \to A$: The decrease in temperature in point D allows for the hydrogen ions to partially recombine and viscosity to decreases. The temperature then drops abruptly to the quiescent state. Back in point A the ions completely recombine.

The above-described cycle results in a heating (or cooling) wave that starts at one annulus in the disc and pushes adjacent annuli over the instability threshold, triggering an outburst (or a drop to quiescence in the case of a cooling wave) (Mineshige & Osaki, 1985). An outside-inside outburst is triggered on the outer disc and propagates inward. This will generate a rapid rise in the lightcurve, since the material coming from outer annuli, where the surface density is higher, has a large effect on the inner annuli that have lower surface density. On the other hand, an inside-outside outburst occurs when the trigger is initiated in the inner disc and the heating wave expands outward. In this case the rise in the lightcurve will be slow (e.g. Hellier, 2001).

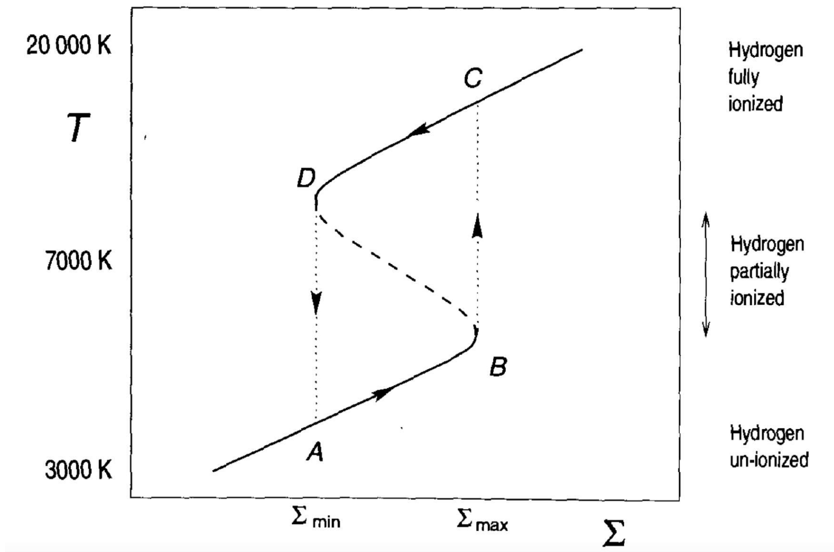

Figure 1.7: Surface density versus disc temperature depicting the cycle of a dwarf nova disc. Image taken from Hellier (2001).

The disc thermal instability model has become the standard prescription to explain the lightcurve behaviour of DN. And while the famous α-parametrisation of the disc viscosity (Shakura & Sunyaev, 1973) is successful in offering a general description of the disc behaviour, the origin of such viscosity is uncertain. Molecular viscosity has been discarded due to the relatively low density of the disc.

Magnetohydrodynamic turbulence has offered the most likely solution, since as it turns out, pure hydrodynamical simulations showed that eddies tend to be damped out in Keplerian discs. This led to the Hawley-Balbus magnetic instability prescription (Hawley & Balbus, 1998): Blobs of ionised (therefore magnetic) material positioned at different radii become connected by a magnetic field. But due to the differential rotation in the disc, the outermost blob rotates slower than the inner counterpart. And while the outer blob is sped up (gaining angular momentum), the inner one is slowed down (losing angular momentum). The magnetic field line becomes stretched, causing the field to grow, and creating magnetic turbulence that disrupts the orderly Keplerian flow. The Hawley-Balbus instability is especially strong during the disc high states due to the high ionisation of hydrogen. On the other hand during cold states, the neutral atoms do not couple with the magnetic field. This readily explains the viscosity difference between hot states in outburst and cold states of quiescence.

The thermal instability has gained widespread acceptance on its capacity to reproduce amplitude, duration, and recurrence time of dwarf novae lightcurves. However, certain systems require the inclusion of other mechanisms such as mass-transfer variations, disc irradiation, stream-disc overflow, or inner-disc truncation (e.g. Hameury & Lasota, 2021). However, these extra ingredients are not well-constrained, requiring further investigation to properly incorporate them to the models (Hameury, 2025).

1.3.3 Tidal Instability, Superhumps and Mass Ratio Determination

Photometry taken during superoutbursts of SU UMa-type CVs reveal a superposed low-amplitude modulation (Vogt et al., 1980; Kato et al., 2009; Tampo et al., 2020), called superhumps, that recur with a period slightly longer than the orbital cycle of the binary. The origin of superhumps has been modelled successfully (Whitehurst, 1988) by a tidal instability caused by the torque produced from the interaction of the disc with the secondary star. This tidal torque causes the disc to become elliptical and precess, causing the external orbits of the disc to intersect and dissipate additional energy (O'Donoghue, 1990).

The superhump periods in many SU UMa systems usually show the following stages (Kato et al., 2009): (A) early stage with a longer and stable superhump period; (B) middle stage with periods that show a positive period derivative; and (C) a final stage with a shorter, and stable period. Superhumps arising on the early stages of the superoutburst highly correlate with the orbital period, and have been modelled as a consequence of the 2:1 resonance[3] of the accretion disc and the secondary (Lin & Papaloizou, 1979). Other studies relate stage A superhumps as immature superhumps, that evolve to full growth at the 3:1 resonance during the beginning of stage B (Kato & Osaki, 2013). Late-phase superhumps show a shorter period than those of stage B and also likely occur at the 3:1 resonance radius (e.g. Whitehurst, 1988).

Modelling the thermal-tidal physics, the mass ratio (q) can be calculated from the superhump period ($P_{\rm sh}$) fractional excess: $\epsilon = P_{\rm sh}/P_{\rm orb} - 1$ (Hirose & Osaki, 1990; Kato & Osaki, 2013; McAllister et al., 2019). However, a difficulty in applying such method arises in the choice of the superhump stage, given that the superhump period changes throughout the superoutburst. Furthermore, pressure effects within the disk, which affect the apsidal precession rate, are often neglected (Kato & Osaki, 2013).

A few of the so-called $\epsilon - q$ relations have been put forth for different super-

[3]An $x : y$ resonance refers to that occurring at a radius in the disc where the material orbits x times for every y orbital cycles of the companion (e.g. Hellier, 2001).

hump stages. For example, the traditional method was calibrated for ϵ measured during stage B (Patterson et al., 2005):

$$\epsilon = 0.18q + 0.29q^2 \tag{1.15}$$

An updated prescription for stage B was proposed by McAllister et al. (2019), based on observational calibrations:

$$\mathrm{q}(\epsilon_\mathrm{B}) = (0.118 \pm 0.003) + (4.45 \pm 0.28) \times (\epsilon_\mathrm{B} - 0.025) \tag{1.16}$$

However, the unknown pressure effect is expected to be stronger in stage B, causing large uncertainties in Equation 1.15 (Kato & Osaki, 2013). Therefore a stage C relation can also be found in (McAllister et al., 2019):

$$\mathrm{q}(\epsilon_\mathrm{C}) = (0.135 \pm 0.004) + (5.0 \pm 0.7) \times (\epsilon_\mathrm{C} - 0.025) \tag{1.17}$$

Likewise Kato & Osaki (2013) also propose an independent calibration made with stage A superhump periods:

$$1 - \frac{P_\mathrm{orb}}{P_\mathrm{sh}} = \left(\frac{q}{2\sqrt{1+q}}\right)\left(\frac{1}{2}\sqrt{r}\, b^{(1)}_{3/2}(r)\right) \tag{1.18}$$

Where $\frac{1}{2}\sqrt{r}\, b^{(1)}_{3/2}(r)$ is the Laplace coefficient:

$$\frac{1}{2}\sqrt{r}\, b^{(j)}_{s/2}(r) = \frac{1}{2}\int_0^{2\pi} \frac{\cos(j\phi)\, d\phi}{(1 + r^2 - 2r\, cos\phi)^{s/2}} \tag{1.19}$$

And finally, the 3:1 resonance radius is given by:

$$r_{3:1} = 3^{-2/3}(1+q)^{-1/3} \tag{1.20}$$

In particular, using Equations 1.18 – 1.20 and measuring the stage A superhump period excess of the WZ Sge object V3101 Cyg (Tampo et al., 2020) estimated a mass ratio of $q = 0.0880(9)$. These authors argue that the stage A superhump period shows the most stability and therefore their choice of $\epsilon - q$ yields the most accurate mass ratio. However, as discussed in Chapter 3, using the different relations listed in this Section introduces a considerably larger systematic uncertainty ($q = 0.088 \pm 0.013$). This has particular relevance for the work of this thesis, since the mass ratio is used to reveal the substellar nature of the donor in V3101 Cyg, and its likely origin from the Brown Dwarf+White Dwarf (BD+WD) evolutionary channel (see also Section 1.3.5).

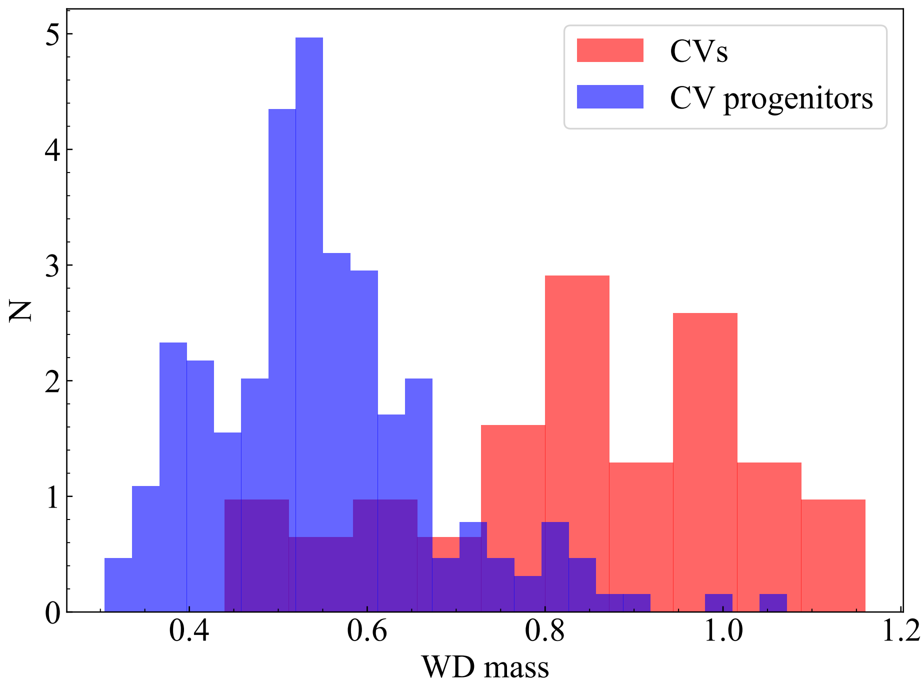

Figure 1.8: Mass distribution of cataclysmic variables (in red), peaking at $\simeq 0.83\,\mathrm{M}_{\odot}$, significantly higher than $\simeq 0.5\,\mathrm{M}_{\odot}$, the average mass of WDs in a combined sample of PCEBs and wide WD+MS binaries (blue), which are likely CV progenitors. The CV masses were obtained from Pala et al. (2022), and the progenitor masses from Rebassa-Mansergas et al. (2011).

Furthermore, given that the above-listed relations assume purely dynamical effects, thus neglecting pressure induced precessional braking, it is possible for the resulting superhump period excess to be underestimated. Therefore, alternative methods are recommended to impose stricter constraints on the mass ratio. The optimal approach, albeit expensive, is the direct measurement of the the mass of both components, or alternatively, their radial velocities. When possible, Doppler tomography can be used to map the emission of both the primary and an irradiated secondary to estimate the radial velocities of both components (e.g. Steeghs et al., 2001). Finally, in CVs with high binary inclination, eclipse modelling during quiescence can also be implemented to determine the mass ratio (e.g. Feline et al., 2004; Littlefair et al., 2006; Savoury et al., 2011).

1.3.4 Nova Outbursts and the Large Average-Mass Problem

One of the fundamental questions in CVs rises from their mass distribution (Livio & Soker, 1984). Specifically, the average WD mass in CVs ($\langle M_{\rm wd}\rangle \simeq 0.83\,{\rm M}_\odot$, Zorotovic et al., 2011; Pala et al., 2022) significantly exceeds that of single WDs ($\langle M_{\rm wd}\rangle \simeq 0.66\,{\rm M}_\odot$, McCleery et al., 2020; O'Brien et al., 2024)). More alarmingly, as shown in Figure 1.8, a large and homogeneous sample from the Sloan Digital Sky Survey (SDSS, York et al., 2000) of CV progenitors (PCEB and wide WD+MS binaries) shows a mass distribution that leans towards the low-mass end ($\lesssim$0.6M$_\odot$) of the isolated WD distribution (Rebassa-Mansergas et al., 2011). This discrepancy was initially dismissed as an observational bias, on the grounds that higher WD masses imply a larger accretion energy release; and that larger, and hence brighter, accretion discs should be harboured in the larger Roche lobes (Ritter & Burkert, 1986). However, an SDSS sample of CVs (Szkody et al., 2011) demonstrated the contrary: The detection of massive WDs is actually disfavoured, as expected from their lower luminosity owed to their smaller radii.

This turned the focus to the so-called classical nova outbursts: at the typical mass accretion rates ($10^{-10} - 10^{-8}\,{\rm M}_\odot\,{\rm yrs}^{-1}$) the transferred hydrogen-rich material does not burn stably in the surface, but it instead piles up (Wolf et al., 2013). When enough material is accreted onto the white dwarf surface ($\sim 10^{-4}\,M_\odot - 10^{-6}\,M_\odot$) the density and temperature increases at its base, triggering thermonuclear reactions at the bottom of the accumulated envelope layer. The thin outer envelope expands, engulfing the binary until it gets ejected (Hellier, 2001), analogous to the CEE (see Section 1.2.3).

Whether all the accreted mass becomes ejected from the WD after the nova eruption is not clear. This prompted the idea that the accreting WDs in CVs could grow in mass by retaining a considerable amount of the transferred material. This could be achieved if a thick helium shell accumulated from a long series of hydrogen flashes in the surface is ignited. After several nova cycles, the continual heating of the WD interior by helium flashes could lift the degeneracy in the outer layers. This would result in quasi-steady helium-burning instead of explosive reactions (e.g. Hillman et al., 2016). However, mass growth during nova cycles fails to reproduce the observed WD mass distribution and the period distribution of CVs (Wijnen et al., 2015).

Another proposed scenario is also related to nova eruptions, but instead of mass growth, it invokes mergers of the CV components when their primary is a low-mass WD. Recent novae models predict that systems hosting white dwarfs with low mass ($M_{\rm wd} \lesssim 0.6M_\odot$) require larger nova ignition masses (Shen & Quataert, 2022) and the velocities of the expanding envelope should be slower (Schreiber et al., 2016). The engulfed system then experiences a higher frictional loss of angular momentum (Schenker et al., 1998), which is drained from the orbital energy, destabilising the binary and ultimately leading to a merger (Metzger et al., 2021). This mass-dependent additional angular momentum prescription indeed agrees with the observational evidence showing a negative correlation between the mass transfer ratio and the white dwarf mass (Pala et al., 2022). However, it must be noted that various systems challenge this view by hosting WDs with masses far below $\simeq 0.6\,\mathrm{M_\odot}$(Pala et al., 2022): SDSS J100515.38+191107.9 ($M_{\mathrm{wd}} \simeq 0.44\,\mathrm{M_\odot}$); CU Vel ($M_{\mathrm{wd}} \simeq 0.47\,\mathrm{M_\odot}$); and particularly, V3101 Cyg ($M_{\mathrm{wd}} \simeq 0.47\,\mathrm{M_\odot}$), which is an object of study of this thesis (see Chapter 3). The WD mass measurements for all of these three systems are reliable, given that they were obtained from *HST* ultraviolet observations combined with Gaia DR3 parallaxes (Pala et al., 2022, see also Chapter 3). Furthermore, none of the systems are eclipsing, so their UV spectrum is not expected to be affected by the so-called *iron-curtain* (Horne et al., 1994), which is a layer of absorbing material from the disc, usually detectable as a forest of Fe II absorptions in the UV and blue regions of the spectrum, that can affect the spectroscopic estimations of the WD-parameters (e.g. GY Cnc, Gänsicke et al., 2000; McAllister et al., 2019; Littlefair et al., 2024; Godon & Sion, 2022).

1.3.5 Evolution of Cataclysmic Variables

As discussed in Section 1.2.2, sustained and stable mass transfer is only possible through a continual decrease of the donor's Roche Radius. Equation 1.10 shows that this strictly requires continuous AML. Furthermore, Equation 1.8 shows that $\dot{J} \lesssim 0$ causes a reduction in the orbital separation, and thus the orbital period. It then becomes evident that AML is the main driver of CV evolution. The main mechanisms of AML invoked CVs are Gravitational Radiation (GR) and Magnetic Braking (MB).

GR is a general relativistic effect consisting on creating ripples of spacetime warps caused by the orbital movement. It can be approximated with Einstein's quadrupole formula (Paczyński, 1967):

$$\dot{J}_{\mathrm{GR}} = \frac{-32}{5}\frac{G^{7/2}}{c^5}\frac{M_1^2 M_2^2 M^{1/2}}{a^{7/2}} \tag{1.21}$$

Where c is the speed of light and G the gravitational constant. On the other hand MB is caused by a stellar wind emanating from the secondary that interacts with its magnetic field. The ionised particles corotate with the magnetic field at the Alfvén

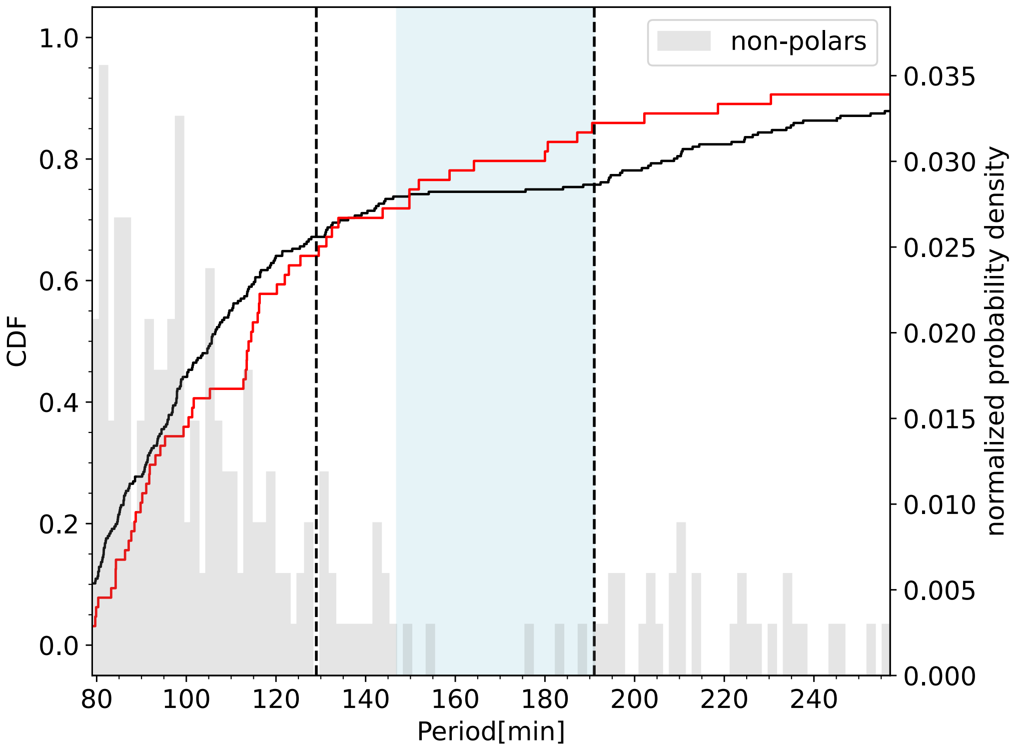

Figure 1.9: Histogram of the period distribution of non-polar Cataclysmic Variables, showing a dearth of systems within the period gap region (shaded in light blue). Comparing the cumulative distribution function of polars (red) and non-polars (black) further highlights the lack of non-polars in the period gap region. Image obtained from Schreiber et al. (2024)

radius. They are accelerated and eventually ejected from the system, carrying away substantial angular momentum. The star responds by slowing down its rotation. And since tidal forces tend to synchronise the orbits of the components in close binary systems, the braking stellar rotation ultimately causes the orbit to shrink as a response to the AML. The prescription by Rappaport et al. (1983) is widely used to model MB, given its versatility to modify shape and strength of the magnetic field through the γ parameter:

$$\dot{J}_{\rm MB} = -3.8 \times 10^{-30} \left(\frac{M}{\rm g}\right) \left(\frac{R_\odot}{\rm cm}\right)^4 \left(\frac{\Omega}{\rm s^{-1}}\right)^3 \left(\frac{R}{R_\odot}\right)^{\gamma_{\rm MB}} \tag{1.22}$$

Where k_2 is the radius of gyration of the region where the magnetic wind is coupled to the star. However, despite its advantages, matching well with observations of accreting objects, it struggles to reproduce mass transfer rates, and thus evolutionary time-scales of certain compact binaries, such as CVs (e.g. Belloni et al., 2020; Pala et al., 2022).

Now, as implied in Section 1.2.2 (see Equations 1.8 and 1.10), the rate of AML is closely related to the secular mass-accretion rate. And since mass accretion causes compressional heating, the WD components have a higher temperature than their isolated analogues (see Section 1.1.2). Indeed, a correlation between the WD effective temperature and the long-term average of the accretion is known (Townsley & Bildsten, 2002, 2003; Townsley & Gänsicke, 2009). Therefore the WD temperature can be used as a proxy in the evolutionary characterisation of CVs. However, since the accretion disc and the MS donor dominate the emission in optical wavelengths, a clean determination of the WD temperature becomes only possible in the Ultraviolet (UV) range (Gänsicke et al., 2006a).

Nevertheless, as made obvious in Eq. 1.8, the most direct indicator of evolution through AML is the orbital period of the system. In other words, determining the evolutionary stage of CVs dependent on AML, becomes a problem of measuring their orbital period. The period distribution of CVs (see Fig. 1.9) then offers invaluable clues to their evolution. I now focus on the two canonic features of this distribution which have been used to impose constraints on the AML prescription: the Period Gap at $\simeq 2 - 3$ hrs; and the Period minimum at $\simeq 76$ min.

Period Gap

The period distribution of CVs exhibits a dearth of detections in the $\simeq 2 - 3$ hrs range (e.g. Schreiber et al., 2024, see also Fig. 1.9). This is attributed to a disruption of the MB (Rappaport et al., 1983). The standard AML recipe predicts that above the gap ($P_{\rm orb} \gtrsim 3$ hrs), whereby the donor has a radiative core, MB is orders of magnitude stronger than GR, thus dominating the evolution (Knigge, 2006; Knigge et al., 2011). The high accretion rates in this regime drive the donor out of thermal equilibrium, causing it to bloat slightly and maintain contact with its Roche lobe. After sufficient mass-loss (at $P_{orb} \simeq 3$ hrs), however, the donor becomes fully convective. This abruptly decreases MB, allowing the donor to recover thermal equilibrium and detach from its Roche Lobe; effectively ceasing mass transfer (Hellier, 2001; Warner, 2003). This explains the lack of CV detections in the distribution, in what is known as the period gap. Eventually AML via GR (and perhaps residual MB) decreases sufficiently the size of the Roche lobe to restart mass transfer below the gap ($P_{orb} \lesssim 2$ hrs).

In accordance to the standard prescription, the mass-transfer timescales are of comparable magnitude both above and below the period gap ($\tau_{\dot{M}_2} \simeq 4 \times 10^8$ yrs) (Knigge et al., 2011). And yet, the existence of the gap has not been immune to debate. In particular, conclusions drawn from recent volume-limited samples contravene each other regarding the statistical significance of its existence: while the gap is clearly present in Pala et al. (2020), this sample is liable to low-number statistics; on the other hand, a larger homogeneous sample from SDSS (Inight et al., 2023) does not show clear evidence for the presence of the gap. Magnetism offers a possible solution to the apparent contradiction: upon dividing the SDSS I-IV sample based on their magnetic classification (Section 1.2.4), Schreiber et al. (2024) were able to show a statistically significant period gap for the non-polar population (see also Fig. 1.9). This is further proof that the existence of the gap is indeed related to MB.

Period Minimum

Another marked feature of the period distribution is the sharp cut-off at $\simeq 77$ min. To explain existence of the period minimum it is necessary to investigate the response of main sequence stars to mass-loss. The so-called mass-radius index (ξ) relates these two parameters as: $M \propto R^{\xi}$. A logarithmic differentiation of this relation then yields an expression for the mass loss and the rate of change of the secondary's radius:

$$\frac{\dot{R}_2}{R_2} = \xi \frac{\dot{M}_2}{M_2} \tag{1.23}$$

The value of ξ, and therefore the behaviour of Eq. 1.23, depends on the characteristic timescales involved in perturbing ($\tau_{\dot{M}}$) and restoring (τ_{KH}) thermal equilibrium. As discussed in Section 1.2.2, if the mass-loss timescale exceeds the thermal timescale ($\tau_{\dot{M}_2} >> \tau_{\mathrm{KH}}$) thermal equilibrium is maintained by the donor, in which case the mass-radius index has a value of ~ 0.8 (characteristic of a low-mass MS stars). On the contrary, when $\tau_{\mathrm{KH}} >> \tau_{\dot{M}_2}$, the mass-loss is fast and adiabatic, and the donor is unable to restore thermal equilibrium. The response to adiabatic mass-loss of low-mass stars with a significant convective envelope is to expand (Knigge et al., 2011). In this regime the ξ index has a value of $\sim$1/3 (Rappaport et al., 1982).

Now, as explained in detail by (Knigge et al., 2011), combining Eq. 1.9 and Kepler's third law yields the period density relationship:

$$\langle p \rangle = \frac{3M_2}{4\pi R_2^3} \tag{1.24}$$

Applying logarithmic differentiation to Eq. 1.24 and using the mass-radius relationship in Eq 1.23, yields an equation that models the evolution of the orbital period:

$$\frac{\dot{P}_{\rm orb}}{P_{\rm orb}} = \left(\frac{3\xi - 1}{2}\right) \frac{\dot{M}_2}{M_2} \quad (1.25)$$

Equation 1.25 predicts a minimum ($\dot{P}_{\rm orb}$=0) occurs at the adiabatic expansion regime when $\xi = 1/3$, with the companion bloated and far out of thermal equilibrium. After this point the period derivative switches sign, thus the orbit stops shrinking and instead increases. As such, systems that pass this bounce-back threshold are called *period bouncers*. As expressed above, any donor with mass-loss timescale radically exceeding the thermal timescale could become a period bouncer. In practice, however, the period minimum marks the threshold where the donor reaches the hydrogen burning limit[4] and becomes substellar (Knigge, 2006).

Given the long evolutionary timescales of the stellar to sub-stellar transition, synthetic models predict an accumulation of systems at $\simeq 65 - 70$ min (Kolb & Baraffe, 1999). This is in considerable disagreement ($\sim$ 10%) with the observed cut-off at $\simeq 76 - 79$ min (Ritter & Kolb, 1998, 2003; Gänsicke et al., 2009), therefore posing serious challenges to the standard AML recipe. A semi-empirical donor sequence, constructed on observational and theoretical constraints (Knigge, 2006), signals the requirement of an additional source of AML, in order to shift the cut-off towards higher periods. Nonetheless, the physical process driving the additional braking remains unclear.

Despite the peak of faint CVs found at $\sim$ 79 min (Gänsicke et al., 2009) only a handful of period bouncers have been confirmed (e.g. Patterson, 2011). These systems are intrinsically difficult to detect in quiescence, since the accretion-heated WD outshines the donor in all optical bands and emits at comparable brightness in the infrared (Knigge, 2006). Furthermore, their accretion rates are low, an by consequence so are their X-ray luminosities, accretion disc sizes and outburst recurrence. Nevertheless, a volume-limited sample with up to $\sim$ 70% completeness (Pala et al., 2020), updated with an eROSITA catalogue, reveals a relatively small fraction of $\sim$ 25% of period bouncers (Rodriguez et al., 2025). Even accounting for the expected undetected systems, this low percentage is at odds with the theory, which predicts up to $\sim$70% of CVs should have already evolved past the bounce-back regime (Kolb, 1993; Goliasch & Nelson, 2015; Belloni et al., 2018).

It has been proposed that the WD component can develop a strong magnetic field, that then connects with the field lines of the donor. This causes the WD to spin down and transfer angular momentum to the orbit, effectively detaching the donor from its Roche lobe and ceasing the accretion process, thus no longer appearing as

[4]When the secondary runs out of hydrogen in the core and nuclear fusion progressively decreases.

a CV (Schreiber et al., 2023). Such a strong magnetic field could develop within a few Gyr as a product of crystallisation powered dynamo (Isern et al., 2017, see also Section 1.1.2); or from the emergence of fossil fields buried in the stellar interior during the progenitor's giant phases (Camisassa et al., 2024). These systems would remain virtually undetectable and would imply a large number of magnetic WDs with detached brown dwarf companions. A strong candidate to observationally prove this scenario is ZTF J021804.16+071152.93, a detached magnetic WD (19 MG) plus a BD binary with an orbital period of 1.7 hrs. Its white dwarf parameters and membership of the galactic thick disk implies that the system previously went through a stable accretion phase (Parsons et al., 2026), discarding a pre-CV nature. Furthermore, the X-ray detection of two long-period ($P_{\rm orb} \simeq 100$ min) magnetic CVs with substellar companions (Cunningham et al., 2025) offer possible additional observational support to this hypothesis. These systems, identified in the *XMM-Newton* catalogue (Webb et al., 2020), at the very least, help reconcile the expected space density of period bouncers for the case of magnetic CVs. But whether the remaining period bouncers are truly out there, or if CV evolution requires a shift in paradigm, is still a matter of current investigation.

Below the Minimum: The search for Brown Dwarf+White Dwarf pair progenitors

WDs with low-mass MS companions dominate the PCEB population. If following CEE, the binary separation is of the order of a few solar radii, orbital decay will likely transform the system into a CV within a Hubble time. As detailed in the previous Sections, AML causes the system to evolve to shorter periods, until a minimum at $\simeq 80$ min is reached, at which point the donor becomes substellar and the CV evolves back toward longer periods.

However, comprehensive population synthesis analyses, predict an alternative formation channel for CVs harbouring substellar donors: Up to $\sim 18\%$ of the zero age CVs are expected to have emerged from the CEE as detached BD+WD pairs (Politano, 2004; Politano & Weiler, 2007). The overwhelming majority ($\sim 80\%$) are expected to eject the common envelope at orbital periods $\lesssim 78$ min (Politano, 2004). GR causes the brown dwarf to become in contact with its Roche lobe, and the onset of mass transfer causes it to expand. The binary responds by expanding, and eventually, at periods of ~ 70 min, this evolutionary track is predicted to merge with the period bouncer channel, regardless of the initial substellar nature of the donor (Kolb & Baraffe, 1999).

BD+WD pairs, like their progenitors, are inherently scarce, as attested by the low numbers ($\sim 0.8\%$) of brown dwarfs orbiting solar-type stars within ~ 10 au, compared to planetary or stellar companions (e.g Grether & Lineweaver, 2006; Unger et al., 2023). However, as discussed in Section 1.2.3, CEE does not thwart the survival of substellar donors with masses over $\sim 10\,\mathrm{M_J}$ (Yarza et al., 2022). Indeed, despite their rarity (Farihi et al., 2005), white dwarfs hosting a brown dwarf companion in short orbital periods (∼hrs) have been identified (e.g. Farihi & Christopher, 2004; Burleigh et al., 2006; Maxted et al., 2006; Littlefair et al., 2014; Longstaff et al., 2019; Casewell et al., 2020; de Wit et al., 2025), with a few even having orbital periods below the period minimum: e.g. SDSS J1205-0242 ($P_{\rm orb} \simeq 71.2$ min, Parsons et al., 2017; Rappaport et al., 2017), SDSS J1231+0041 ($P_{\rm orb} \simeq 72.5$ min, Parsons et al., 2017) and EPIC 21223532 ($P_{\rm orb} \simeq 68.2$ min, Casewell et al., 2018).

Yet, no unambiguous observational confirmation of a CV following this alternative channel has been reported. CVs with periods below the minimum are natural candidates to consider. The CV-related objects AM CVn stars fullfill this condition, but this is due to the degenerate donor (e.g. Green et al., 2020). V485 Cen ($P_{\rm orb} \simeq$59 min, Augusteijn et al., 1996); EI Psc ($P_{\rm orb} \simeq$64 min, Thorstensen et al., 2002); and GALEX J194419.33+491257.0 ($P_{\rm orb} \simeq$76 min, Kato & Osaki, 2014) all are CVs with periods below the observed cutoff, but were dismissed as BD+WD descendants since their hot donors are likely nuclearly evolved (Augusteijn et al., 1996; Thorstensen et al., 2002; Gänsicke et al., 2003). This occurs when mass transfer begins after the companion has already burnt most of its hydrogen into helium in its core. These donors are therefore more compact, forcing them into shorter orbital periods in order for RLOF to take place (Belloni & Schreiber, 2023a). As a matter of fact, these CVs with nuclearly evolved donors are a possible evolutionary mid-stage between super-soft X-ray sources and AM CVn stars (e.g. Schenker et al., 2002).

SDSS J150722.30+523039.8 ($P_{\rm orb} \simeq 66.6$ min) was identified as a promising prospective product of the BD+WD channel (Szkody, 1985; Littlefair et al., 2007). However, its high space velocity (Patterson et al., 2008) and subsolar metallicity (Uthas et al., 2011) revealed this object as a member of the Galactic Halo and therefore a Population II metal-poor system (Uthas et al., 2011). These systems have a lower atmospheric opacity, which would account for a smaller radius than a Population I donor, and thus explain the short period. I argue in Chapter 3, that to the best of my knowledge, V3101 Cyg is the best candidate to fill this gap in the literature.

So far, I have only discussed WD accretion from either stellar or brown dwarf donors. However, although likely different in origin, WDs have also been found to accrete material from the disrupted bodies of far smaller substellar objects: planets and planetesimals. It is now time I turn my attention to these objects with extreme mass ratios.

1.4 Planetary White Dwarf Systems

The Planets of our solar system, the wanderers of the sky, have evoked awe to the peoples of Earth since the origins of civilisation. Their movements, not in concert with the east-to-west march of the stars, quickly betrayed a different nature. And while exponential progress has been made since, there are still a plethora of questions awaiting investigation from a curious beholder. The diversity of planets (Berger et al., 2026) and correlations with their host stars (Ghezzi et al., 2026); the constraints for their formation (Ochem & Marrocchi, 2026), orbital migration (Jinno et al., 2026), and conditions for post-MS survival (Malamud, 2026); their atmospheric conditions (Clavier et al., 2026), elemental abundances (Sun, 2026; Bonsor, 2026), magnetic interactions (Pineda et al., 2026) and orbital architectures (He & Ford, 2026), are all issues that will occupy researchers for the foreseeable future. Not only for their inherent scientific value, but also because they are necessary steps in a pathway to answering a far more fundamental question (Alexandrov et al., 2026; Fetherolf et al., 2026; Arney et al., 2026): Is there life out there?

This is no longer just a purely theoretical question, as evidenced by the scientific effort to put in orbit the Habitable Worlds Observatory (HWO, Peacock et al., 2025; Arney et al., 2026), a NASA flagship project meant te be launched in $\sim$2040. These habitable planets, however, will not necessarily be hosted by a MS star. Indeed, planetary systems are known to survive the evolution of their parent stars into WDs (Veras, 2021). These systems uncover insights that are largely inaccessible in the analysis of their MS progenitors, especially in terms of their internal structure and composition (e.g. Zuckerman et al., 2007). It is in this spirit, that I now embark on describing the general framework of their formation as well as the main clues these systems have to offer to the bigger questions.

1.4.1 Formation of WD planetary Systems

Whether planets exist outside of our solar system is a question that has been long resolved. When considering all current detection methods, the frequency of planets in our Milky way is estimated to be of the order of 1.6 per star (Cassan et al., 2012), with about double the occurrence rate around single stars than binary star systems (Sullivan et al., 2026). The current count stands at over $\sim$ 6000 detected exoplanets,

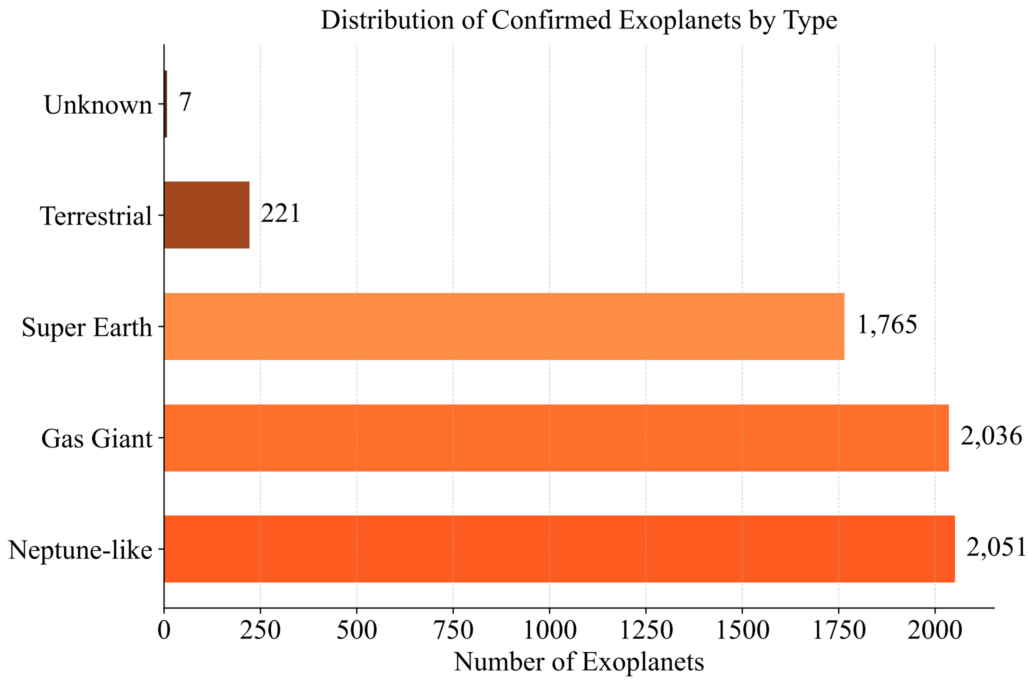

Figure 1.10: Distribution of observed exoplanets by type. The total amount of detected exoplanets was of 6080 at the time the data was retrieved (in 2026-01-27 from the NASA exoplanet archive). It must be noted that the number of exoplanets is expected to change by the time the reader has access to this thesis, but the chart is meant to illustrate the already considerable quantity of detections.

with the bulk having been detected via transits (∼74%), radial velocity (∼ 19%), microlensing (∼ 4%) and imaging methods (∼ 2%).

As shown in Figure 1.10, the exoplanets are generally classified in four types: (1) Terrestrial: like the inner planets of our solar system, they are mostly made of rock and metals; (2) Super Earths: they have a range of $\simeq 2 - 10$ times the size of Earth with comparable composition; (3) Neptune-like: composed mostly of frozen water, ammonia and methane, analogous to Neptune and Uranus; and (4) Gas Giants: mostly composed of hydrogen and helium resembling Jupiter and Saturn. This classification is achieved by deriving an average density based on mass and radius measurements, combined with an expected composition derived from atmospheric parameters of the parent star and planetary structure models (e.g. Valencia et al., 2007; Rogers & Seager, 2010; Baumeister et al., 2025).

The detected exoplanets, along with our own Solar system architecture have helped cement the foundation of planetary formation theory, which is closely linked to the origin of their parent stars in stellar nebulae (e.g. Carroll & Ostlie, 1996;

Tobin et al., 2022). Kelvin-Helmholtz contraction causes a nebula to collapse under its own weight resulting in the formation of a protostar and a circumstellar disc. After major dissipation of the envelope dust, the star accretes matter from the disc, further contracting until hydrogen burning is ignited (Hayashi, 1966; Shu et al., 1987; Palla & Stahler, 1999; Larson, 2003). It is within the circumstellar disc that the planets are destined to form (Armitage, 2010). As the disc cools down, gas particles condense into microscopic solid grains. Chemical bonds and gravitational forces result in coagulation and instabilities that form accumulations of dust and pebbles, which progressively coalesce to form planetesimals with km-sized diameters (Comins & Kaufmann, 1999). The planetesimals collide and merge, eventually forming full-fledged planets, whereby the collision melt the rocky material, causing the denser minerals to sink, in a process known as chemical differentiation (Toulhoat & Zgonnik, 2022). This is the accepted formation channel of the inner terrestrial rocky planets in our solar system: Mercury, Venus, Earth and Mars (Baumeister et al., 2025).

However, in the outer and colder regions of the disc, beyond the so-called ice-line, volatile compounds such as water, methane (CH_4), and ammonia (NH_3) can survive as ices. These ice-forming elements are more abundant than rocky grains (composed of silicon, magnesium and iron). Therefore, planets on the outer regions, made-up of a mixture of ices and rock, are several times larger than the inner terrestrial planets (e.g. Carroll & Ostlie, 1996). Furthermore, due to the relatively slow velocities of gases in the outer regions, the larger rocky and icy cores accrete hydrogen and helium, developing a thick envelope analogous to those in Saturn, Jupiter, Uranus and Neptune (e.g. Bodenheimer & Pollack, 1986).

The above-mentioned scenario illustrates the origin of planetary systems, but then, what happens when the MS parent star experiences the metamorphosis into a WD described in Section 1.1.1? It is a well established fact that stars harbour planetary systems both before (Mayor & Queloz, 1995) and after (van Maanen, 1917; Wolszczan & Frail, 1992) the giant phases. But the circumstances that ensure survival are not completely clear. In general, guarantee of safe passage depends primarily on orbital separation, initial masses of the star and planets, and mass-loss during and after the AGB stage. Piecing together how these conditions constrain evolution is paramount to understanding whether if our own planet Earth will survive the Sun's giant phases. This remains subject of active investigation, but due to tidal interactions and drag experienced in the chromosphere of the giant Sun, Earth is not expected to avoid engulfment (Schröder & Connon Smith, 2008). Mars, however, and the planetary bodies beyond, will very likely survive the post-MS transition (Rybicki & Denis, 2001).

The surviving planets interact gravitationally, scattering asteroids, moons and even the innermost planets into the potential well of the WD. Inside the so-called tidal radius, the object's self gravity is exceeded by the tidal-gravitational forces of the WD. This causes the orbiting body to become shredded into dust and gas, eventually getting accreted by the compact object (Debes & Sigurdsson, 2002; Jura, 2003; Veras & Gänsicke, 2015). In the following Sections, I will briefly discuss the observational evidence sustaining WD planetary science, such as photospheric enrichment (pollution) of the WD (Zuckerman et al., 2003; Koester et al., 2014), dusty (Zuckerman & Becklin, 1987; Kilic et al., 2005) and gaseous debris discs (Gänsicke et al., 2006b; Melis et al., 2012; Manser et al., 2016b; Manser, 2018), solid planetesimals (Vanderburg et al., 2015; Manser et al., 2019; Vanderbosch et al., 2020) and even giant planets (Gänsicke et al., 2019).

1.4.2 Photospheric Enrichment

Despite the predominance of radial velocity analyses and transits for exoplanet detection in general (Zhu & Dong, 2021, see also Section 1.4.1), these techniques are not as successful in finding WD planetary systems. The WD small radius ($\sim 1.4\,R_{\oplus}$) and low luminosity make finding transits difficult (but not impossible, e.g. Vanderburg et al., 2020); and the need for high-resolution spectroscopy makes radial velocities expensive (e.g. Rogers et al., 2024a; Ramírez et al., 2025, see also Chapter 4).

However, the WD high density ($10^6\,\mathrm{g\,cm^{-3}}$, Saumon et al., 2022), and hence strong surface gravity (g$\sim 10^8\mathrm{cm\,s^{-2}}$) , provides a solution. At temperatures with limited radiative forces ($T_{\rm eff} \lesssim 25\,000\,\mathrm{K}$) it would be expected that the WD spectra display pristine atmospheres with only hydrogen or helium absorptions (or a combination of both). This is due to the fact that elements heavier than helium sink within the atmospheres in timescales far shorter than the cooling sequence (Schatzman, 1948, see also Section 1.1.2). However, atmospheres enriched with traces of metals, are detected in up to $\simeq 25-50\%$ of white dwarfs (Zuckerman et al., 2003; Koester et al., 2014). Indeed, a recently compiled database recorded, at the time of publication, up to 1739 metal-enriched WDs and a total of 24 different photospheric metals detected (Planetary Enriched White Dwarf Database, Williams et al., 2024).

Measuring the metal abundances of photospheric enrichment allows a unique opportunity to directly probe the mass fraction of each element in the parent body (e.g. Rogers et al., 2024b). Deriving the parent bulk-composition from the photospheric abundances requires an accurate calculation of the velocity with which metals gravitationally sink out of the atmosphere. However, since different metals sink out at different rates, the material measured directly from the WD photosphere will not be equal to that of the accreted parent body (Paquette et al., 1986a,b; Dupuis et al., 1993). In other words, elements with shorter timescales would appear as relatively depleted in the WD atmosphere due to this differential sinking.

The calculation of these timescales requires a modelling of the WD atmosphere accounting for the following element transport mechanisms (see Bédard, 2024, for a comprehesive review.):

(a) Diffusion: It refers to the net movement of a chemical component in the presence of a spatial gradient of a physical quantity. The main gradients taking place in WDs are of composition, pressure and temperature. These lead to the main three types of diffusive transport: chemical diffusion, gravitational settling, and thermal diffusion, respectively. These microscopic mechanisms are a function of atomic mass and charge, and are therefore different for each element.

(b) Radiative levitation: The photons propagating throughout the envelope of the star transfer outward momentum to highly absorbing atoms, counteracting gravitational settling (e.g. Chayer & Dupuis, 2010). The efficiency of the radiative force depends on the opacity of each element; therefore, in WDs, elements with higher opacities in the UV are the most affected by this matter-radiation interaction.

(c) Convection: It consists of a macroscopic cyclic flow of matter, causing hot fluid to rise and cooler fluid to descend. This type of heat transport occurs in high-opacity regions whereby radiation becomes ineffective. As the white dwarf cools down, a convective region develops in the outer envelope due to recombination of the atmosphere constituents (Saumon et al., 2022). The fluid motions effectively mix the present chemical species within the convective region, wiping out the sedimentative effects of diffusion (Bédard, 2024). Therefore, differential sinking in WDs can only occur below the convective envelope, where its effects are slower than at the surface. In this context, if convective cells enter underlying stable layers — in a process known as convective overshoot — the uniformly mixed region extends further, forcing differential sinking to occur at even deeper layers (e.g. Cunningham et al., 2019).

(d) Thermohaline mixing: A hypothesised instability expected to be triggered by the inverted composition gradient of a heavier material (accreted metals) onto a lighter fluid (H/He atmosphere). If active, this instability is expected to render differential sinking inactive, causing all metals to sink at similar timescales (e.g. Buchan et al., 2025), therefore, dramatically affecting the interpretation of the measured photospheric abundances (Bauer & Bildsten, 2018).

As described above, diffusion constantly competes with upward forces such as radiative levitation and convection, resulting in different sinking timescales that must be accounted for to determine the composition of the accreted material. Different treatments of these processes can have considerable effects on the interpretation of the abundances. Furthermore, additionally to the intrinsic stellar properties, the calculated parent-body composition will also be altered by the accretion phase in which the abundances are measured (Koester, 2009). The standard picture, albeit simplistic, assumes an accretion event having an instantaneous start, followed by a constant accretion rate, which eventually also shuts off instantaneously; thus dividing the process in three distinct phases (Koester, 2009; Buchan et al., 2025):

(a) Build-up phase: the abundances increase linearly with time, and the relative abundances resemble the parent composition.

(b) Steady state: The abundances reach a plateau due to a diffusion-accretion equilibrium, i.e., the metals diffuse out of the convection zone at the same rate at which they are accreted on to the atmosphere. To obtain the parent composition, the relative abundances must be weighed by their respective sinking timescales. The parent-body number abundance N is calculated via[5] (Williams et al., 2024; Gänsicke et al., 2012; Koester et al., 2014):

$$\frac{N(Z)}{N(\mathrm{Si})} = \frac{\dot{M}(Z)}{\dot{M}(\mathrm{Si})} \frac{A(\mathrm{Si})}{A(Z)} \tag{1.26}$$

Where A is the atomic mass; the accretion-mass ratio ($\dot{M}$) is obtained (in units of $\mathrm{g\,cm^{-2}\,s^{-1}}$) from the measured WD photospheric abundance X_{acc} at the Rosseland mean opacity ($\tau_{\mathrm{Ross}} = 2/3$), assuming a constant diffusion flow of each element (Koester et al., 2014):

$$X\,\rho\,v_{\mathrm{diff}} = \mathrm{const} = X_{\mathrm{acc}}\dot{M}_{\mathrm{acc}} \tag{1.27}$$

Where the mass density in the atmosphere (ρ) and the diffusion velocity (v_{diff}) are depth-dependent, leading to a stratified structure from which the mass fraction of the respective element (X) can be calculated from atmospheric models (Koester, 2010; Koester et al., 2014)

(c) Declining phase: Accretion at this point has stopped and the parent abundance depends on the diffusion timescales of each metal (τ_Z). The abundance ratio

[5] Si is commonly used for abundance ratio calculations, however, other common references metals include Mg and Fe

measured at a time t is calculated with respect to the instant t_0 of the accretion shut-down (e.g. Williams et al., 2024):

$$\frac{N(Z,t)}{N(Si,t)} = \frac{N(Z,t_0)\, e^{t/\tau_Z}}{N(Si,t_0)\, e^{t/\tau_{Si}}} \tag{1.28}$$

Therefore, to accurately estimate the chemical composition of the parent body, an assumption on the accretion state at the time of the observations needs to be made. In the case of warm hydrogen-dominated DAs ($T \gtrsim 11\,000$ K), the metal-diffusion timescales range from days to a few years, so metal detection can be safely assumed to occur during the steady state. However, this assumption is not valid for cooler DAs ($T \lesssim 11\,000$ K) and helium-rich DBs ($T_{\rm eff} \lesssim 20\,000$ K) (Koester, 2009), which have extended convection zones and whose long diffusion timescales ($\sim 10^6$, e.g. Izquierdo et al., 2021) are comparable to the lifetimes of circumstellar debris discs around WDs ($10^4 - 10^6$ Girven et al., 2012, see also Section 1.4.3). Thus, in the latter systems, all the accretion states have to be explored to derive the parent-body composition (e.g. Izquierdo et al., 2021); unless a circumstellar disc is detected, which would imply a system in the steady state.

A variety of chemical compositions have been unraveled from photospheric metal-enrichment (Williams et al., 2024), with the majority of objects displaying either a chondritic (Doyle et al., 2023) or bulk Earth nature (e.g. GD 424, Izquierdo et al., 2021). Such findings hint at a resemblance between these exoplanet systems and our own solar system, although unusual compositions have indeed been found. For example, the iron-rich (or icy) Mercury (or Kuiper-belt) analog (Johnson et al., 2022). Evidence of core-mantle differentiation has also been observed as an enrichment of siderophilic[6] (PG 0843+516, Gänsicke et al., 2012) or litophilic[7] (Melis & Dufour, 2017) elements. Studying the oxygen budget with respect to rock-forming elements, WDs hosting water-planet candidates have already been identified (Farihi et al., 2011, 2013; Raddi et al., 2015; Xu et al., 2016; Hoskin et al., 2020; Klein et al., 2021), showcasing the immense potential of WDs to search for habitable worlds.

Theoretical simulations indeed demonstrate the relation between the photospheric enrichment and planet accretion, and also explain how planetesimals in stable orbits can migrate inwards within the WD tidal disruption radius; where the planetesimal's self-gravity and cohesion yield to the gravity of the WD. Gravitational interactions with exterior sub-Jovian planets (Frewen & Hansen, 2014), liberated ex-

[6] iron rich material that tends to sink to the core

[7] Rock forming elements with strong affinity to combine with oxygen, usually found in the mantle or crust.

omoons (Payne et al., 2016, 2017) or even wide binary stellar companions (Bonsor & Veras, 2015), perturb and scatter inner-orbit planetesimals onto highly eccentric orbits ($e \gtrsim 0.98$) within the WDs Roche Radius. The debris then forms a highly eccentric (likely colisionless) ring that orbits the WD. If perturbative forces (besides gravity) are factored in, such as radiation-induced Poynting-Robertson drag (Guess, 1962) or sublimation, the eccentric ring shrinks down to a circular disc within the tidal disruption radius (Veras et al., 2015). Such a disc then acts as a material reservoir for WD accretion (Veras et al., 2014). Observational evidence for disrupted debris orbiting WDs has been found as infrared excess (although not as widespread as enrichment), which I briefly discuss in the following Section.

1.4.3 Debris Discs

Dusty debris disc

Dusty debris discs around WDs are detected as infrared excess above the white dwarf continuum (Zuckerman & Becklin, 1987; Graham et al., 1990). Circumstellar dust reprocesses the stellar light and emits at longer infrared wavelengths with typical temperatures of $\simeq 1000\,\mathrm{K}$ (Farihi, 2016). The detection of metal enrichment in the first white dwarf hosting a disc (G29-38), cemented the idea of circumstellar disc accretion (Koester et al., 1997). Furthermore, a correlation has been recently found between the dust mineralogy and the metal abundances in the WD photosphere (Rogers et al., 2025), suggesting accretion occurs over short timescales in homogeneous-composition conditions.

However, despite the high percentage of metal-enriched WDs ($25-50\%$), population studies reveal a mere $1-3\%$ of WDs harbouring detectable dusty discs. (Farihi et al., 2009; Steele et al., 2011; Rocchetto et al., 2015). This implies that up to ∼90 percent of disc go undetected. Instrumental sensitivity can be discarded as the main issue, since a dusty circumstellar disc is expected to outshine the stellar photosphere at wavelengths longer than $\sim 2\mu$m. This means that space-based observatories such as *WISE* (Wright et al., 2010), *Spitzer* (Werner, 2005) and *JWST* (Gardner et al., 2006) are well-equipped to measure infrared excess from the warm debris discs. The lifetime of the disc is also an unlikely culprit: comparison of accreted metal masses of DBZ and instantaneous accretion rates for DAZ [8], constrains the lifetime range from $3 \times 10^4 - 5 \times 10^6$ yrs (Girven et al., 2012); in reasonable agreement with theoretical models (Rafikov, 2011b). Possible solutions for

[8] Taking the DBZ convection zone as lower limit of the total disc mass, and assuming no difference in the architecture and evolution of discs around DBs and DAs (Jura et al., 2007).

the dearth of detections suggest an inherent faintness, due to a reduced surface area (e.g. Rocchetto et al., 2015) or an optically thin nature, as opposed to the opaque and optically thick assumptions (Jura, 2003). Additionally, a recently compiled catalog triplicates the sample of WD candidates with infrared excess, but follow-up is required to extract the systems harbouring a dusty disc that could help alleviate the discrepancy (Madurga Favieres et al., 2024).

Even though planetary debris transits are difficult to observe, as they require high inclinations, at least a dozen candidates show optical photometric transit variability (Guidry et al., 2021; Bhattacharjee et al., 2025), with five confirmations exhibiting a wide range of periods: WD 1145+017 ($P \simeq 4.5 - 4.9$ hrs, Vanderburg et al., 2015), ZTF J1944+4557 ($\simeq 4.97$ hrs, Guidry et al., 2025), WD J0139+5245 ($P \simeq 100$ d Vanderbosch et al., 2020), WD J0328-1219 (showing two periods of $\simeq 9.94$ and 11.2 hrs, Vanderbosch et al., 2021) and WD 1054-226 ($\simeq 23$ min, Farihi et al., 2022).

Unlike the rare transit events, up to $\simeq 70\%$ of dusty white dwarfs have been observed in *WISE* to show significant infrared variations (Swan et al., 2019), independent from viewing geometry. Stellar pulsations can cause changes in the infrared brightness of the disc (Patterson et al., 1991). However, this variability, when independent from temperature, usually signals structural changes (Xu & Jura, 2014). A decrease of luminosity can be explained if the disc surface area contracted. This contraction can be due to a planetesimal impact (Jura, 2008), or by a runaway accretion event due to interactions with an inner gaseous disc (Rafikov, 2011a; Rafikov & Garmilla, 2012; Metzger et al., 2012). Fresh dust generation from tidal disruption (Xu et al., 2018) can cause a sudden increase of infrared emission. Additionally or alternatively, planetesimal collisions could trigger production and destruction of dust and gas, as invoked to explain a rise and fall by $\simeq 20\%$ in the infrared flux of GD 56 (Farihi et al., 2018). Regardless of the processes responsible for creation and depletion of gas and dust, it is clear that interaction of these two components plays a protagonist role in the infrared variability.

Gaseous debris disc

While dusty WDs are rare, an even smaller subset is that of gaseous disc components. A large spectroscopic survey of single WDs from SDSS was analysed in search of the gaseous telltale: double-peaked emission from the Ca II 8600 Å triplet. Only $\simeq 0.067\%$ displayed the emission (Manser et al., 2020), with a total of 22 WD gas discs detected to date (Gänsicke et al., 2006b, 2008, 2007; Southworth et al., 2007; Melis et al., 2010, 2012, 2020; Brinkworth et al., 2012; Debes et al., 2012;

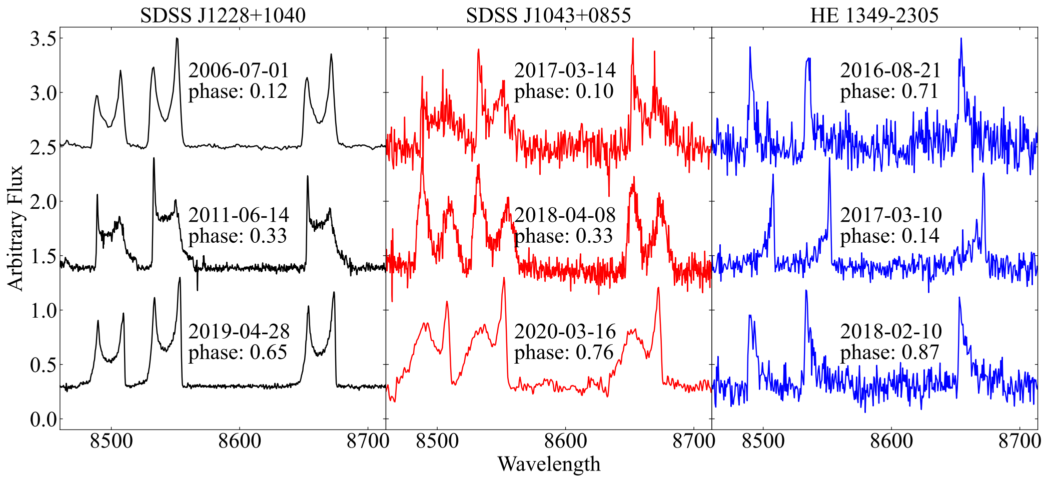

Figure 1.11: Asymmetric double-peaked structure of the Ca II triplet gas emission of SDSS J1228+1040 (left), SDSS J1043+0855 (middle), and HE 1349–2305 (right). Each panel shows spectra taken at various phases of each of the corresponding precession periods: $\sim$25 yr, $\sim$4.5 yr, and $\sim$1.3 yr, respectively. The spectra were normalised to illustrate the diversity of morphological structure and the different variability timescales. Data provided by Christopher Manser (private communication).

Bhattacharjee et al., 2025).

The emission from the gas component is likely generated after UV radiation incoming from the WD photoionises the gas after heating it up to several thousand Kelvin (Melis et al., 2010; Kinnear, 2011). As discussed in Section 2.4, the double peaked shape is then formed from the Doppler shifts of the Keplerian orbits (Horne & Marsh, 1986). Both the overall relative strength (Wilson et al., 2014, e.g.), as well as the morphology of the Doppler shifted peaks(e.g. Manser et al., 2016a, 2021) have shown long-term variability with a range of periods of $\simeq 1.3 - 25$ yrs (see Fig. 1.11).

As mentioned in the previous Section, one of the possible mechanisms behind infrared variability is collisional production and destruction of gas and dust (Farihi et al., 2018). Different collisional models have been put forth, such as collisional cascades of bodies (Kenyon & Bromley, 2017; Swan et al., 2021), or a tidal stream colliding within a pre-existing disc (Malamud et al., 2021). However, Manser et al. (2019) also uncovered short-term variability ($\simeq$123 min) in the shape and strength of the emission lines of SDSS J1228+1040. The variability was interpreted as a signature of a solid-body planetesimal orbiting in a precessing orbit within the dust disc, and so producing emitting gas. While confirmation in other systems is still pending, these results suggest that double-peaked emission variability could serve as proxy for embedded planetesimals; which would naturally explain the wide range in variability periods, if assuming different sized orbits.

Indeed, the morphological variability has been succesfully modelled with an eccentric structure precessing with a fixed period due to relativistic effects (Cauley et al., 2018; Miranda & Rafikov, 2018; Goksu et al., 2024). Doppler tomography (see Section 2.4), an indirect imaging method, has also shown an elliptical shape in the discs of SDSS J1228+1040 (Manser et al., 2016a) and HE 1349-2305 (Manser et al., 2021). With the same method, I show in chapter 5, that the elliptical assumption is also valid for a third object: SDSS J1043+0855.

1.5 Thesis Outline

In this thesis I will describe and discuss the research I made on three diverse cases of accreting white dwarfs. In Chapter 2, I describe the main spectroscopic instruments employed, and mention the reduction methods used for the respective observations. I also delve into the Doppler tomography indirect imaging technique, and briefly discuss five images for distinct systems I produced. In Chapter 3, I discuss the results obtained for V3101 Cyg and the major implications for CV evolution. Chapter 4 discusses the modulation analysis of WD 0141–675, and the tentative signal found which contests the retraction of the astrometric detection. In Chapter 5, I exhibit the third Doppler tomography of the select WD gaseous disc population, and update the two previously published. This Chapter shows the range of variability periods in the morphology of the Ca II emission, as well as showing a consistent tomography shape across all three objects, suggestive of a common origin. Finally, the general conclusions are laid out in Chapter 6, as well as future work designed to complement the accomplished results.

Chapter 2

Methodology

"Begin at the beginning, and go on till you come to the end: then stop."

Lewis Carrol

Electromagnetic radiation is the keystone to understanding celestial bodies. In particular for this thesis, three spectrographs were employed for the analysis of the objects of study. In this Chapter, I describe the general properties of the instruments. Methods used throughout this Thesis such as Radial Velocity and the Lomb-Scargle Periodogram are also described here. Finally, the method of Doppler Tomography, employed in Chapter 5, is devoted special attention in Section 2.4, given its particular potential to interpret the behaviour of spectral features in accreting white dwarfs.

2.1 Instruments

2.1.1 HST Cosmic Origins Spectrograph

Since its installation on the *Hubble Space Telescope* (HST), the COS has made a major impact in the study of faint UV light sources. It therefore has been a useful tool in the analysis of WDs whose emission peaks in this wavelength range (Gänsicke et al., 2006a). This versatile instrument is equipped with two independent observing channels: (1) a Far-Ultraviolet (FUV) detector operating in the wavelength range of $\simeq 900 - 2140$ Å and (2) a Near-Ultraviolet (NUV) detector sensitive to wavelengths between $\simeq$ 1650–3200 Å. The channels can utilize either a medium-resolution ($R \sim 20\,000$) or low-resolution($R \sim 3\,000$) grating. COS has two circular science apertures available: the Primary Science Aperture (PSA) and the Bright

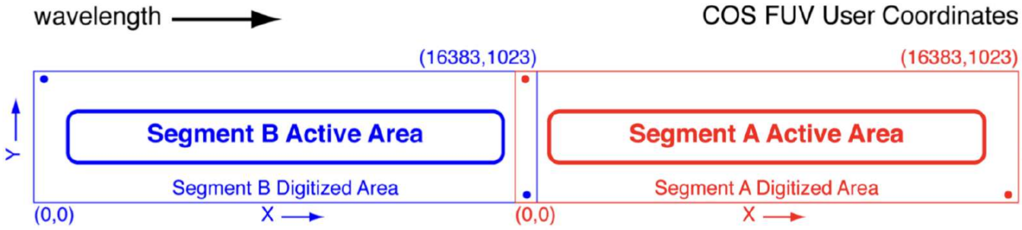

Figure 2.1: FUV COS detector showing the FUVA segment (red) and the FUVB (blue) segment. Figure taken from the COS instrument handbook (Soderblom, 2023).

Object Aperture (BOA) (Soderblom, 2023). For the particular case of the cataclysmic variable V3101 Cygni in Chapter 3, the observations were made in the FUV channel, with the PSA and a medium-resolution grating (G130M).

The FUV detector is composed of two segments with a gap ($\sim$ 9 mm wide) separating the active areas (see Fig. 2.1). The wavelengths that fall in the gap are not recorded, but choosing an alternate central wavelength setting (CENWAVE) for complementary observations circumvents this issue. In particular, for Chapter 3, I used the CENWAVE settings of 1222 and 1291 Å, which enable full coverage of each other's gaps (see Table 2.1). Furthermore, different positions are selected for the gratings (FP-POS=1–4) to shift the spectrum slightly in the dispersion direction, thus minimising the effects of fixed pattern noise. All FP-POS were used for our object of study (See Table 3.1).

Table 2.1: COS grating setup for V3101 Cyg in Chapter 3.

Channel	**Grating**	**Central W.l. (Å)**	**Segment B (Å)**	**Segment A (Å)**
FUV	G130M	1 222	1 067–1 207	1 223–1 363
		1 291	1 134–1 274	1 291–1 431

Sub-Exposure Splitting and Lightcurve Extraction

The detector can be set in either TIME-TAG or ACCUM mode. TIME-TAG records the position and arrival time of each detected photon; as well as a pulse height, which discriminates real events from electronic noise or cosmic events. Alternatively, ACCUM mode only records their position. Due to its many advantages, we used the TIME-TAG mode, which allows for temporal sampling, discrimination of poor quality data, thermal correction and background removal (by using the pulse-height values). I took advantage of this setting by splitting the observations of V3101 Cyg (Chapter 3) in sub-exposures of $\sim 1/10$ of the orbital period, in order to perform Radial velocity studies. This was done by following the Jupiter Notebooks developed by Space Telescope Science Institute. The specific Python function used for the splitting of the exposures in Chapter 3 was Splittag.

Next, I ran the CalCos pipeline on each sub-exposure to extract the one-dimensional spectra. This pipeline performs a series of corrections using associated reference files (see Frazer et al., 2024), such as geometric, flat field, deadtime, and Doppler corrections, as well as Pulse-height filtering. The one-dimensional spectra are also wavelength-calibrated with the count rates converted to flux densities. COS has an onboard wavelength calibration system that uses two Pt/Ne emission line lamps and two D_2 lamps. This set of lamps illuminates the flat field aperture and the wavelength calibration aperture. All apertures are on a common aperture plate, so that the offset between the wavelength calibration aperture and the PSA and BOA is fixed. This calibration system typically achieves a wavelength precision better than $8\,\mathrm{km\,s^{-1}}$ for its medium resolution spectra (Osterman et al., 2011). This systematic instrumental error was included in the uncertainty calculation of the radial velocity analysis of Chapter 3. Furthermore, by integrating the desired wavelength range, TIME-TAG mode can also be used to compute a lightcurve with the chosen exposure time. We utilized the LIGHCURVE Python package developed by Ely et al. (2015), selecting exposure time of 5 s and and masking the geocoronal emission lines from Ly α ($\simeq$ 1216 Å) and O I ($\simeq$ 1300 Å).

2.1.2 ESPRESSO

The Echelle SPectrograph for Rocky Exoplanets and Stable Spectroscopic Observations (ESPRESSO) is an ultra-stable high resolution spectrograph. This instrument is fiber-fed and cross-dispersed. It was installed at the Very Large Telescope (VLT) in Paranal, Chile, in 2017, starting regular operations in October 2018. This instrument has improved the instrumental radial-velocity precision, allowing to explore new frontiers in the search for exoplanets (Pepe et al., 2021). Its optical configuration is designed to minimise the size its optics (González Hernández et al., 2018, see also Fig. 2.2).

ESPRESSO is able to observe with any of the four Unit Telescopes (UTs) of the VLT at a spectral resolving power of $\sim$140 000 within the optical range of $378.2-788.7$ nm. In the 4-UT mode, all four Unit Telescope (UT)s can be combined together to to form a 16-m equivalent telescope, while still providing a resolving power of 70 000.

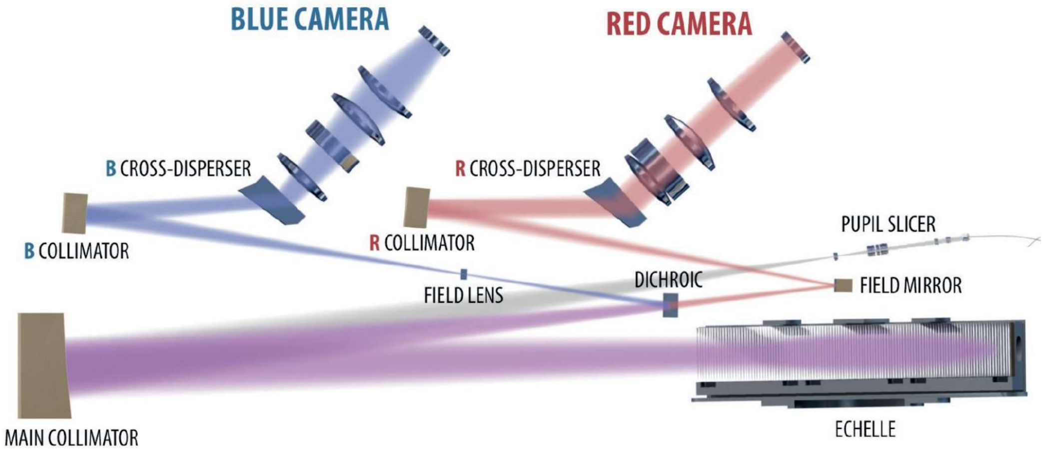

Figure 2.2: Optical layout of ESPRESSO. Figure taken from (González Hernández et al., 2018).

The ESPRESSO data can be reduced using the Data Reduction Software2 (DRS v3.0.0). provided by ESO and the ESPRESSO Consortium (Pepe et al., 2021) The DRS performs standard Echelle spectrum reduction, including bias and dark subtraction, optimal order extraction, bad pixel correction, flat-fielding, deblazing, wavelength calibration, and order merging. The default wavelength calibration employs a combination of a thorium-argon hollow-cathode lamp and a Fabry-Pérot interferometer (Wildi et al., 2012); a design with a wavelength solution that reaches an extreme precision of $10\,\mathrm{cm\,s^{-1}}$ (Figueira et al., 2025).

For the analysis of WD 0141-675 (Chapter 4), observations in single telescope mode, slow read-out and 4×2 binning (spatial$\times$spectral) were obtained. They were then calibrated, order-merged and deblazed with the DRS pipeline. Using the MOLECFIT package[1], the telluric lines were also removed (Kausch et al., 2015; Smette et al., 2015). Our reported radial velocity uncertainty in Chapter 4 greatly exceeds the instrumental systematic error $10\,\mathrm{cm\,s^{-1}}$, therefore it was not included in the analysis.

2.1.3 X-Shooter

The X-Shooter Echelle spectrograph is mounted on the UT3 of the VLT in Paranal. It is a single-target with intermediate-resolution (R$\sim$ 4 000 – 17 000). Through the use of two dichroics, the light is split into three channels (or arms) (Vernet et al., 2011): UVB (3 000 – 5 500 Å), VIS (5 300 – 10 500 Å), and NIR (9 800 –

[1]see also *Astroclimes*, for a package to study telluric lines (Fetzner Keniger et al., 2025)

25 000 Å). Each of the three channels operates as an independent cross dispersed echelle spectrograph with individual slit masks and shutters.In particular, due to their broad wavelength coverage and intermediate resolution, the UVB and VIS arms are ideal to detect key optical features of WDs, in order to investigate the accretion of metals.

In Chapter 5, I illustrate the potential of the VIS arm, by studying the Ca II triplet variations of WDs with planetary gaseous debris discs. These debris discs exhibit infrared excess at about $\sim$ 22 000 Å, outside the range of the NIR arm, therefore the analysis of this channel was deferred for future work. These observations were reduced using the REFLEX reduction workflow with the standard settings (Freudling et al., 2013). The data reduction pipeline uses a ThAr hollow-cathode arc lamp for wavelength calibration. The wavelength calibration achieves an accuracy better than $2\,\mathrm{km\,s^{-1}}$ in the VIS arm and better than $4\,\mathrm{km\,s^{-1}}$ in the UVB and NIR arms (Vernet et al., 2011). These systematics were not included in the radial velocity analysis of Chapter 5, since they are far smaller than the reported uncertainties in the VIS arm. Analogous to the ESPRESSO observations, the X-Shooter observations were telluric corrected with MOLECFIT (Kausch et al., 2015; Smette et al., 2015). The additional observations used for Chapter 5 were obtained already calibrated from scientific archives.

2.2 Radial Velocity Method

The periodic orbital motion of two celestial bodies around a centre of mass causes the respective spectral lines to become Doppler-shifted to an observer, with over ~1100 exoplanets having been discovered via this technique (Wright, 2018; Trifonov, 2026). Assuming orbital motions far smaller than the speed of light, the radial velocity (having the direction of the line of sight) will be affected as follows by the Doppler effect: (V_r):

$$\frac{V_\mathrm{r}}{c} = \frac{\lambda_\mathrm{obs} - \lambda_\mathrm{rest}}{\lambda_\mathrm{rest}} \tag{2.1}$$

Where c is the speed of light, and λ_obs and λ_rest are the observed and rest wavelengths of the spectral feature, respectively.

If enough spectroscopic observations are available to cover the periodic cycle, the velocity of the stellar component can be modelled by fitting a sine wave of the form[2]:

$$V(t) = \gamma + K \sin\left(2\pi \frac{t - t_0}{P}\right) \tag{2.2}$$

where γ is the systemic velocity, P is the orbital period, and K the velocity amplitude. Considering an orbital inclination i different from zero, $K \sin i$ then represents the true orbital velocity of the stellar component. The value of t_0 is usually taken as that of the inferior conjunction, that is, when the position of the secondary is closest to the observer.

A variety of methods are employed to measure the Doppler shifts of the individual observations, with their main limitation being the wavelength calibration of the spectrograph (see Section 2.1).

1. A standard approach consists of fitting a Gaussian, Lorentzian or Voigt profile to the spectral line, and adopting the mean as the observed wavelength $\lambda_{\rm obs}$ (e.g. Ramírez et al., 2025). The use of cross-correlation of atmospheric models with observed spectra is also common practice (e.g. Chapter 3).

2. When the shape of the spectral feature appears morphologically distorted or asymmetrical a convolution method can be applied. For example, for double-peaked lines generated by accretion discs (see also Section 2.4), convolution of the spectral line with the derivative of a Gaussian or a double-Gaussian profile is standard practice (Schneider & Young, 1980; Ramírez et al., 2022). In particular, this convolution method traces the motion of the line-wings, which originate in the inner regions of the accretion disc, whose radial velocity is expected to closely reflect the motion of the WD component in CVs (Shafter, 1985; Shafter et al., 1986).

3. A method especially useful for radial velocity measurements in asymmetric emission lines, is the so-called Cumulative Equivalent Width (CEW). This method calculates the equivalent width across a variable wavelength range sweeping over the emission line (e.g. Dennihy et al., 2018; Manser et al., 2021). The CEW function naturally starts from zero (assuming a non-contaminated continuum); it progressively increases as the extending range covers an increasing fraction of the spectral feature; and it finally plateaus when the full line has been completely covered by the variable wavelength range. The wavelength position of the mean (or the median) of the CEW is then selected as the centroid of the emission line.

[2]Assuming a circular orbit

4. Finally, it is worthwhile listing the Violet-over-Red method, implemented in Chapters 4 and 5. It consists in dividing the emission line by two wavelength sectors: a blue and red wavelength range (e.g. Manser et al., 2019; Ramírez et al., 2025). Then, the ratio between these two sectors is obtained. Strictly speaking, this is not a radial velocity measurement, and in this work it was employed as a proxy to constrain the variability period of the spectral features. However, provided a good spectral resolution, a velocity centroid can be inferred from this method.

In this Thesis, the radial velocity uncertainties were only statistical, except for those of Chapter 3, where the systematic instrumental error was included. These uncertainties are therefore somewhat optimistic, although, as mentioned in Sections 2.1.2 and 2.1.3, said instrumental error is negligible.

2.3 Lomb-Scargle Periodogram

As is clear from Eq. 2.2, a good radial velocity amplitude measurement requires a well-constrained orbital period P. The Lomb-Scargle period search technique (Lomb, 1976; Scargle, 1982) is a commonly employed method in astronomy (Ramírez et al., 2022; Hernández-Díaz et al., 2025). It estimates the Fourier power as a function of oscillation frequency f by fitting a sinusoid function of the form $y(t) = A\cos(2\pi f\, t) + B\sin(2\pi f\, t)$: for each frequency, it optimises the A and B coefficients and evaluates the residual variance after the fit. This method is specifically useful to unveil periodic signals in unevenly sampled data (see VanderPlas, 2018, for a detailed review).

The validity of the found frequency in the Lomb-Scargle can then be assessed by calculating its False Alarm Probabilityy (FAP) (e.g. Rogers et al., 2024a; Ramírez et al., 2025). The usual approach consists in generating synthetic datasets and computing their Lomb-Scargle periodogram. The number of periodograms showing a peak with a strength equal or higher to the observed dataset are recorded to calculate the frequency of this event. A threshold is then defined (usually 0.01), and if the frequency exceeds this threshold, the signal is discarded. A more sophisticated method that avoids large-scale simulations is that developed by Baluev (2008). It instead interprets the Lomb-Scargle as a continuous random process, and uses extreme-value statistics techniques to analytically determine the probability of a power peak being caused by noise. This approach has the advantage of being computationally efficient and avoiding the need for extensive Monte Carlo simulations. It accounts for the uneven time-sampling inherent to ground-based radial velocity observations. However, the method assumes that the noise is independently and identically distributed (i.i.d.) and Gaussian. These conditions are approximately met when measurement uncertainties are well-characterised and stellar activity or instrumental systematics do not dominate the residuals. In practice, radial velocity datasets may contain correlated noise contributions from stellar jitter or scheduling-induced aliasing, which can cause the FAP of a signal to be underestimated.

In this Thesis, after the signals were validated with the FAP, the uncertainties were calculated by fitting a Gaussian to the selected periodogram signal. When this was not possible, a sine wave fit with the period as a free parameter was made to the data (see Section 2.2), and the statistical uncertainty from this fit was adopted for the period.

2.4 Doppler Tomography

Doppler tomography is an indirect imaging technique that analyses time-resolved spectra of a binary, in order to map its emission distribution in velocity space. It does so by interpreting the morphological variations caused by Doppler shifts in spectral features (Marsh, 2001b, 2005). This technique was originally developed to study the accretion discs in CVs (Marsh & Horne, 1988), following analogous principles to those of medical Tomography; that is, to interpret projections at a series of angles in order to reveal information about the the higher-dimensional distribution.

A simple Keplerian disc generates a characteristic double-peaked emission structure, as illustrated in Fig. 2.3. This pattern is generated from the Doppler shift caused from the disc orbits having different radial velocity (see Eq. 2.1). It is worth noting that in the rotating frame for the Keplerian case, the regions of equal velocity magnitude in the disc are simply concentric rings. However, in the observer's inertial frame, the regions of equal radial velocity form a fixed dipole pattern in coordinate space (see Fig. 2.3).

The complex dipole pattern makes it difficult to translate the information of the spectra and obtain a tomography image of the disc. However, in velocity space the issue is greatly simplified, since constant radial velocities create a pattern of straight lines in velocity space (see Fig. 2.4). To illustrate this, let the coordinate space have the x-axis going from the WD to the donor, and the y-axis in the direction of motion of the donor (Fig. 2.4). This defines inertial speeds V_x and V_y that when projected onto our line of sight (Marsh, 2001a) produce radial velocities. The mathematical projection for the radial velocity (V_r) of an element with position

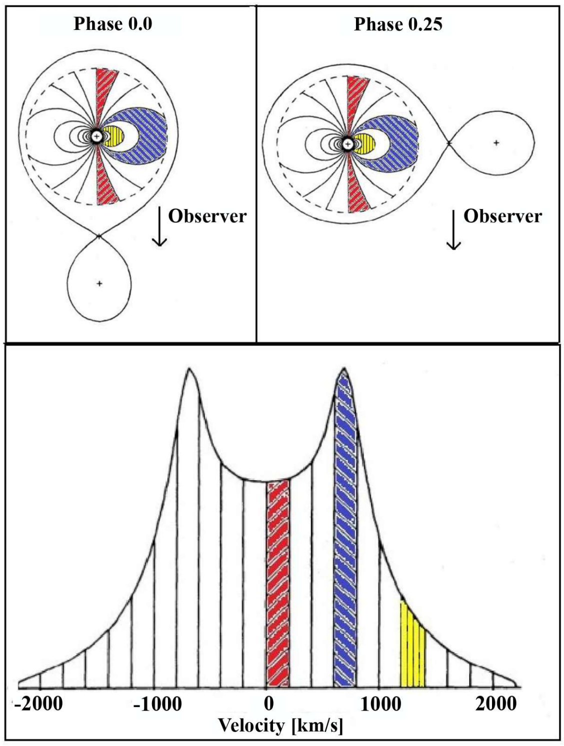

Figure 2.3: Formation of an emission line profile of an accretion disc. The top panels show the radial velocity pattern (in coordinate space) of the disc at phases 0.0 (left) and 0.25 (right). The bottom panel shows the resulting emission profile. Note that the radial velocity pattern remains fixed from an inertial frame perspective. Three different areas of the disc are colored-in to show their radial velocity correspondence in the emission profile. Figure modified from Horne & Marsh (1986)

(V_x, V_y) at orbital phase ϕ is given by (Marsh, 2005):

$$V_r(\phi) = \gamma - V_x \cos 2\pi\phi + V_y \sin 2\pi\phi \tag{2.3}$$

This linear dependence of V_x and V_y (for a fixed phase), gives the straight line projection in velocity coordinates (see left panel of Figure 2.4); however, in the rotation frame the angle that the lines of equal radial velocity make with the axes, will vary with the orbital phase (see Figs. 1 and 2 of Marsh, 2005). It follows that for each orbital phase, the velocity (V) line profile $f(V, \phi)$ in Figure 2.3, becomes a simple projection in the mathematical sense of integrating the image $I(V_x, V_y)$ in velocity space:

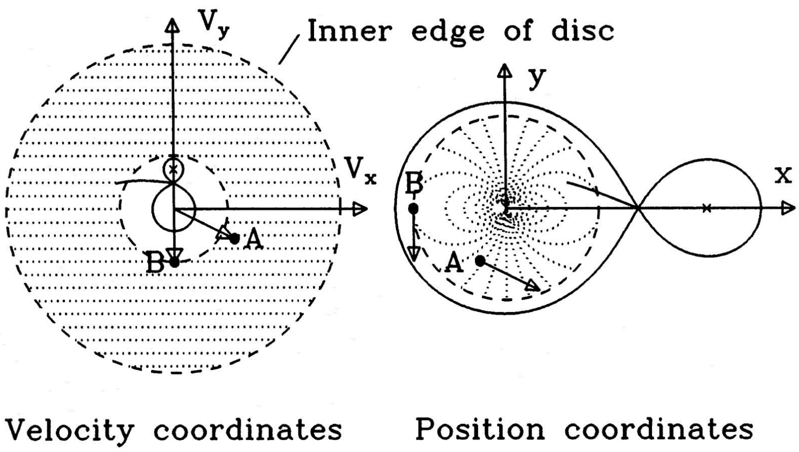

Figure 2.4: Schematic illustration of the transformation from velocity (left) to spatial (right) coordinates. The spatial configuration corresponds to orbital phase 0.25, assuming the observer lies below the page (By convention, phase 0.0 is defined when the donor star is in front of the accretor). In this case, the set of lines defining constant radial velocity in the rotating frame in velocity space are horizontal, i.e. the line of sight is aligned with V_y. However, as the binary rotates, the angle of the constant radial velocity lines would rotate as well, given the fixed position of the observer. The equivalent positions in each space of two elements (A and B) is also shown. Image reproduced from (Marsh, 2001a).

$$f(V, \phi) = \int_{-\infty}^{\infty} \int_{-\infty}^{\infty} I(V_x, V_y) g(V - V_r)\, dV_x\, dV_y \tag{2.4}$$

Where g is the normalised local line profile shape, that accounts for effects such as instrumental blurring.

Doppler tomography consists precisely in the inverse process of this projection, that is, $back\!-\!projecting$ the spectral line profiles (see Fig. 2.5) onto the rotating frame in velocity, where stationary accretion flows are independent of time (Cherepashchuk, 2022). The so-called filtered-back projection is a two-step process of (1) filtering each spectrum to limit the propagation of noise (Marsh, 2001a) and (2) inverting Equation 2.4, to obtain the image in velocity space (see Marsh & Horne, 1988, for a detailed derivation):

$$I(V_x, V_y) = \int_{0}^{0.5} \tilde{f}(\gamma - V_x \cos 2\pi\phi + V_y \sin 2\pi\phi, \phi)\, d\phi \tag{2.5}$$

Where $\tilde{f}(V, \phi)$ is the filtered profile as a function of velocity and orbital phase (Marsh, 2005).

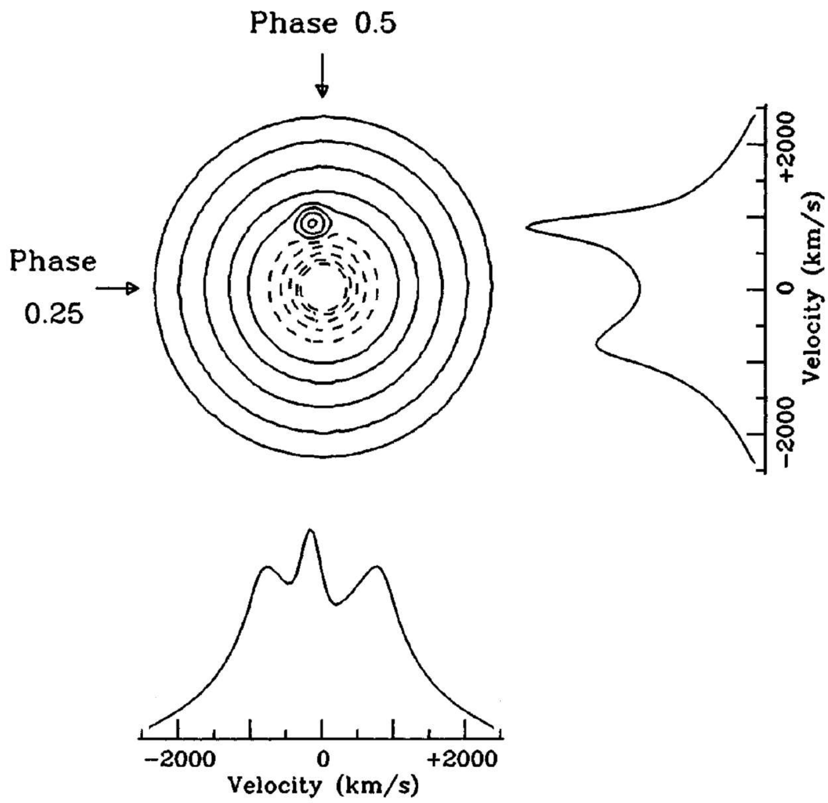

Figure 2.5: Schematic illustration showing the relation of spectral emission profiles as projections of an image in velocity space, with the direction of the projection dependent on the orbital phase. Image reproduced from (Marsh, 2005).

An alternative inversion technique is the Maximum Entropy Method (MEM) (Horne, 1985). It consists in optimising a combined objective function, that uses a regularisation parameter, α, that controls the balance between data fidelity and entropy maximization (Skilling & Bryan, 1984; Spruit, 1998):

$$F = \chi^2 - \alpha \cdot S \tag{2.6}$$

where χ^2 measures the deviation between the reconstructed and observed spectra and minimises when when the observations are matched exactly; and S is the entropy of the image relative to a default map that gets maximised for 'smooth' maps. A standard form of the entropy that measures departures from a default image is described by (Marsh & Horne, 1988):

$$S = -\sum_{i=1} p_i \log \frac{pi}{qi}, \quad p_i = \frac{I_i}{\sum_j I_j} \quad \text{and} \quad q_i = \frac{D_i}{\sum_j D_j} \tag{2.7}$$

Where I_i pixel value of the image of interest at pi, and D_i is the pixel value of the default image at q_i. The condition from Eq. 2.6 differs from a simple χ^2 minimisation given that there are infinitely many images that will fit the data equally well. By including the optimisation of the entropy term encodes an *A priori* assumption: the disc structure is expected to be smooth. This is equivalent to selecting the most featureless image from the possible solutions.

The initial default image used to maximise the entropy is typically computed from models of discs, with radial decay and azimuthal symmetry (Horne, 1985). Next, a heavily smoothed version of the current map at each iteration is used. This dynamic default promotes smooth structures rather than completely uniform images (Marsh & Horne, 1988; Spruit, 1998).

Doppler tomography assumes 5 axioms (Marsh, 2001b):

1. The visibility of all elements in the binary is constant.
2. In the rotating frame, the flux at every fixed point remains constant.
3. The direction of motion at every point is parallel to the orbital plane.
4. The velocity vectors rotate with the binary system.
5. The intrinsic width of the line profile (e.g. thermal) from any point is negligible.

In practice, these axioms are not always satisfied. For example, eclipsing systems might fail to meet the first axiom; whereas jets, winds or magnetic channeling of the accretion stream break the third condition. This can cause spurious artifacts in the tomography images, so their interpretation must be made with caution.

All the Doppler tomography images computed in this thesis were made with the code PyDoppler, published by Hernandez Santisteban (2021), which is a Python wrapper of the MEM routines developed by Spruit (1998).

2.4.1 Interpretation of Doppler Tomography Maps

As an example of how to interpret Doppler maps, I proceed to show the tomography I computed for different objects as complementary projects for this thesis. This exercise is mostly intended as a basic outlook on the interpretation of Doppler maps. The implications of the results in the broader context of the object types and their evolution is meant to be published elsewhere.

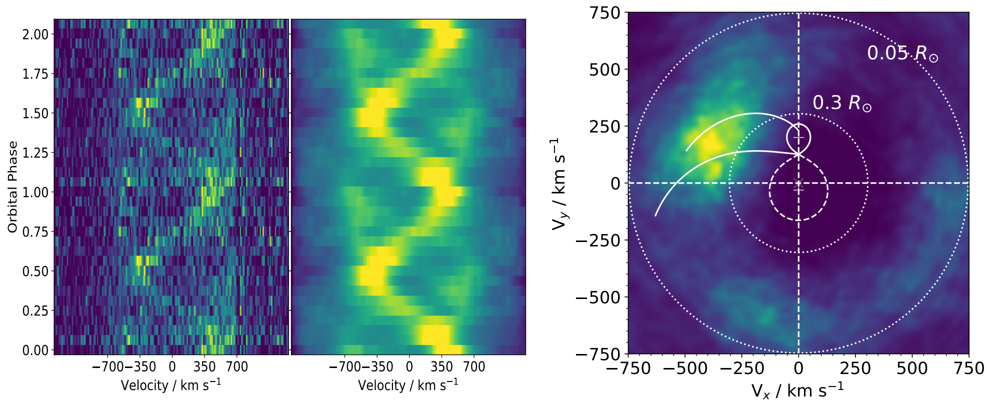

Figure 2.6: Observed trailed spectra (left), reconstructed trailed spectra from the tomography (middle), and Doppler Tomography image (right) of the He I 5875 Å emission of V1838 Aql. The Roche lobe of the companion (top lobe, in solid) and accretor (bottom lobe, in dashed) are plotted. The dotted circles indicate two rings of different radius, that illustrate the inversion of the Keplerian disc in velocity space. Finally, the curves originating from the companion's lobe are the Keplerian (top) and ballistic (bottom) trajectories of the gas stream. See text for details. The emission shows a diffuse disc overlaid with a hotspot caused from the stream-disc impact.

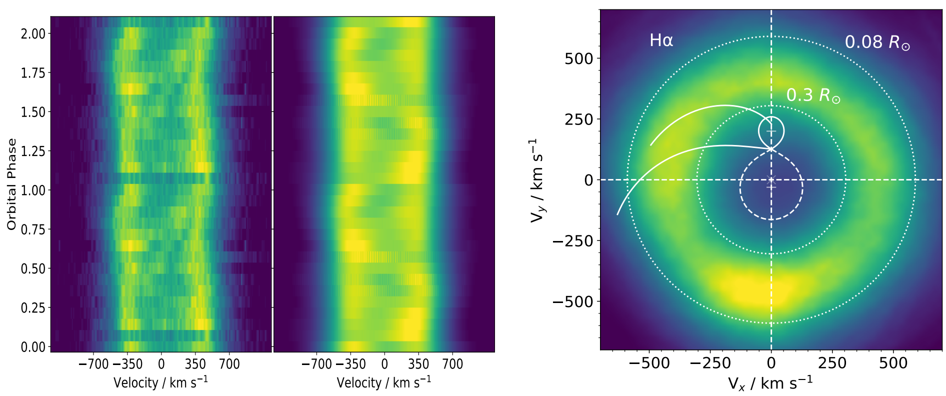

Figure 2.7: Same as Fig. 2.6, but for the Hα emission of V1838 Aql. The image shows a disc emission overlaid by a bright stucture in the lower quadrants, possibly related to a patchy disc or a secondary impact zone due to stream overflow.

V1838 Aql, A Dwarf Nova

V1838 Aql is a short period ($\sim$ 80 min), high proper motion DN, which was detected by amateur astronomer Itagaki on May 2013, during a strong Superoutburst and later classified as a WZ Sge object (Kato et al., 2014). An extensive photometric study during the super-outburst determined a mass ratio of $q = 0.10(1)$, derived from its superhump period excess (Echevarría et al., 2019). The results of these authors suggested a likely stellar nature of the donor approaching the period minimum, corroborated by its relatively high temperature estimation (Hernández Santisteban et al., 2019). Narrow-band imaging revealed an extended emission around the source after the outburst, interpreted as a bow shock. Such structure was presumed to be formed by a quasi-continuous outflow from the source in quiescence (Hernández Santisteban et al., 2019). Outflows are not expected in this state, but if confirmed, this additional sink of angular momentum could help alleviate the discrepancy between theory and observations regarding the position of the period minimum (See Section 1.3.5).

X-shooter observations of V1838 Aql during a quiescent state were provided (J.V. Hernandez-Santisteban, private communication). These were obtained in 2018 April, May 04 and May 14, with a coverage of three full orbits. The spectra show a plethora of emission features, including the Balmer line Hα and He I 5875. As mentioned above, I computed the Tomography of these emission lines using the code developed by Hernandez Santisteban (2021). I assumed the mass ratio derived by Echevarría et al. (2019), a low inclination of $\simeq 24°$, an orbital period of $\simeq$ 79 min, and a WD mass of $\simeq 0.83\,M_{\odot}$ (Zorotovic et al., 2011).

Figure 2.6 shows the computed tomography of He I 5875. The image shows the position of the Roche lobes in velocity space, with the superior one pertaining to the donor star, and the inferior one to the accretor. Since the donor co-rotates with the binary, its shape in velocity space is preserved, but rotated 90° due to the vectorial product relation of the velocity ($\mathbf{v}$), frequency (Ω) and radius ($\mathbf{r}$) $\mathbf{v} = \Omega \times \mathbf{r}$. In velocity space the Keplerian disc gets turned inside-out, with the outer/inner disc appearing at low/high velocities. The Figure highlights this inversion by showing a ring of $0.3\,R_{\odot}$ and a higher-velocity ring at $0.05\,R_{\odot}$.

The tomography reproduces the behaviour of the trailed spectra quite well. The trailed spectra shows a difuse double-peaked emission which in the tomography creates a weak disc structure. However, the emission is dominated by a blob structure in the top left quadrant. This is the canonic position of the bright spot (or hot spot), where the stream impacts the disc. This is illustrated by the curves stemming out of the donor's Roche lobe, which plot the Keplerian and ballistic trajectories of

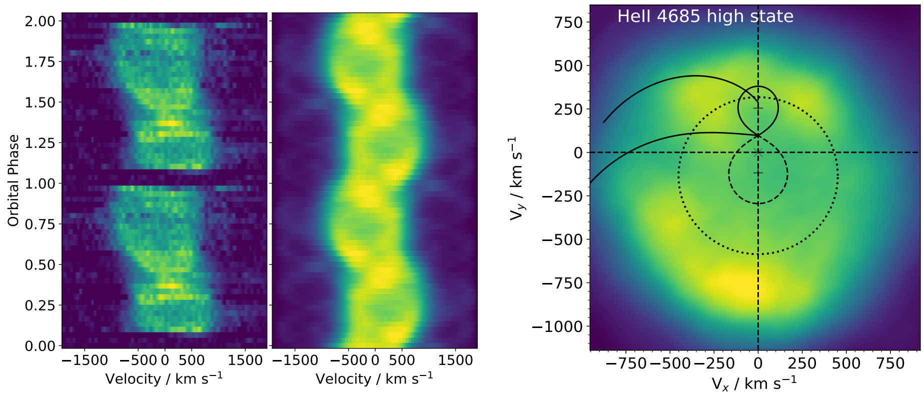

Figure 2.8: Same as Fig. 2.6, but for the He II 4685 Å emission of J 1948 during a high state. The tomography shows an asymmetric emission overlaying a diffuse disc structure, strongly hinting at the presence of spiral shocks.

the stream. In the trailed spectra, the hotspot can be observed as an $S-wave$ that oscillates from the red to blue peaks of the disc.

The Hα Balmer line, on the other hand, shows a much stronger disc emission, but does not exhibit a hotspot in its canonic position (See Fig.2.7). Instead an intense structure appears in the lower quadrants. This is suggestive of a secondary impact zone, or a patchy disc associated with a tidally thickened sector that becomes irradiated by the WD or inner disc, which can generate spiral structures in the images (e.g. Ogilvie, 2002; Neustroev et al., 2016). Regardless of its origin, the different tomography highlights the value of mapping different ions to better understand the disc architecture. The tomography shown here is consistent with that published by Hernández Santisteban et al. (2019), for observations obtained in 2013, signaling a stability of the disc structure in quiescent state, at least until the 2018 observations. The results presented here are intended for publication in Echevarria et al. (in prep)

Next, I show the tomography of the novalike J194827-131733, produced during different accretion states, which illustrates how this method can study the morphological evolution of discs.

J194827-131733, a novalike

J 194827-131733 (henceforth J1948) is an eclipsing novalike with a long orbital period that experiences recurrent stunted outbursts. I computed a tomography with observations taken during and after one of these outbursts. Optical spectroscopy was provided (Joaquín Meza and Odette Toloza, private communication) from the

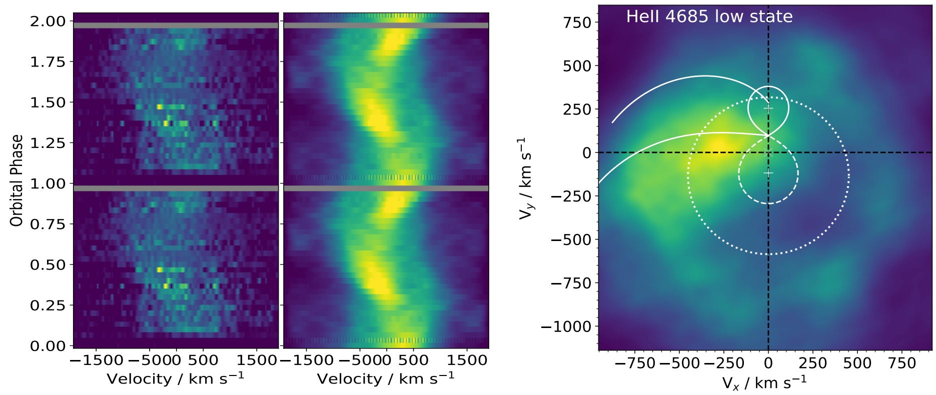

Figure 2.9: Same as Fig. 2.8, but for a low state. The tomography no longer displays the spiral arm structure as in the high state, and instead shows an emission close to the hotspot region, extending outside the tidal radius.

Intermediate Dispersion Spectrograph (IDS) mounted on the 2.5-meter Isaac Newton Telescope in la Palma. For the Roche lobe geometry we used an orbital period of $P_{\rm orb} = 5.19\,$hrs, a mass ratio of $q = 0.464$, the average white dwarf mass in CVs of $M_{\rm wd} \simeq 0.8\,{\rm M}_\odot$ (Pala et al., 2022; Zorotovic et al., 2011), and given the eclipsing nature, a high inclination of 85° was used (Meza et al. in prep).

The resulting Doppler tomogram for He II in the high state can be observed in the right panel of Fig. 2.8. It shows an asymmetrical spiral arm structure, bordering the tidal radius[3], and overlaying a weak disc emission. In particular, the bottom arm displays a higher flux than its top counterpart. This structure bears close resemblance to that observed in the dwarf nova IP Peg during outburst stages (Steeghs et al., 1997; Harlaftis et al., 1999); explained by tidal perturbations from the companion star that propagate inwards as waves, and result in spiral shocks (Matsuda et al., 1990; Spruit et al., 1987).

Intriguingly, in the low state of J 1948 (Fig 2.9, right panel) the spiral arms vanish, and instead an extended emission appears at the expected position of the hotspot along with a faded disc structure. These results, intented for publication in Meza et al. (in prep.), are suggestive that the spiral arms presence (or lack thereof) is the cause for the stunted outbursts in J 1948.

T CrB, a symbiotic star

T Coronae Borealis (T CrB) is a prototypical symbiotic recurrent nova, with an eruption recurrence of $\simeq$ 80 yrs, with its following nova outburst expected to be

[3]the theoretical maximum disc radius before tidal truncation from the companion (Hellier, 2001).

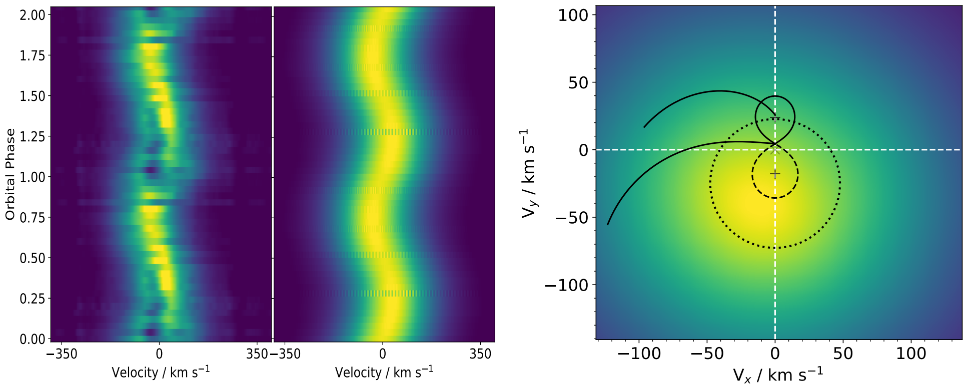

Figure 2.10: Same as Fig. 2.6, but for the Hα emission of T CrB. The tomography does not show a disc emission, instead, a brigt structure appears in the lower left quadrant, and decreasing radially from its center.

occurring soon ($\simeq 2026 - 2027$) (Schaefer, 2023). The components of the system are a WD and an M giant, with an orbital period of $\simeq$227 d (Kraft, 1958). The nova outburst is usually preceded by a so-called Super Active Phase (SAP), where enhanced mass is accreted onto the WD. The latest SAP of T CrB ended in 2023, suggestive of the imminence of the upcoming outburst. I computed the Doppler tomography of Hα in emission, during the latest SAP (2015-2023) of T CrB , using the 227 d orbital period and the parameters derived by Planquart et al. (2025): WD mass of $\simeq 1.32\,M_\odot$, mass ratio of $\simeq 0.74$ and inclination $\simeq 65°$. The observations were obtained from the ARAS spectral database compiled by amateur astronomers[4] of eruptive stars (David Boyd, private communication).

The tomography of T CrB does not display a clear disc structure, and instead it shows a bright emission centred in the lower left quadrant, decreasing its intensity radially from its centre. Intriguingly, this emission peaks outside the tidal radius (see Fig. 2.10). It must be noted that the trailed spectra is not well-reproduced. The tomography struggles particularly in phases $\sim 0.0 - 0.25$, during the inferior conjunction of the donor. This could imply that the emission might actually have a more complex structure. Planquart et al. (2025), found a consistent structure appearing in the lower quadrants, although their emission is more localised and peaks within the WD Roche lobe. However this difference is likely due to their higher resolution (R∼86 000).

The tomography of T CrB resembles that of the intermediate polar AE Aqr (e.g. Wynn et al., 1997; Ramírez & Echevarría, 2021), which could suggest that the

[4] https://aras-database.github.io/database/index.html

T CrB could be experiencing outflows, albeit with a different origin from that of the magnetic propeller, such as winds, as expected from the wind accretion in symbiotics (e.g. Carroll & Ostlie, 1996). However much caution is advised in interpreting tomography of symbiotic binaries, given that the flow dynamics are not expected to be constrained to the orbital plane.

The small compilation of Doppler tomography shown in this Section already illustrates the variety of image structure that binary systems can produce. As shown for the novalike J 1948 the method can probe how the disc can change in different physical states; or as is the case in the dwarf nova V1838 Aql, investigate the diverse morphology for distinct emission lines; or even detect outflows (as possibly for T CrB). These results clearly elucidate the great potential of Doppler tomography in the study of binary systems. And even though the method was originally devised for CVs as those in this Section, its applications are not limited to these compact objects. As a matter of fact, Doppler tomography has also been used to map the precessing gaseous debris discs of disrupted planetesimals around WDs (e.g. Manser et al., 2016a, 2021). In Chapter 5, I delve into this application by performing a follow-up on two of the previously mapped gaseous discs, and produce the first tomography of the gas disc around the WD SDSS J1043+0855.

Chapter 3

V3101 Cyg: A Cataclysmic Variable Descended From a Brown Dwarf+White Dwarf Pair

"What is now proved was once only imagined."

William Blake

3.1 Introduction

The evolution of cataclysmic variables, semi-detached binaries in which a low-mass star transfers mass to a white dwarf, is driven by angular momentum loss via gravitational radiation (Paczyński, 1967) and magnetic breaking (Rappaport et al., 1983). Most population models only consider cataclysmic variables born with main-sequence stars (Kolb, 1993; Howell, 2001; Pala et al., 2022), with initial orbital periods of several hours. Angular momentum loss results in the the mass of the companion, the binary separation and the orbital period decreasing, until the donor eventually reaches the hydrogen burning limit at $P_{\rm orb} \simeq 80\,{\rm min}$. At this point, the thermal time-scale outweighs the mass transfer time-scale and further mass-loss results in adiabatic expansion, which in turn causes an increase of the binary separation and the orbital period. The contrast between the large population of such short-period cataclysmic variables with brown dwarf donors predicted by models

(Kolb & Baraffe, 1999; Goliasch & Nelson, 2015; Belloni et al., 2018) and the small number of confirmed examples (Pala et al., 2019; Hernández Santisteban et al., 2018; Inight et al., 2023) is subject to ongoing observational (Muñoz-Giraldo et al., 2024) and theoretical efforts (Schreiber et al., 2023).

What is often ignored in this context is that cataclysmic variables can also be born with brown dwarf donors and $P_{\rm orb} < 80$ min, evolving towards longer periods upon the onset of mass transfer (Kolb & Baraffe, 1999). These systems could make up $\simeq 18\%$ of the entire population of cataclysmic variables (Politano, 2004). The existence of this formation channel is corroborated by the identification of post-common envelope binaries with brown dwarf companions (Maxted et al., 2006; Rappaport et al., 2017; Casewell et al., 2018) that will eventually evolve into cataclysmic variables.

To date, only SDSS J150722.30+523039.8 ($P_{\rm orb} = 66.6$ min), among several thousand known cataclysmic variable, was suspected to have formed with a brown dwarf donor (Littlefair et al., 2007). However, the space motion identifies this system as a halo member, and its short period can be explained by the evolution of a cataclysmic variable that formed with a metal-poor main-sequence donor.

V3101 Cyg was detected by Hideo Nishimura on 2019 July 12 when it brightened to nearly 8th magnitude during viscous thermal instability in the disc, which was followed by multiple re-brightenings (Tampo et al., 2020) (Fig. 3.1). With a distance of $d = 108.3 \pm 0.7$ pc (Gaia Collaboration et al., 2021), it is the 18th closest cataclysmic variable (Pala et al., 2019). The fact that this system had never been detected in outburst prior to 2019 implies an extremely long recurrence time, and consequently a very low mass transfer from the donor, which allowed the accretion disc to build-up enough mass for the uncharacteristically large-amplitude (Δmag $\simeq 9.5$) outburst. In this chapter we discuss what makes V3101 Cyg the best candidate known to date, to confirm cataclysmic variables descending from detached brown dwarf+white dwarf pairs.

3.2 Observations

3.2.1 *HST* COS Spectroscopy

We obtained Far Ultraviolet Spectroscopic observations of V3101 Cyg (Programme ID 16069) with the Cosmic Origins Spectrograph (COS) (Soderblom, 2023) on board the Hubble Space Telescope (*HST*) using the Primary Science Aperture (PSA), which has a 2.5 arcsec diameter (see Section 2.1.1). A first visit with two spacecraft orbits was obtained in 2020 Sep 12 (four orbits were intended but due to instrument issues two of them were discarded) and a second visit with four consecutive orbits was performed in 2020 Nov 21.

The COS instrument was set in the far-ultraviolet (FUV) channel configuration, using the G130M grating centred either at 1291 Å or 1222 Å (see Table 3.1), with a spectral coverage over a range of $\sim 1130 - 1430$ Å, and a spectral resolution of $R \simeq 18000$ at the central wavelengths. All permitted FP-POS positions $(1 - 4)$ were used, which move the spectrum slightly in the dispersion direction to improve signal-to-noise ratio and reduce the effect of flat-field artifacts. The 1291 Å central wavelength configuration has an instrumental gap between ∼1274–1291 Å, due to the space between the detector segments; analogously for the 1222 Å configuration, at the range of ∼1207–1223 Å.

The COS observations were obtained in TIME-TAG mode, a setup that records the time of encounter of each individual photon, allowing the observations to be split in sub-exposures. We did this by running the SPLITTAG Python module[1]. After splitting the file into segments we ran the CalCOS calibration pipeline (Soderblom, 2023) to re-extract the one-dimensional spectra. For the FUV channel, the pipeline includes pulse-height filtering and geometric correction, as well as flat field, dead-time, and Doppler correction, returning the one-dimensional, wavelength-calibrated spectra with the count rates converted to flux densities.

Finally, TIME-TAG data collection mode allows to study time variability by extracting a lightcurve from the observations (see Section 3.8). The geocoronal emission lines from Ly α ($\approx$ 1216 Å) and O I ($\approx$ 1300 Å) were masked in the lightcurve extraction procedure.

Table 3.1: Log of the *HST* COS observations of V3101 Cyg, taken in TIME-TAG mode with the G130M grating.

	Exposure	Date (start)	Time	MJD	Exp. time [s]	CWl [Å]	FP POS
1	le8z01eiq	2020-09-12	07:32:09	59104.31400248	2480	1291	3
2	le8z01eoq	2020-09-12	11:02:01	59104.45974322	1386	1222	2
3	le8z01eqq	2020-09-12	12:11:45	59104.50816915	1390	1222	3
4	le8z01esq	2020-09-12	12:37:18	59104.52591211	1386	1222	4
5	le8z04o2q	2020-11-21	05:34:56	59174.23260211	2480	1291	3
6	le8z04o4q	2020-11-21	07:03:01	59174.293771	2919.	1291	4
7	le8z04o6q	2020-11-21	08:38:22	59174.35998618	1390	1222	1
8	le8z04o8q	2020-11-21	09:03:55	59174.37772952	1386	1222	2
9	le8z04oaq	2020-11-21	10:13:45	59174.4262247	1390	1222	3
10	le8z04ocq	2020-11-21	10:39:18	59174.44396766	1386	1222	4

[1] See the Space Telescope Science Institute Jupiter Notebooks.

3.2.2 Long-Term Archival Photometry

The long term variability of V3101 Cyg was analysed with the AAVSO lightcurve, as well as with the Zwicky Transient Facility (ZTF) g and r-bands, and the *Gaia* g-band long term lightcurves (see Fig. 3.1).

The long term ligthcurves show a progressive increase of brightness right until the initial outburst occurs. The brightness then climbed ≈ 9.5 magnitudes reaching a peak at $V \approx 8.5$ mag, lasting 24 days. It was followed by a series of 7 rebrigthenings that reached a magnitude of ≈ 11 mag (see Hameury & Lasota (2021) for a detailed description of the rebrightenings)

The quiescent period increases from outburst to outburst, while the magnitude level in quiescence decreases progressively. However, the system has not yet recovered the quiescent level observed before the initial 9.5-mag outburst. We fitted a power law to the quiescent period occurring after the last brightening event, and estimated the system will cool down to its pre-outburst level on 2033 June (see Fig. 3.1).

3.2.3 SED Archival Photometry

We collected the available photometry obtained before V3101 Cyg went into an outburst state in 2019 (see Table), in order to make a Spectral Energy Distribution (SED) fit. As discussed in Section 3.5, this allowed us to measure the temperature of the system's components during the quiescent state.

Table 3.2: Archive Photometry used for the SED fit in ascending order of central wavelength.

Filter	Central WL	Flux	Error
PAN-STARRS_PS1.g	4810.16	2.42×10^{-16}	8.06×10^{-18}
GAIA_GAIA3.Gbp	5035.75	2.84×10^{-16}	2.82×10^{-18}
GAIA_GAIA3.G	5822.38	2.07×10^{-16}	8.49×10^{-19}
INT_IPHAS.gR	6153.45	1.39×10^{-16}	1.28×10^{-18}
PAN-STARRS_PS1.r	6155.46	1.77×10^{-16}	6.03×10^{-18}
INT_IPHAS.Ha	6568.19	2.29×10^{-16}	4.21×10^{-18}
PAN-STARRS_PS1.i	7503.03	1.02×10^{-16}	1.67×10^{-18}
GAIA_GAIA3.Grp	7619.95	1.50×10^{-16}	2.02×10^{-18}
INT_IPHAS.gI	7663.25	8.15×10^{-17}	2.25×10^{-18}
PAN-STARRS_PS1.z	8668.36	8.54×10^{-17}	4.86×10^{-18}
PAN-STARRS_PS1.y	9613.60	6.71×10^{-17}	1.44×10^{-18}
UKIRT_UKIDSS.J	12483.0	2.87×10^{-17}	5.96×10^{-19}
UKIRT_UKIDSS.H	16313.0	1.68×10^{-17}	3.97×10^{-19}
UKIRT_UKIDSS.K	22010.0	7.91×10^{-18}	4.23×10^{-19}

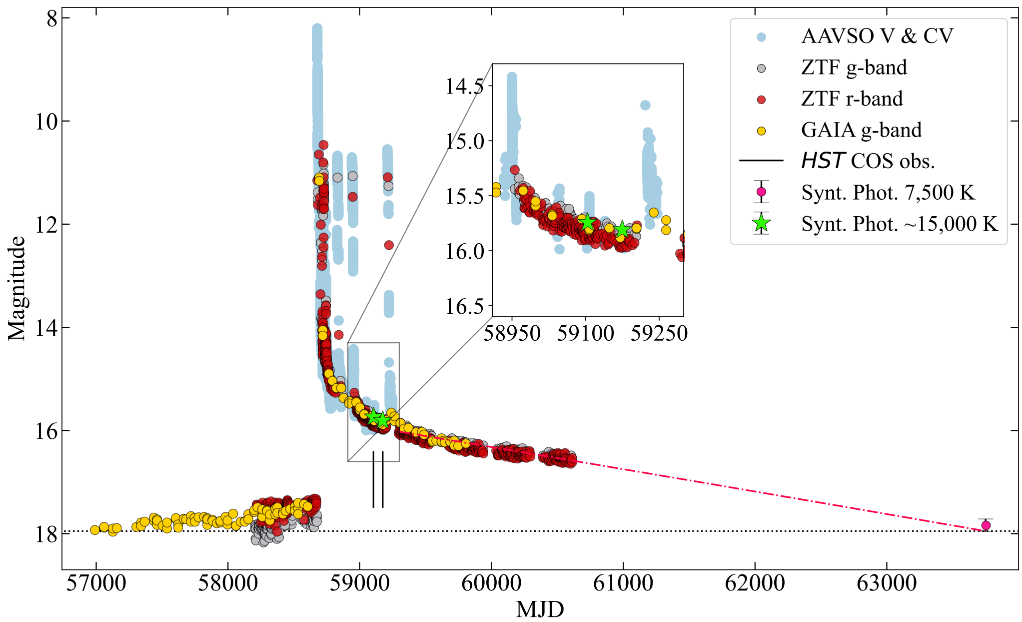

Figure 3.1: Long term light curve of V3101 Cyg. The photometric data from the AAVSO V and CV filters (light blue) ZTF g and r-band (grey and red, respectively) and *Gaia* g-band (yellow) trace the evolution of the system from deep quiescence through the outburst and the re-brightenings into the fading back to quiescence. The dashed black line indicates the quiescent magnitude of WD 0141–675 prior to the slow brightening that led to the 2019 July 12 superoutburst. The times of the two *HST* observations are indicated by vertical red lines. Synthetic V-band magnitudes computed from the best-fit white dwarf models (green stars) match the observations well. The white dwarf cooled by $\simeq 500$ K within 70 days between the *HST* observations (see inset). A power law fit (red dashed-dotted line) to the post-outburst light curve (excluding the re-brightenings) intersects the quiescent brightness in 2033 June, corresponding to a white dwarf temperature of $T_{\rm eff}$ = 7 000 K (pink circle).

3.2.4 Hα Excess

We positioned V3101 Cyg within a ($r'-$Hα) versus ($r' - i'$) colour-colour diagram made for a catalogue (Witham et al., 2008) of 4853 point source Hα emission-line objects selected from the INT/WFC Photometric Hα Survey (IPHAS) (Drew et al., 2005) (see Fig. 3.2). The diagram shows V3101 Cyg as a strong Hα emitter, and highlights the effectiveness of this selection method to detect cataclysmic variables from Hα excess developed in the literature (Witham et al., 2006). This approach is not biased against short-period systems, since these intrinsically faint objects with low mass transfer rate, usually have the largest Balmer equivalent widths. Therefore, more systems like V3101 Cyg can be unveiled using this method.

3.3 White Dwarf Spectral Atmospheric Parameters

We obtained the initial atmospheric parameters ($T_{\rm eff}$ and $\log g$) of the white dwarf from the flux-calibrated COS spectrum of each sub-exposures from both visits. To model the continuum, we generated white dwarf atmospheric model grids (Koester, 2010) for pure hydrogen atmospheres by fixing the rotational broadening ($v \sin i$) and abundances of strong absorption lines to an initial value that best matches the spectral absorption features visually. Then, we scaled the model fluxes using a Gaia parallax and a mass-radius relation (Althaus et al., 2013), and combined it with a constant flux to fit the continuum following a standard χ^2 minimisation technique as illustrated in Figure 3.3. The constant flux accounts for the additional contribution of the disc or boundary layer to the WD flux (e.g. Godon et al., 2017; Pala et al., 2017; Hause et al., 2017; Pala et al., 2022). While fitting, we masked the spectral regions that are affected by geocoronal or airglow emission lines to accurately model the continuum flux as shown in Figure 3.3.

Next, fixing the $T_{\rm eff}$, $\log g$ and constant flux to an initial best-fit value for each sub-exposure, we fitted the models to the spectral region (1250-1310 Å) dominated by strong absorption lines of Si, C and O in order to determine the $v \sin i$ and radial velocity of the white dwarf. The fits are performed for each sub-exposure which are then used to compute the orbital period of V3101 Cyg as shown in Figure 3.7 and described in later sections. We computed a $v \sin i$ of 47±4 km s^{-1} taking the average of individual sub-exposures. Finally, fixing the white dwarf models to this $v \sin i$ value, we determined the $T_{\rm eff}$, $\log g$, and hence the mass for each visit independently (as the two visits have different flux levels reflecting the cool-down of the white dwarf). The best-fit parameters for each visit are provided in Table 3.3.

Table 3.3: Atmospheric parameters of the post-outburst white dwarf obtained from the spectral fitting.

Parameter	Visit 1	Visit 2
$T_{\rm eff}$ (K)	15560 ± 67	15082 ± 106
$M_{\rm wd}$ ($M_{\odot}$)	0.48 ± 0.01	0.46 ± 0.01
$R_{\rm wd}$ ($R_{\odot}$)	0.0164 ± 0.0002	0.0168 ± 0.0002
$\log(g)$	7.68 ± 0.02	7.65 ± 0.02

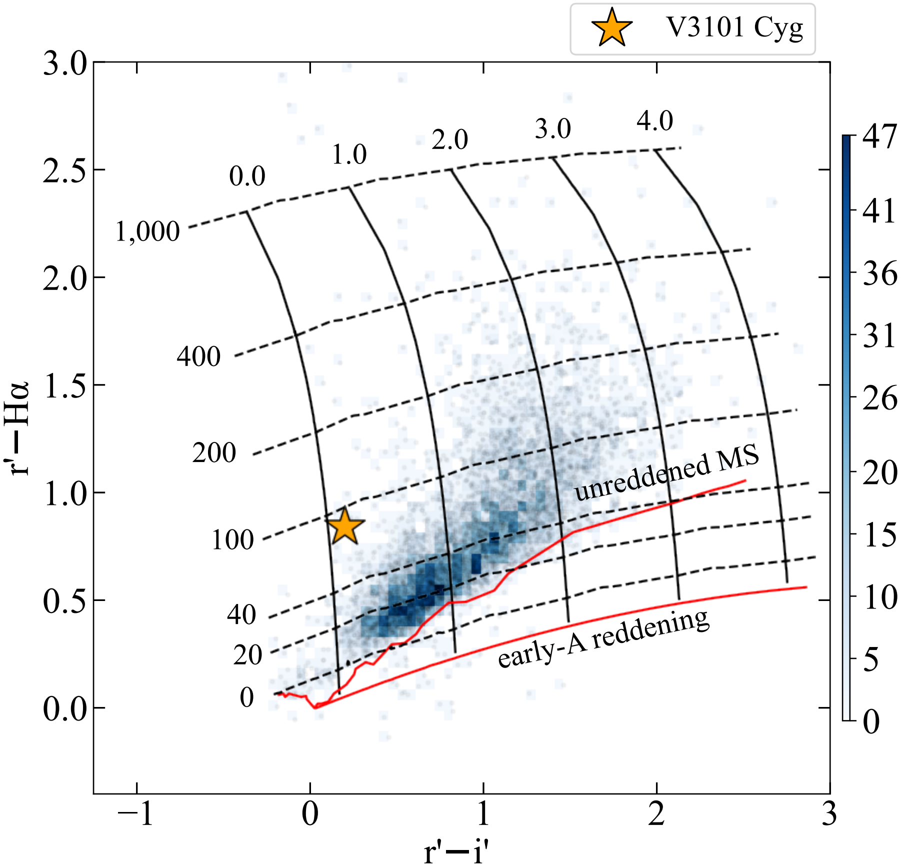

Figure 3.2: IPHAS colour-colour diagram, showing a distribution of strong Hα emitter candidates. The star symbol represents the position of V3101 Cyg. Each source's position on the colour–colour diagram is determined by its Hα equivalent width and the shape of its continuum spectral energy distribution. The contrast scale in the right side indicates the number of emitters in each grid square. The expected locations of unreddened main sequence stars and the reddening track of an early A star are also shown. The unreddened main sequence track represents the upper bound of the main sequence locus, over which the Hα emitters were selected (Drew et al., 2005; Witham et al., 2006, 2008). The dashed lines show the constant Hα equivalent width (in Å) for early-type stars. These were taken from the literature (Drew et al., 2005; Witham et al., 2006, 2008), whereby they were calculated by computing power-law SEDs with $F_\lambda \propto \lambda^{-2.3}$ (for an optically thick accretion disc), adding Hα lines with the corresponding equivalent width (Witham et al., 2006), and then calculating the reddening tracks of the resulting model spectra. The solid vertical lines indicate increasing Hα emission for the model SED at fixed reddenings (specified across the top as $E(B-V)$).

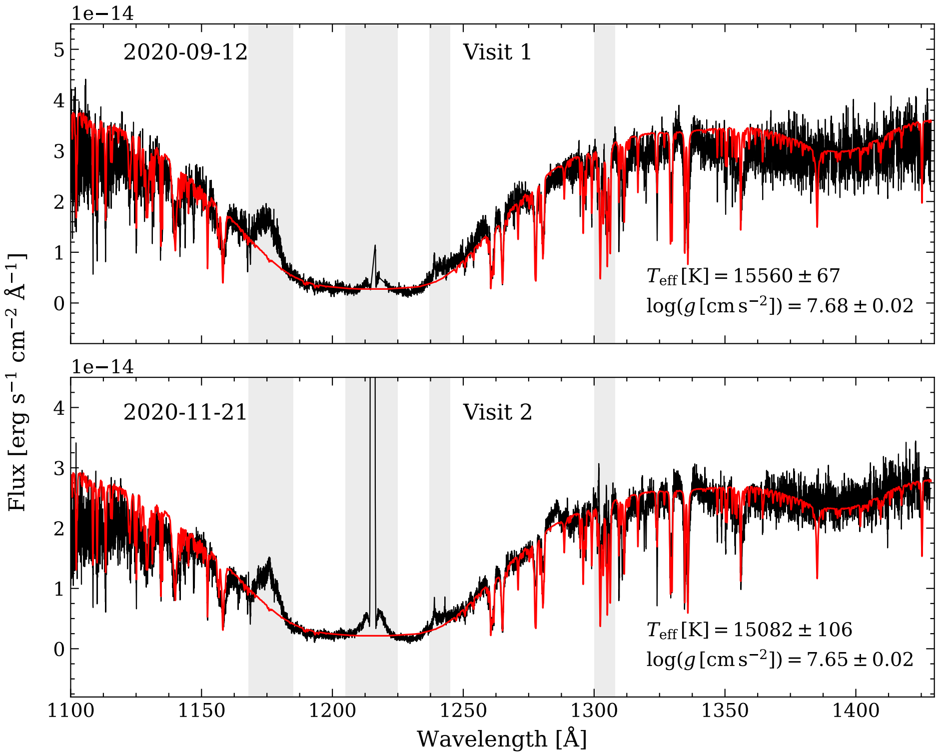

Figure 3.3: Average spectra of V3101 Cyg. The COS spectrum of individual visits are shown in black with the best-fit WD model atmosphere combined with a constant flux in red. The spectral regions masked during the fitting are shown in grey. The broad Lyman α absorption feature confirms the hydrogen dominant atmosphere of the white dwarf. The best-fit $T_{\rm eff}$ and $\log g$ with 1σ errors of individual visits are labeled in the figure, where the temperature difference between the two visits reflects the cool down of the white dwarf.

3.4 Metal Abundances

We observe strong absorption lines of several elements including C, O, and Si in the COS spectrum. To understand the chemical composition of the white dwarf in WD 0141–675, we measured photospheric abundances using COS sub-exposures of individual visits. Keeping the $T_{\rm eff}$, and $\log g$ fixed to the average of the two visits as obtained earlier, we generated a white dwarf model grid with abundances (defined as log(Z/H) where Z represents the element with respect to H) ranging from -10 to -3 in steps of 0.5 dex (Koester, 2010). Since it is difficult to constrain both $v \sin i$ and photospheric abundances at the same time, we fixed the $v \sin i$ to 47 km s^{-1} in the models. To derive the abundances log(Si/H), log(C/H), and log(O/H) from the models, we chose the spectral regions covering Si II (1260.42, 1264-1265 Å), Si III

Table 3.4: Element photospheric abundances derived from spectroscopic fit to COS spectra.

Element	log(Z/H)
C	-4.10 ± 0.10
Si	-5.10 ± 0.12
O	-3.41 ± 0.10
Fe	$< -5.57 \pm 0.32$
S	$< -4.77 \pm 0.40$

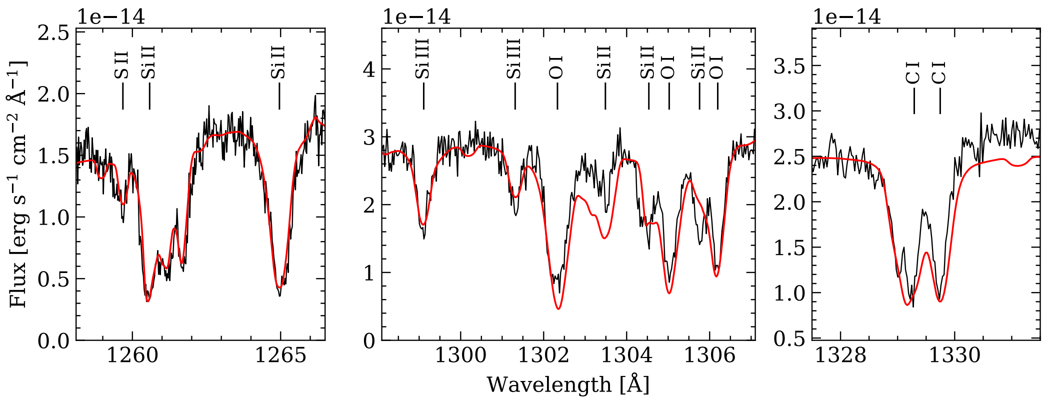

Figure 3.4: Elemental Abundances from COS spectra: COS spectra (Visit 1 for example) are shown in black while the white dwarf synthetic spectra for a hydrogen-dominant atmosphere corresponding to the best-fit abundances (Table 3.4) are shown in red. The strong absorption features of Si II, O I and C I are indicated by the solid black lines.

(1294-1301 Å), O I (1152.15 Å, 1302-1306 Å) and C I (triplet at 1329 Å) lines as shown in Figure 3.4. Varying log(Z/H) and line velocity, the models were fitted to these spectral regions following a standard χ^2 minimisation technique to find the best-fit abundances. Since Si II, and O I lines are contaminated by the absorption lines arising from the interstellar medium along the line of sight, we also included their contribution in the model fitting to accurately measure the abundances (Williams et al., 2025). Finally, we computed the abundances and their corresponding 1σ uncertainties considering the average and standard deviation of best-fit abundances obtained from individual sub-exposures, as provided in Table 3.4. We do not detect strong absorption lines of Fe II (weak lines between 1140-1152 Å) and S II (1250-1259 Å), hence, we determined an upper limit of log(Fe/H) = -5.6 and log(S/H) = -4.8 (Williams et al., 2025). Overall, we find that the abundance ratios of C/Si and O/Si are in agreement (within $\pm 2\sigma$) with that of the Sun (Lodders, 2003).

3.5 SED Fit to Catalogue Photometry

Table 3.5: Parameter Range and optimal values from SED fit.

Component	Parameter	Range	Optimal Value
White dwarf	$T_{\rm eff}$ [K]	3 000-70 000	$7\,250 \pm 200$
	$\log(g)$ $[cms^{-2}]$ *	–	7.5
	Z $[Z_\odot]$ *	–	0.5
Brown dwarf	$T_{\rm eff}$ [K]	1 000-3 600	$1\,300 \pm 100$
	$\log(g)$ $[cms^{-2}]$ *	–	5.0
	Z $[Z_\odot]$ *	–	0.0
Disc (H Slab)	$T_{\rm eff}$ [K]	4 500-9 500	$5\,500 \pm 50$
	Density	$10^4 - 5 \times 10^8$	10^7
	Gas Pressure	$50 - 1\,600$	50

*Fixed

We made a spectral energy distribution (SED) fit to the available archival photometry from before the outburst in 2019 (see Table 3.2), in order to measure the quiescent temperature of the system's components: white dwarf, brown dwarf and accretion disc. In Table 3.5, we list the optimal parameters of this model and the explored ranges.

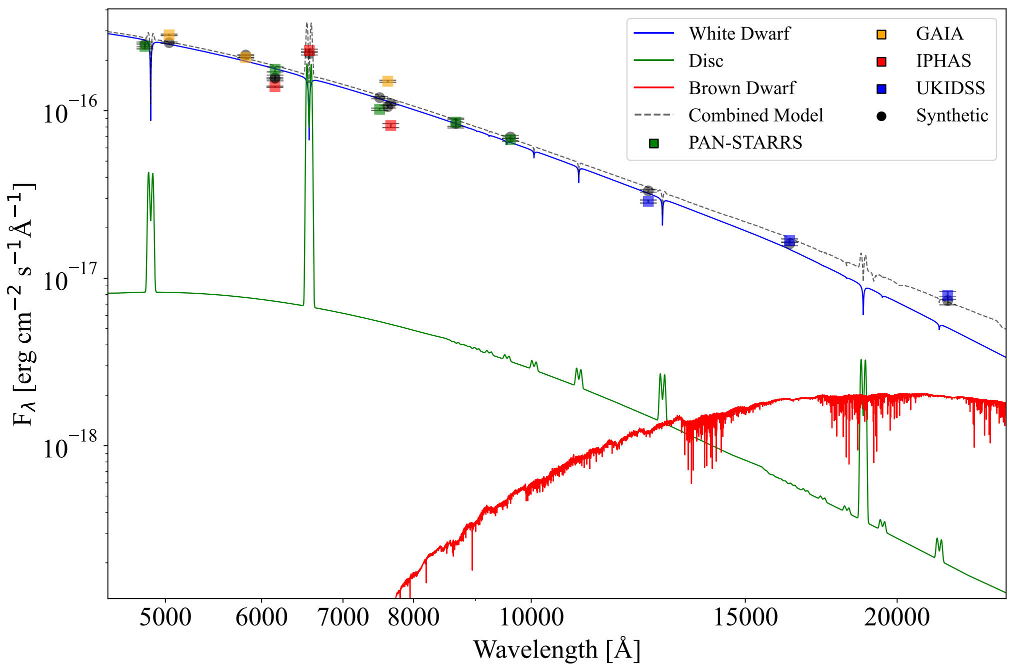

Figure 3.5: Spectral Energy Distribution of V3101 Cyg. Three components contribute to the flux of V3101 Cyg: the white dwarf (blue), accretion disc (green), and brown dwarf (red). The black dashed line represents the best-fit combined model. The observed photometry (colour-coded squares) corresponds to the long dormant state, taken before the 2019 outburst. The synthetic photometry is plotted as dark gray circles.

We computed a grid of white dwarf atmosphere models (Koester, 2010) covering the range of 3000-40000 K in steps of 250 K, assuming a metallicity of $Z = 0.5\,Z_\odot$ and $log(g) = 7.66$ (see White Dwarf Atmospheric Parameters). The models were scaled according to the equation:

$$S = \left(\frac{R_{\rm wd}}{d}\right)^2 \tag{3.1}$$

Where $R_{\rm wd} = 0.0153 \pm 0.0002\,R_\odot$ is the white dwarf radius, and $d = 108 \pm 0.7$ pc, is the distance from the system. The white dwarf radius was estimated iteratively: 1) for a first approximation, we used the spectroscopic measurements of $T_{\rm eff,wd}$ and log(g) (see Section 3.3), and the La Plata mass-radius relationship. This first iteration corresponds to the radius of a white dwarf puffed up due to the post-outburst temperature. 2) Next, we computed the SED fit (described below) using that radius for the scaling factor. 3) With the resulting white dwarf quiescent effective temperature ($T_{\rm eff,wd,q}$) and the spectroscopically measured mass, we again used the mass-radius relationship to obtain a new iteration of the radius. We repeated steps 3) and 4) until the white dwarf radius converged to the value above-mentioned.

We approximated the disc emission using an isothermal and isobaric pure-hydrogen slab model (e.g. Gänsicke et al., 1997, 1999). We assumed a tidal truncation limit to estimate the maximum disc radius (Neustroev & Zharikov, 2020):

$$R_{\rm max} = a(0.353 + 2.71{\rm e}^{-3.045\,q}) = 0.267 \pm 0.001\,R_{\odot} \tag{3.2}$$

Using the mass ratio estimate from the literature (q=0.0880(9), Tampo et al., 2020) and white dwarf mass obtained from our spectral fit, $M_{\rm wd} = 0.47 \pm 0.01\,{\rm M}_{\odot}$, we determined a donor mass of $M_{\rm d} = 0.041 \pm 0.001\,{\rm M}_{\odot}$. Thus the orbital period, $P_{\rm orb} = 77.01 \pm 0.02$ min and Kepler's third law yield an orbital separation $a = 0.48 \pm 0.01\,{\rm R}_{\odot}$. Assuming a Roche lobe filling donor star then returns a donor radius (Eggleton, 1983) :

$$R_{\rm d} = \frac{0.49\,a\,q^{2/3}}{0.6q^{2/3} + ln(1 + q^{1/3})} = 0.095 \pm 0.003\,{\rm R}_{\odot} \tag{3.3}$$

Combining $M_{\rm d}$ and $R_{\rm d}$ yields a surface gravity of the donor of $\log(g[cms^{-2}]) = 5.1 \pm 0.1$. The metallicity in the white dwarf photosphere represents a lower limit of that in the accretion stream incoming from the donor photosphere. However no model atmospheres are available for low-mass stars with $Z = 0.5\,Z_{\odot}$ and log(g)=5.1; instead we retrieved a grid of BT-DUSTY models for late-type stars from the Theoretical Spectra Web Server, with $Z = Z_{\odot}$ and $\log({\rm g}) = 5$. The temperature extended a range of 1000-3600 K in steps of 100 K.

We computed the synthetic photometry of our models accounting for the contribution of the three components and used a χ^2 minimisation routine to fit to the pre-outburst data. In particular, as shown in Fig. 3.5 and Supplementary Table 3.5, our best fit model returned a donor effective temperature of $T_{\rm eff,d} = 1\,300 \pm 100\,K$. It must be noted, however, that the lower limit of the temperature grid (1000 K) only covers relatively young brown-dwarf ages ($\simeq 3$ Gyr, Phillips et al., 2020). Therefore, for future work, it would be desirable to repeat the fit with a grid extending down to lower temperatures.

3.6 Radial Velocity Analysis of the White Dwarf

Making use of the TIME TAG mode, each of the observations were split in ∼8 min sub-exposures (see COS Spectroscopy in Observations and Data Reduction). We then

Table 3.6: Radial Velocity Parameters

White Dwarf Fit		
	Visit 1	Visit 2
γ (km s^{-1})	41.44±0.63	40.35±1.31
K_1 (km s^{-1})	21.36±0.87	23.85±1.86
MJD_0	59104.321±0.001	59174.242±0.001
P_{orb}* (days)	0.05352083	0.05352083
N V Lines		
	Visit 1	Visit 2
γ (km s^{-1})	42.66±5.96	38.67±3.33
K_1 (km s^{-1})	21.49±9.20	21.26±4.76
MJD_0	59104.327±0.003	59174.247±0.002
P_{orb}* (days)	0.05352083	0.05352083

*Fixed

repeated the fit from the preceding Section (White Dwarf Atmospheric Parameters) to each of the sub-exposures. The fit accounts for the Doppler-shift of the absorption lines, outputting the radial velocities of the white dwarf at the mid-time of each sub-exposure. The uncertainty estimate of each measurement included the instrumental systematic error of 8 km s^{-1} (Osterman et al., 2011, see also Section 2.1) Due to the long baseline, each of the visits were treated separately. We computed the Lomb-Scargle periodogram (Lomb, 1976; Scargle, 1982) for both visits as displayed in Fig. 3.6. The first visit displays a power signal at a period of $P_1 = 76.85 \pm 0.72$ min with a significance level over 99 percent (obtained from the False Alarm Probability). The second visit exhibits its strongest power signal at a period of $P_2 = 76.04 \pm 1.01$ min, also with a significance level well over 99 percent. We pre-whitened the signals consistent with the orbital period in search of other periodicities, but none appeared.

Our found periods are self consistent, and their average $P_{avg} = 76.44 \pm 0.62$ min, agrees within uncertainties with the value of $P_{orb} = 77.07 \pm 0.02$ min, obtained from the radial velocity analysis of the Hα emission line reported in the literature (Neustroev et al., 2019). Given that the latter value is better constrained by a smaller error, we adopt it as the orbital period of the white dwarf for the rest of our calculations.

Next we made an orbital fit of the radial velocities to a circular orbit (Eq. 2.2). The orbital period was fixed to $P_{orb} = 77.07 \pm 0.02$ min in Eq. 2.2, and therefore only the other three parameters were left free.

The optimal fit for each of the visits are shown in Figure 3.7. The optimal parameters of both visits are listed in Table 3.6. We note that the amplitude,

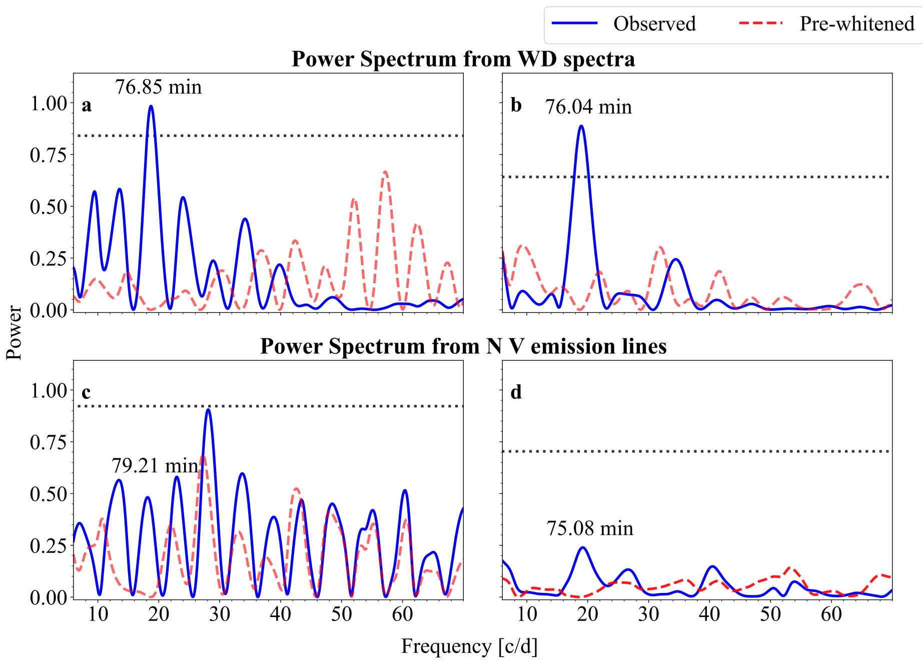

Figure 3.6: Lomb-Scargle periodograms of the radial velocities. The measured radial velocities (in blue) obtained from the white dwarf fit of the first (a) and second visit (b) show a clear peak at a period consistent with the expected orbital period. The N V periodograms (c and d for the first and second visit, respectively) do not show any significant signal. The periodograms re-computed after pre-whitening the orbital period ~77 min (in dashed red) do not show any signal exceeding the 99 percent significance threshold (horizontal dotted black line).

K_1, and the systemic velocity, γ, agree within the uncertainties for both visits, we therefore adopt the average from both visits as the white dwarf parameters: $K_{\rm wd} = 22.61 \pm 1.03\,{\rm km\,s^{-1}}$and $\gamma_{\rm wd} = 40.89 \pm 0.73\,{\rm km\,s^{-1}}$.

3.6.1 Orbital Inclination

Adopting the orbital period of $P_{\rm orb} = 77.07 \pm 0.02\,{\rm min}$ (Neustroev et al., 2019) and the average amplitude from both visits of $K_{\rm wd} = 22.60 \pm 1.06\,{\rm kms^{-1}}$, as the orbital velocity of the white dwarf (see Section 3.6), results in a mass function of the donor of:

$$f(M_{\rm d}) = \frac{P_{\rm orb} K_{\rm wd}^3}{2\pi G} = \frac{(M_{\rm d} \sin i)^3}{(M_{\rm wd} + M_{\rm d})^2} = 0.00006\,M_\odot \tag{3.4}$$

Where $M_{\rm wd}$ is the mass of the white dwarf, $M_{\rm d}$ is the mass of the donor and i is the orbital inclination of the system. We solved Eq. 4.1 for the inclination i, fixing $M_{\rm wd,cos,avg} = 0.47 \pm 0.01\,M_\odot$ (see Section 3.3).

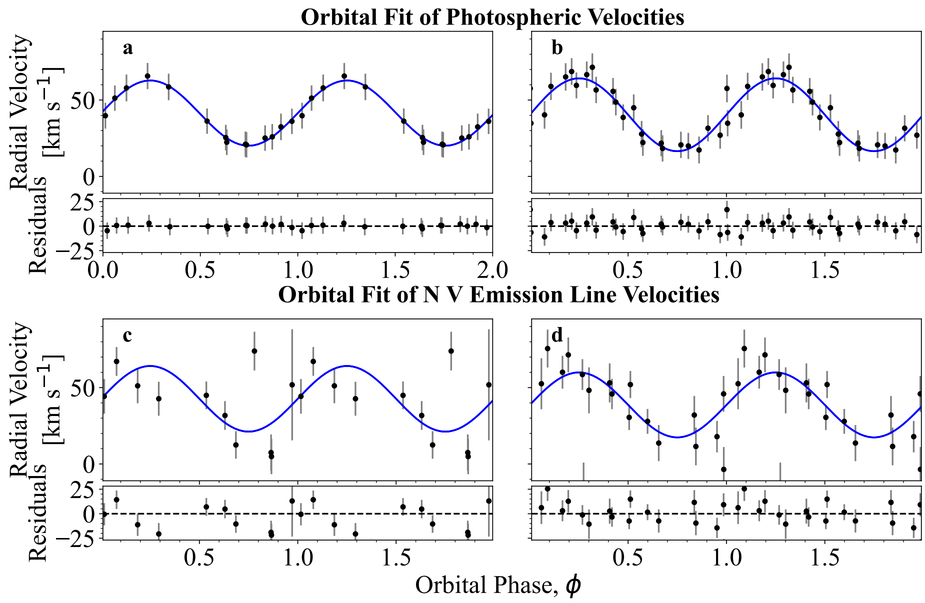

Figure 3.7: Orbital Fit of the radial velocities obtained from the best fit to white dwarf for the first (a) and second (b) visit show a clear sinusoidal behaviour when folded by the ≈77 min period. Those obtained from the N V emission show more scatter (c and d for the first and second visit, respectively), but folding by ≈77 min period yields consistent orbital parameters with those of the white dwarf. The error bars include the systematic uncertainty from the wavelength solution of the COS instrument. The data were repeated for a second orbital cycle for visualisation purposes.

We used different mass ratio values calculated from $\epsilon - q$ relations of different superhump stages (Kato & Osaki, 2013; McAllister et al., 2019). The values range from 0.1 (Neustroev et al., 2019) down to 0.062 (Patterson et al., 2005; Tampo et al., 2020), constraining the inclination within the range of $33° - 60°$ (Fig. 3.8). We note that even the highest reported value of $q \sim 0.1$ (Neustroev et al., 2019) results in a companion mass of $\sim 0.047\,M_{\odot}$, well below the hydrogen burning limit. However, that estimate was calculated for the stage A superhump period of V3101 Cyg using a relation calibrated with stage B periods (Patterson et al., 2005; Neustroev et al., 2019; Tampo et al., 2020, see also Eq. 1.15). On the other hand, the second highest reported estimate of q=0.0880(9) (Tampo et al., 2020) is arguably the least affected by instabilities of the available superhump periods (Kato & Osaki, 2013; Tampo et al., 2020). All other combinations of superhump periods (Tampo et al., 2020) and $\epsilon - q$ relations (McAllister et al., 2019) yield smaller values of the mass

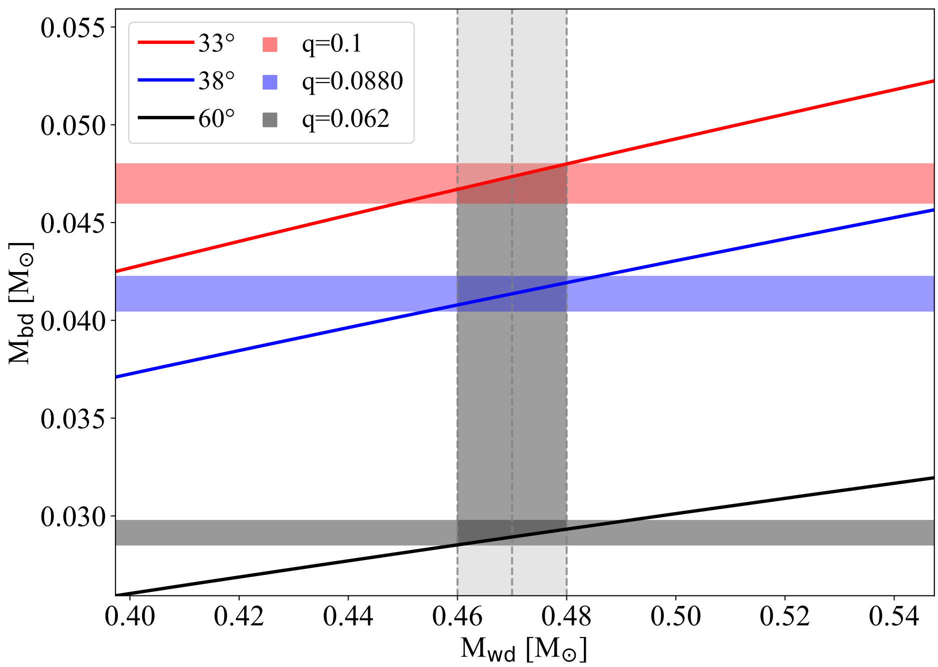

Figure 3.8: Inclination constraint from the mass function. Solving the mass function – assuming the measured white dwarf mass of $0.47 \pm 0.01\,\mathrm{M}_{\odot}$ (gray region) and the range of mass ratio values reported in the literature – constrains the inclination range between 33° for $q = 0.1$ (red), and 60° for $q = 0.062$ (black). Our selected mass ratio q=0.0880(9) (blue) results in an inclination of $38 \pm 1°$. The dark gray shaded region shows the mass parameter space allowed by the inclination and mass constraints.

ratio that imply smaller donor masses; therefore, we select q=0.0880(9) (Tampo et al., 2020) as our most conservative choice. We also note that combining the stage C relation (Eq. 1.17, McAllister et al., 2019) and the late stage superhump periods measured by Tampo et al. (2020) resulted in negative mass ratio values. This reinforces the argument by Kato et al. (2009), that late stages and stage C superhumps are distinctly different and should not be treated as equivalent.

It is worth highlighting that this mass ratio constraint is based upon indirect measurements obtained from superhump period excess. Therefore, we stress the importance of infrared observations to directly measure the mass of the donor star (e.g. Harrison, 2016; Neustroev & Mäntynen, 2023).

3.7 Radial Velocity of the N V Emission Lines

As shown in Figure 3.3, the N V doublet (λ1239 Å and λ1243 Å) is present in emission in the spectra. These same features were detected in strong absorption in the prototype cataclysmic variable U Geminorum, presumably originated in a region close to the white dwarf surface (Long & Gilliland, 1999). To verify this assesment, we performed a radial velocity analysis of these lines, by fitting a double Gaussian profile with a fixed separation and repeated the methodology described in the previous section (Radial Velocity Analysis of the White Dwarf) .

Among the weak signals in the Lomb-Scargle periodogram of the first visit, ≈79 min is present, although not dominant. The periodogram of the second visit shows a weak and broad peak at ≈75 min. None of these signals are statistically significant, likely due to the low signal-to-noise ratio of the N V emission; nonetheless the average of both visits, ≈77 min, agrees with the white dwarf orbital period (77.07 ± 0.02, Neustroev et al., 2019).

The orbital fit (Figure 3.7), fixing the period to that of the white dwarf, shows a clear oscillation with fitted parameters that agree remarkably well to those obtained for the white dwarf (see Table 3.6). This is highly suggestive that the N V doublet indeed originates in a region close to the white dwarf's surface and follow its orbital motion. This implies the presence of optically thin material in the line of sight that co-orbits with the white dwarf. The accretion disc would be a candidate but our estimated low inclination would require it to be highly flared. It is possible that the white dwarf was observed with a puffed up white dwarf atmosphere (Crumpler et al., 2024), however we leave this problem for consideration of the reader.

3.8 COS Lightcurve Extraction

The *HST* COS TIME-TAG data collection mode allows us to extract a lightcurve from the spectroscopic observations (see Section 2.1.1). This was performed with the LIGHTCURVE Python package (Ely et al., 2015), implementing five-second bins and masking the geocoronal emission lines from Ly α (≈ 1216 Å) and O I (≈ 1300 Å). The lightcurve for both visits can be observed in Figure 3.9. We performed a Lomb-Scargle periodogram (see Fig. 3.10), that shows a complex structure. However, the same power structure is reproduced upon obtaining the Lomb-Scargle of an interpolated sine wave function modulated by the true orbital period. In the case of the first visit, the periodograms practically overlap. From this we can conclude that the only periodic motion corresponds to the orbital modulation. For the

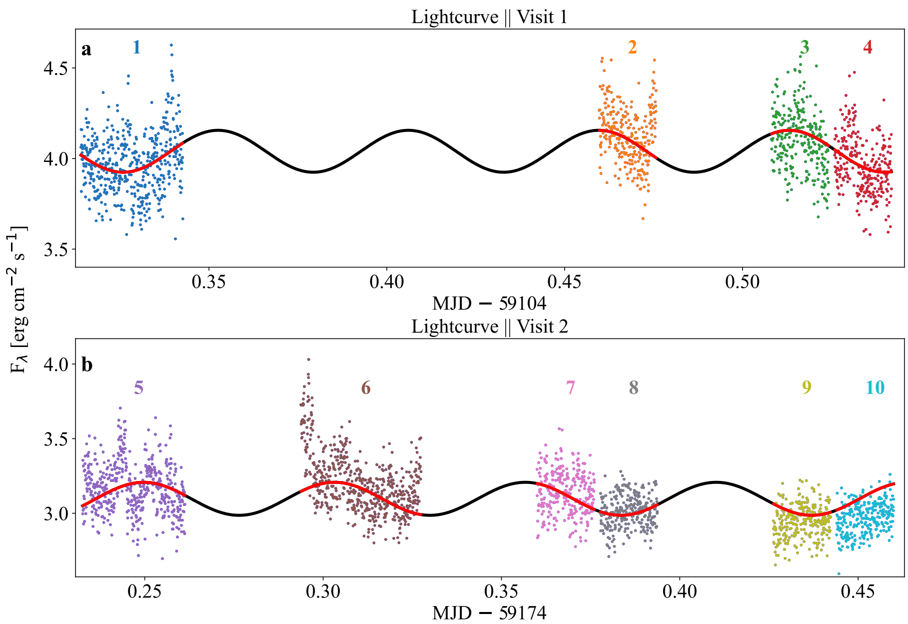

Figure 3.9: Far Ultraviolet Lightcurve of V3101 Cyg, computed from the *HST* COS observations taken on TIME-TAG mode. Overall the lightcurve shows a weak sinusoidal modulation consistent with the orbital period (black). Each observation is numbered as in Table 3.1 and plotted in different colors for visual aid. Note that the scale of the time axis is different for each visit. It can be observed that the flux decreased for the second visit, as expected from the progressive cooling of the white dwarf.

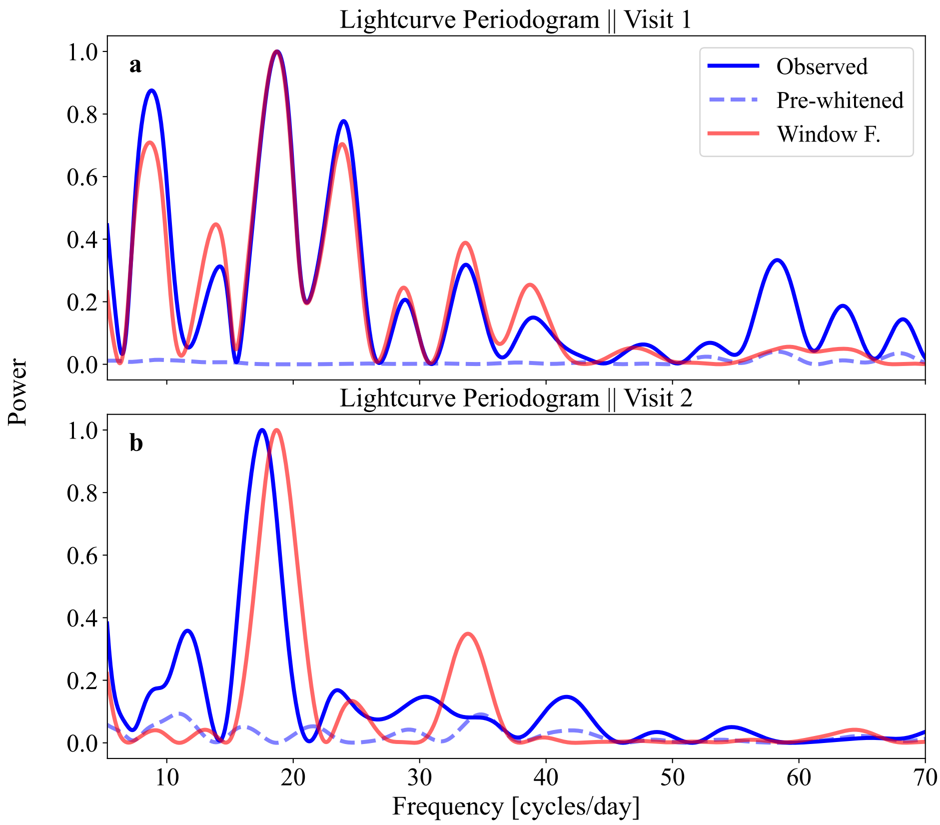

Figure 3.10: The lightcurve periodogram (solid blue) shows a complex structure, which overlaps with the periodogram of an interpolated sine wave (solid red) having the true orbital period (77.07±0.02 min). The periodogram of the prewhitened lightcurve (dashed blue), after subtracting a signal corresponding to the orbital period (77 min), shows no additional signals.

second visit, the main peak appears shifted by ≈1 c/d. This can be explained by an additional source of non-periodic flickering particularly present in observations 5 and 6 (as numbered in Fig. 3.9).

Pre-whitening the orbital signal from the observed lightcurve, and repeating the Lomb-Scargle, shows no signals remain present. This corroborates that the orbital period is the only periodical signal present in the lightcurve data.

The overall well-behaved curve discards the presence of periodic variability aside from the orbital motion, such as white dwarf pulsations (Toloza et al., 2016); double humps from accretion driven by spiral shocks (Pala et al., 2019); or hot spots on the white dwarf. Such phenomena could cause an overestimation of the white dwarf temperature, affecting the mass measurements. Their absence is an indication that the white dwarf parameter values obtained in the spectral fit (see White Dwarf Atmospheric Parameters Section and Supplementary Table 3.3) are accurate estimates.

3.9 Discussion

3.9.1 Evolutionary Channels with MESA

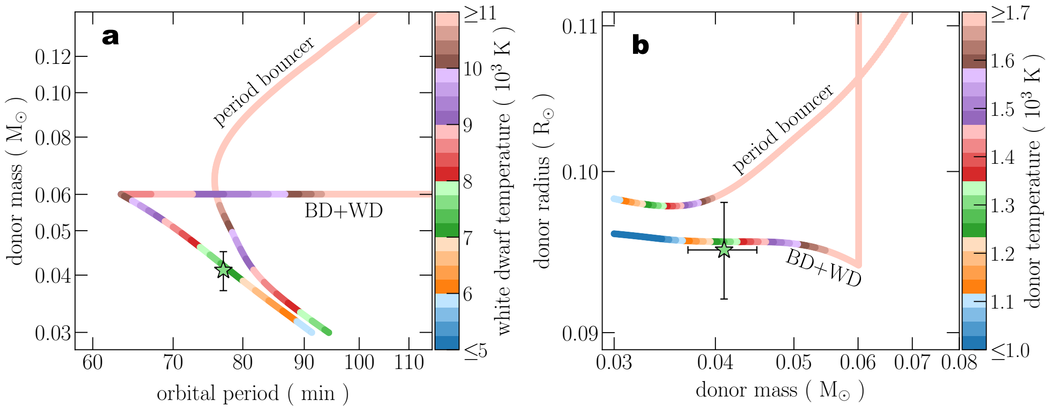

Figure 3.11: Comparison between observed and predicted properties with MESA. Evolution of the donor star mass and white dwarf effective temperature with the orbital period (**a**). Evolution of the donor star effective temperature with the donor star radius-mass relation (**b**). At the observed orbital period, the period bouncer channel predicts a donor brown dwarf that is more massive, hotter, and larger than observed as well as a white dwarf that is hotter and larger than observed. On the other hand, all properties predicted by the brown dwarf+white dwarf channel are in excellent agreement with the observed.

Given the parameters of V3101 Cyg, it could be either a period bouncer (i.e. descendant of a cataclysmic variable with a main-sequence donor star that eventually transitioned to a brown dwarf) or a descendant of a detached white dwarf plus brown dwarf binary (i.e. the donor star is already a brown dwarf at the onset of mass transfer). We therefore tested both formation pathways and searched for reasonable models that can explain the observed properties of V3101 Cyg. After finding the region in the parameter space leading to properties comparable to the observed, if needed, we refined the grid in such a region to search for the best-fitting values.

We used version r15140 of the Modules for Experiments in Stellar Astrophysics (MESA) code (Paxton et al., 2011, 2013, 2015, 2018, 2019; Jermyn et al., 2023) to calculate binary evolution from the moment just after common-envelope evolution onwards. The MESA equation of state is a blend of the OPAL (Rogers & Nayfonov, 2002), SCVH (Saumon et al., 1995), PTEH (Pols et al., 1995), HELM (Timmes & Swesty, 2000), PC (Potekhin & Chabrier, 2010), and Skye (Jermyn et al., 2021) equations of state. Nuclear reaction rates are a combination of rates from NACRE (Angulo et al., 1999), JINA REACLIB (Cyburt et al., 2010), plus additional tabulated weak reaction rates (Fuller et al., 1985; Oda et al., 1994; Langanke & Martínez-Pinedo, 2000). Screening is included (Chugunov et al., 2007) as well as thermal neutrino loss (Itoh et al., 1996) and electron conduction opacities (Cassisi et al., 2007). Radiative opacities are primarily from OPAL (Iglesias & Rogers, 1993, 1996) and, for low temperatures, we adopted the two available opacity tables (Ferguson et al., 2005; Freedman et al., 2008, 2014), which cover sufficiently low temperatures (down to ~ 1000 K). The Roche lobe radius is computed using Eggleton's fit (Eggleton, 1983) and the mass transfer rates are determined assuming the atmospheric Roche-lobe overflow model (Ritter, 1988).

We adopted two values for the metallicity $Z = 0.02, 0.01$, which are consistent with the location of V3101 Cyg in the Milky Way, i.e. in the solar neighbourhood. We adopted several schemes to calculate the outer boundary conditions of the atmosphere (Paxton et al., 2011): the grey Eddington T(tau) relation using either a uniform opacity that is iterated to be consistent with the final surface temperature and pressure at the base of the atmosphere or a varying opacity consistent with the local temperature and pressure throughout the atmosphere as well as non-grey model atmosphere tables, which determine the surface temperature and pressure at the surface optical depth of either 100 or 10.

We included orbital angular momentum loss due to gravitational radiation ($\dot{J}_{\rm GR}$), following the standard prescription of emission of gravitational waves. We also allowed the binary to lose additional angular momentum during the evolution, either with consequential angular momentum loss and/or residual magnetic braking. We adopted the following schemes for the extra angular momentum loss (i.e. in addition to gravitational radiation): (i) no extra angular momentum loss, i.e. $\dot{J}_{\rm orb} = \dot{J}_{\rm GR}$; (ii) adopting the empirical consequential angular momentum loss model (Schreiber et al., 2016), i.e. $\dot{J}_{\rm CAML} = \nu\,(M_{\rm wd}/{\rm M_\odot})^{-1}$, where $M_{\rm wd}$ is the white dwarf mass and ν varies from 0.20 to 0.40, in steps of 0.05. So, $\dot{J}_{\rm orb} = \dot{J}_{\rm GR} + \dot{J}_{\rm CAML}$; (iii) adopting a residual magnetic braking (Knigge et al., 2011) in the form $\dot{J}_{\rm res} = \eta\,\dot{J}_{\rm GR}$, where $\eta = 0.5, 1.0, 1.5, 2.0, 2.5$. So, $\dot{J}_{\rm orb} = \dot{J}_{\rm GR} + \dot{J}_{\rm res}$; (iv) adopting a combination of empirical consequential angular momentum loss and residual magnetic braking. So, $\dot{J}_{\rm orb} = \dot{J}_{\rm GR} + \dot{J}_{\rm CAML} + \dot{J}_{\rm res}$.

We assumed that the white dwarf experiences nova eruptions, resulting in the ejection of all the accreted mass from the companion. This implies that the white dwarf mass just after common-envelope evolution is 0.47 $\rm M_\odot$, which is exactly the measured mass. We computed the white dwarf properties (e.g. effective temperature and radius) with a linear interpolating/extrapolation scheme, using the La Plata tracks (Althaus et al., 2013; Camisassa et al., 2016, 2017, 2019). To estimate the white dwarf accretion luminosity, we adopted the compressional heating model (Townsley & Gänsicke, 2009), that is,

$$\frac{L_{\rm wd}}{\rm L_\odot} = 0.006 \left(\frac{\langle \dot{M} \rangle}{10^{-10}\,{\rm M_\odot\,yr^{-1}}} \right) \left(\frac{M_{\rm wd}}{0.9\,{\rm M_\odot}} \right)^{0.4} \tag{3.5}$$

where $L_{\rm wd}$ is the white dwarf luminosity and $\langle \dot{M} \rangle$ is the mass transfer rate. With the white dwarf luminosity and white dwarf mass, we can easily obtain the other properties from the tracks.

In the period bouncer scenario, as the mass transfer would most likely become dynamically unstable for a cataclysmic variable hosting initially a main-sequence having a radiative core, given the low mass of the white dwarf (Schreiber et al., 2016), we only considered systems with fully convective main-sequence donors at the onset of mass transfer (i.e. with donor stars having initially masses ≤ 0.3 $\rm M_\odot$). For the mass of the companion of the white dwarf just after common-envelope evolution, we assumed 0.2 $\rm M_\odot$. Although we did not adopt other masses, the evolutionary sequences would all converge to the same track because of the dependence on the angular momentum loss recipes we adopted. The initial orbital period is assumed to be 0.1 d. We did not take into account pre-common-envelope evolution or different orbital periods because the investigated donor masses are too low, with evolutionary timescales much longer than the Milky Way age. Finally, we also considered in the fitting scheme as a constraint the orbital period minimum ($75 - 85$ min), which is one of the strongest observational constraints on cataclysmic variables (Gänsicke et al., 2009; McAllister et al., 2019).

For the scenario where the progenitor is a detached white dwarf plus brown dwarf binary, we need to first create brown dwarf models. We created brown dwarfs and stopped the evolution when they were still hot, having an age of only 1 Myr. For the mass of the brown dwarfs just after common-envelope evolution, we assumed 0.06 $M_{\odot}$. This choice does not affect our results because we would have achieved fits of the same quality for other masses, provided the orbital period just after common-envelope evolution and the angular momentum loss rates are adjusted. We set the orbital period just after common-envelope evolution to values from 0.08 to 0.14 d, in steps of 0.01 d. As the brown dwarf cools and shrinks with time, we had to select different initial post-common-envelope orbital periods so that the onset of mass transfer occurs at different brown dwarf ages, i.e. for different effective temperatures and radii.

In both channels, we stop the evolution when one of the following conditions is satisfied: (i) the mass transfer rate gets higher than 10^{-4} $M_{\odot}\,yr^{-1}$, so that the mass transfer is considered dynamically unstable; (ii) the mass of the donor star drops to 0.03 $M_{\odot}$. This allows us to cover the range of the measured orbital period (~ 77 min) and donor mass (~ 0.04 $M_{\odot}$).

The parameters of the best-fitting models for each channel are provided in Table 3.7. Assuming V3101 Cyg is a period bouncer, the angular momentum loss rate required to reproduce the orbital period minimum vary from $\approx -2 \times 10^{34}$ dyn cm (close the onset of mass transfer) to $\approx -7.5 \times 10^{33}$ dyn cm (at the orbital period minimum). These rates lead to an orbital period minimum of ≈ 76 min (consistent with the observed orbital period minimum) and correspond roughly to the minimum allowed to reproduce the observed orbital period, as otherwise the period minimum would be longer than the observed orbital period. At the observed orbital period, the rate is $\approx -5.5 \times 10^{33}$ dyn cm, which is about five times higher than required to explain the white dwarf effective temperature. For this reason, the white dwarf effective temperature and the white dwarf radius cannot be explained as the predicted values are much greater than the observed. Such a high rate also implies that the brown dwarf mass, its effective temperature, and its radius are much greater than observed. This happens because the brown dwarf properties at the transition from a main-sequence star to a brown dwarf are entirely constrained by the angular momentum loss rates, which means there is no way to control the effective temperature when it becomes a brown dwarf.

On the other hand, assuming V3101 Cyg is a descendant of a detached brown dwarf+white dwarf binary, all observed parameters can be reasonably well explained, for an angular momentum loss rate of $\approx -1.2 \times 10^{33}$ dyn cm at the observed orbital period, which are the required to explain the white dwarf effective temperature and its radius. The success of this channel can be attributed to the onset of mass transfer occurring with a brown dwarf companion, which can occur when the brown dwarf effective temperature is low enough and its radius is correspondingly small.

Therefore, given the failure of the period bouncer channel in reproducing the properties we derived and the excellent agreement between prediction and observation with the detached brown dwarf+white dwarf binary channel, we can conclude that V3101 Cyg is most likely a descendant of a detached brown dwarf+white dwarf binary. Our results also imply that the angular momentum loss mechanisms boosting the evolution of period bouncers are not acting with similar efficiency in cataclysmic variables that are descendants of detached brown dwarf binary+white dwarf binaries.

Table 3.7: Parameters derived from the data and predicted with the best-fitting model assuming V3101 Cyg is either a period bouncer or a descendant of a detached white dwarf plus brown dwarf binary.

parameter	observed	predicted	
		period bouncer	brown dwarf + white dwarf
orbital period (min)	77.07 ± 0.02	77.05	77.07
white dwarf mass ($M_\odot$)	0.47 ± 0.01	0.47	0.47
white dwarf quiescent $T_{\rm eff}$ (K)	7500 ± 200	10 535	7 431
white dwarf radius ($R_\odot$)	0.0153 ± 0.0002	0.0160	0.0155
brown dwarf mass ($M_\odot$)	0.041 ± 0.004	0.0544	0.0420
brown dwarf quiescent $T_{\rm eff}$ (K)	1300 ± 100	2 235	1 329
brown dwarf radius ($R_\odot$)	0.095 ± 0.003	0.1039	0.0955

3.10 Summary and Conclusions

In this chapter we analysed the far ultraviolet observations of V3101 Cyg, obtained with the *HST* COS spectrograph. We fitted the spectra and determined a white dwarf mass of $M_{\rm wd} = 0.47 \pm 0.01\,{\rm M}_\odot$(see Table 3.3). The mass ratio $q = M_{\rm d}/M_{\rm wd}$, determined from the well-calibrated relation between the orbital period and the superhump period arising from the precession of the accretion disc during the outburst (Patterson et al., 2005; Kato & Osaki, 2013) ranges from $q = 0.088$ (Tampo et al., 2020) to $q = 0.1$ (Neustroev et al., 2019). The mass of the donor in V3101 Cyg is therefore between $M_{\rm d} = 0.041 \pm 0.001\,{\rm M}_{\odot}$ and $0.047 \pm 0.001\,{\rm M}_{\odot}$, well below the hydrogen burning limit.

Furthermore, the COS spectrum contains emission from the N V 1240 Å resonance doublet. It shows a clear two-component structure, with a broad base and sharp emission spikes. Similar sharp emission lines from hot plasma very near the white dwarf have been detected in a number of binaries (Long & Gilliland, 1999; Tappert et al., 2011). We measured a radial velocity amplitude of $21.31 \pm 4.23\,{\rm km\,s^{-1}}$ from the sharp N V lines, which we interpret as the motion of the white dwarf (see Section 3.7).

Besides the low mass of both its stellar components V3101 Cyg stands out as having one of the most extreme dwarf nova outbursts observed, with an extremely large amplitude and followed by a mix of both normal and super-oubursts. It is also likely to have one of the longest outburst recurrence times, suggesting a low mass transfer rate from the donor.

The quiescent temperature of white dwarfs in cataclysmic variables provide a good estimate of the long-term average of the accretion rate (Townsley & Gänsicke, 2009). Fitting the quiescent spectral energy distribution assembled from photometry obtained before the 2019 outburst with a three-component model (white dwarf, accretion disc, and brown dwarf, see Section 3.5) results in $T_{\rm eff,wd} = 7\,500 \pm 200\,{\rm K}$ for the white dwarf, $T_{\rm eff,disc} = 5\,500 \pm 50\,{\rm K}$ for the accretion disc, and $T_{\rm eff,d} = 1\,300 \pm 100\,{\rm K}$ for the donor. The average accretion rate determined from the quiescent white dwarf temperature and its mass (Townsley & Gänsicke, 2009) is $\log \left\langle \dot{M} \right\rangle = -10.81 \pm 0.05\,{\rm M_{\odot} yr^{-1}}$, which is at the extreme lower end of the cataclysmic variable population (Pala et al., 2022). The low accretion rate is corroborated by the unusually low temperature of the accretion disc (Williams, 1980).

Given our measurement of $M_{\rm d}$, we conclude that the donor is a brown dwarf. Whereas a small number of cataclysmic variables with similarly low-mass donors are known (Beuermann et al., 2020; Pala et al., 2022), V3101 Cyg is the only system with a low-mass white dwarf and brown-dwarf donor. We explored the evolutionary history resulting in this cataclysmic variable with rather unusual properties using numerical simulations with MESA (Paxton et al., 2019; Jermyn et al., 2023) of two different progenitor channels (see Section 3.9.1): (1) A cataclysmic variable formed with a main-sequence donor that evolves into a brown dwarf upon reaching the period minimum; and (2) A detached white dwarf plus brown dwarf pair that initially evolves to periods below the period minimum before starting mass transfer and evolving back towards longer periods. These simulations unambiguously favour the white dwarf plus brown dwarf genesis, which reproduces the system's current parameters (Fig. 3.11, Table 3.7). By contrast, a cataclysmic variable with a main-sequence donor evolving into a brown dwarf fails to match the low temperatures of both the donor and the white dwarf (and consequently the low mass-transfer rate) at the observed orbital period, and it also cannot reproduce the donor's low mass and radius.

V3101 Cyg, with an unusually low-mass white dwarf harbouring a cool substellar donor, and low mass-transfer rate, is the best candidate of a cataclysmic variable born with a brown-dwarf donor. Taking the 42 cataclysmic variables known within 150 pc (Pala et al., 2020) as representative sample suggests that this evolution channel only contributes a few per cent to the total population, much lower than predicted by the theoretical models (Politano, 2004).

Chapter 4

WD 0141-675: a tentative radial velocity signal detection

"Science does not rest upon solid bedrock. The bold structure of its theories rises, as it were, above a swamp."

Karl Popper

4.1 Introduction

WD 0141–675 is a nearby ($d = 9.71$ pc, Gaia Collaboration et al. (2023b)) white dwarf with a hydrogen-dominated atmosphere (Hintzen & Jensen, 1979), with weak Ca H&K absorption lines (Debes & Kilic, 2010), indicating ongoing accretion of planetary material. Interest in WD 0141–675 was recently sparked when an astrometric planet candidate with an orbital period of $P = 33.65 \pm 0.05$ d and a mass of $M_\mathrm{c} = 9.26^{+2.64}_{-1.15}\,\mathrm{M_{Jup}}$ was announced (Gaia Collaboration et al., 2023a; Holl et al., 2023). However in 2023 May, the planet candidate was quietly retracted via a news item[1], and classified as a false positive in the *Gaia* astrometric solutions.

Rogers et al. (2024a) presented a prescription for investigating the nature of astrometric candidate planets using WD 0141–675 as a case study. These authors stress the importance of follow-up spectroscopic observations to confirm a planetary companion. With this in mind, we obtained high-resolution spectroscopy of WD 0141–675 using ESPRESSO (Echelle SPectrograph for Rocky Exoplanets and

[1] https://www.cosmos.esa.int/web/gaia/dr3-known-issues

Stable Spectroscopic Observations) on the Very Large Telescope (VLT), to probe for radial velocity variations indicative of a planetary companion. ESPRESSO is an optimal spectrograph for such objective, as was made evident by Pasquini et al. (2023), who reported highly-accurate velocity shifts of eight Hyades white dwarfs using this instrument, showcasing its capabilities.

4.2 Observations

We acquired high-resolution spectroscopy of WD 0141–675 with the ESPRESSO spectrograph at the VLT of the European Southern Observatory (ESO). We used the single-telescope configuration, slow read-out and 4×2 binning (spatial×spectral). We obtained a total of 20 spectra, each with an exposure time of 3144 s, throughout the period 2023 October 10 to 2023 December 20; further details of the observations are provided in Table 4.1. The observations were designed to sample the putative orbital period of $P_{\rm orb} = 33.65 \pm 0.05$ d, obtaining one spectrum on average once every two days. However, due to varying sky conditions, several nights were skipped, and the observations ended up being spread out over two months.

The ESPRESSO data were reduced with the Data Reduction Software[2] (DRS) version 3.0.0. The DRS performs standard echelle spectrum reduction, including bias and dark subtraction, optimal order extraction, bad pixel correction, flat-fielding, deblazing, wavelength calibration, and order merging (for details see Pepe et al., 2021). Here we used the deblazed, order-merged spectra. We removed telluric lines using MOLECFIT (Kausch et al., 2015; Smette et al., 2015). The signal-to-noise ratio (S/N) of the individual spectra, measured around the Ca K absorption line, ranges from 14 to 25 (Table 4.1).

4.3 Results

4.3.1 Atmospheric Analysis

We used the atmosphere code of Koester (2010) to model the Ca K line in the ESPRESSO spectra of WD 0141−675. Because ESPRESSO is designed primarily for high-precision velocity measurements, the flux calibration is not sufficiently accurate over wavelength scales comparable to the width of the Balmer lines to attempt a spectroscopic fit of the atmospheric parameters, i.e. the white dwarf effective temperature, $T_{\rm eff}$, and its surface gravity, $\log g$. We therefore adopted the values from Rogers et al. (2024a), who derived spectroscopic and photometric parameters of

[2] www.eso.org/sci/software/pipelines/espresso/espresso-pipe-recipes.html

Table 4.1: Log of the ESPRESSO spectroscopy, with the date referring to the start of the exposure. Each spectrum was taken with a 3144 s exposure time. The lunar distance refers to the angular separation from the moon in degrees.

Date	Time	MJD	Lunar Dist.	FLI	S/N
2023-10-20	03:13:49	60237.134604	74	0.3	20.9
2023-10-21	02:16:07	60238.094533	69	0.4	21.5
2023-10-25	06:03:14	60242.252246	64	0.8	20.1
2023-10-29	02:32:04	60246.105605	84	1.0	20.3
2023-11-05	03:57:32	60253.164957	118	0.5	20.2
2023-11-11	01:32:23	60259.064163	105	0.1	19.9
2023-11-13	01:54:27	60261.079487	94	0.0	17.5
2023-11-14	01:52:00	60262.077783	88	0.0	14.2
2023-11-19	01:41:56	60267.070795	63	0.3	14.1
2023-11-26	00:39:32	60274.027459	87	1.0	25.8
2023-12-05	00:30:18	60283.021052	117	0.5	22.2
2023-12-06	00:46:26	60284.032248	115	0.4	18.1
2023-12-07	01:55:34	60285.080263	111	0.3	19.5
2023-12-08	00:52:07	60286.036197	107	0.2	16.3
2023-12-09	01:47:59	60287.074998	102	0.2	12.0
2023-12-10	03:21:44	60288.140102	96	0.1	13.9
2023-12-11	03:30:44	60289.146346	89	0.0	19.3
2023-12-12	01:11:57	60290.049968	84	0.0	16.8
2023-12-16	01:28:59	60294.061797	64	0.1	18.0
2023-12-20	02:23:25	60298.099596	69	0.5	19.0

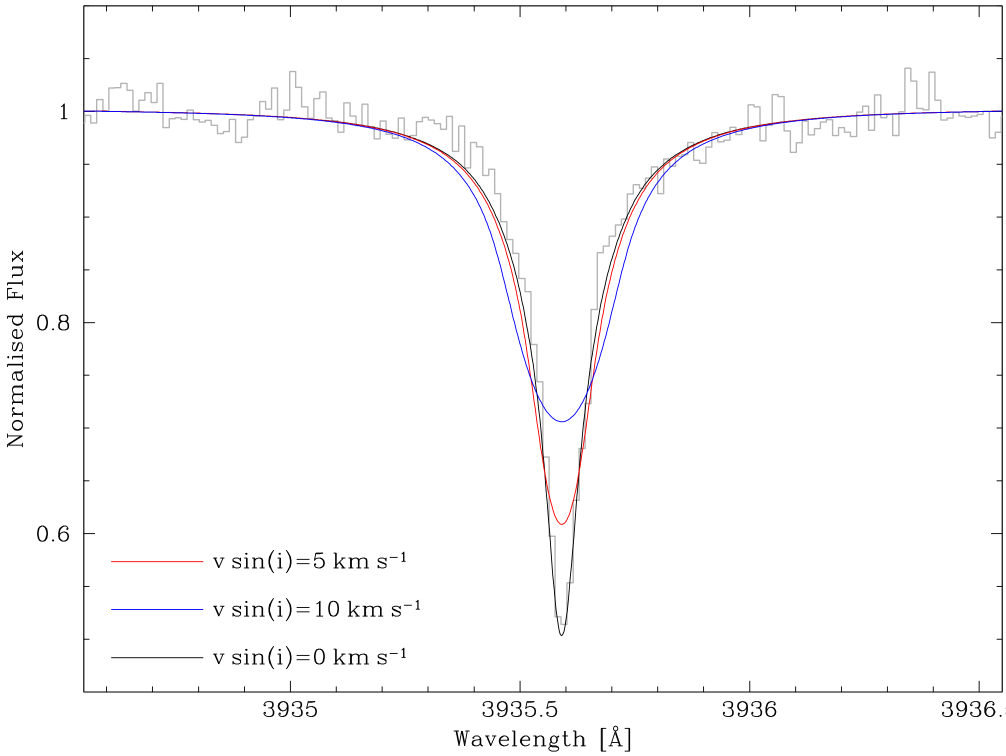

Figure 4.1: The Ca K absorption in the ESPRESSO spectrum of WD 0141−675 (gray) is well modelled by a non-rotating white dwarf with $T_{\rm eff} = 6321$ K, $\log g = 7.97$ and $\log({\rm Ca/H}) = -10.85$ (black line). The red (blue) lines show the model broadened by a rotational velocity of $v\sin(i) = 5\,{\rm km\,s^{-1}}$ ($v\sin(i) = 10\,{\rm km\,s^{-1}}$).

($T_{\rm eff} = 6421 \pm 90$ K, $\log g = 8.10 \pm 0.04$) and ($T_{\rm eff} = 6321 \pm 50$ K, $\log g = 7.97 \pm 0.03$), respectively. Fitting the Ca abundances in the white dwarf atmosphere, we find $\log({\rm Ca/H}) = -10.75 \pm 0.05$ for the spectroscopic parameters, and $\log({\rm Ca/H}) = -10.85 \pm 0.05$ for the photometric ones, in agreement with the results of Rogers et al. (2024a). Our atmosphere models included all elements up to Zn, with the exception of B, F, and Ar, scaled relative to the Ca abundance adopting a bulk Earth composition. No additional metal absorption lines are predicted by the model within the wavelength range covered by the ESPRESSO data, and none were detected.

We used the extremely high resolution of the ESPRESSO spectrum to place an upper limit on the rotational velocity, $v\sin(i) \lesssim 5\,{\rm km\,s^{-1}}$ (See Figure 4.1), corroborating earlier findings that most white dwarfs have rotation periods of many hours to several days (Hermes et al., 2017), too long to detect rotational broadening even in high-resolution spectroscopy (Koester et al., 1998; Berger et al., 2005).

4.3.2 Radial Velocity Analysis

We fitted a Gaussian profile to the Ca K absorption line to measure the radial velocity (RV) at the time of each exposure. We then computed the Lomb-Scargle periodogram from the ASTROPY package (Astropy Collaboration et al., 2022), and calculated the False Alarm Rate (FAR) using the option based on the formulation given by Baluev (2008).

The RVs periodogram (left panel of Fig. 4.2) displays a strong peak at $P = 15.6 \pm 0.9$ d, roughly consistent with half the period of the astrometric planet candidate (P=33.65, Gaia Collaboration et al., 2023a; Holl et al., 2023), although with a FAR of 99 per cent. Another slightly weaker signal is also detected at 10.0 ± 0.4 d.

Besides having such high FAR, each of the found signals present additional reasons for caution: The $\simeq$15 d signal overlaps with a peak rising from the spectral window function, hinting at a possible link to the temporal sampling; and the $\simeq$ 10 d signal coincides with a third of the lunar cycle. In Section 4.4.1, we explore in more detail these systematics, and argue that the $\simeq$ 15.6 d signal stands as our best orbital period candidate.

Upon pre-whitening the $\simeq$10 d period, the $\simeq$15 d signal became stronger by $\sim$30 per cent. And finally, pre-whitening both periods did not uncover new signals in the LS .

Figure 4.2 (right panel) shows the measured radial velocities folded with the 15.6 d period overlaid with a fit to a circular orbit (see Eq. 2.2). The parameters of the optimal fit are listed on Table 4.2.

The systemic velocity derived here, $\gamma = 62.35 \pm 0.07\,\mathrm{km\,s^{-1}}$, is somewhat lower than the average of the radial velocities reported by Rogers et al. (2024a), however, systematic uncertainties in the wavelength zero-point of ESPRESSO (our data), MIKE and X-Shooter (Rogers et al., 2024a) can account for this difference. The latter two instruments are not designed for stable, high-precision radial velocity studies. Indeed, the amplitude determined from the ESPRESSO spectra, $K = 0.19 \pm 0.11\,\mathrm{km\,s^{-1}}$ is well below the radial velocity precision of the MIKE data, $1\,\sigma = 0.47\,\mathrm{km\,s^{-1}}$ (Rogers et al., 2024a).

We attempted the same analysis on the Ca H line, however, due to the broad and overlapping Hϵ line, and the distortions in the flux calibration over wavelength scales comparable to the width of Hϵ, we did not identify any significant variability within that line.

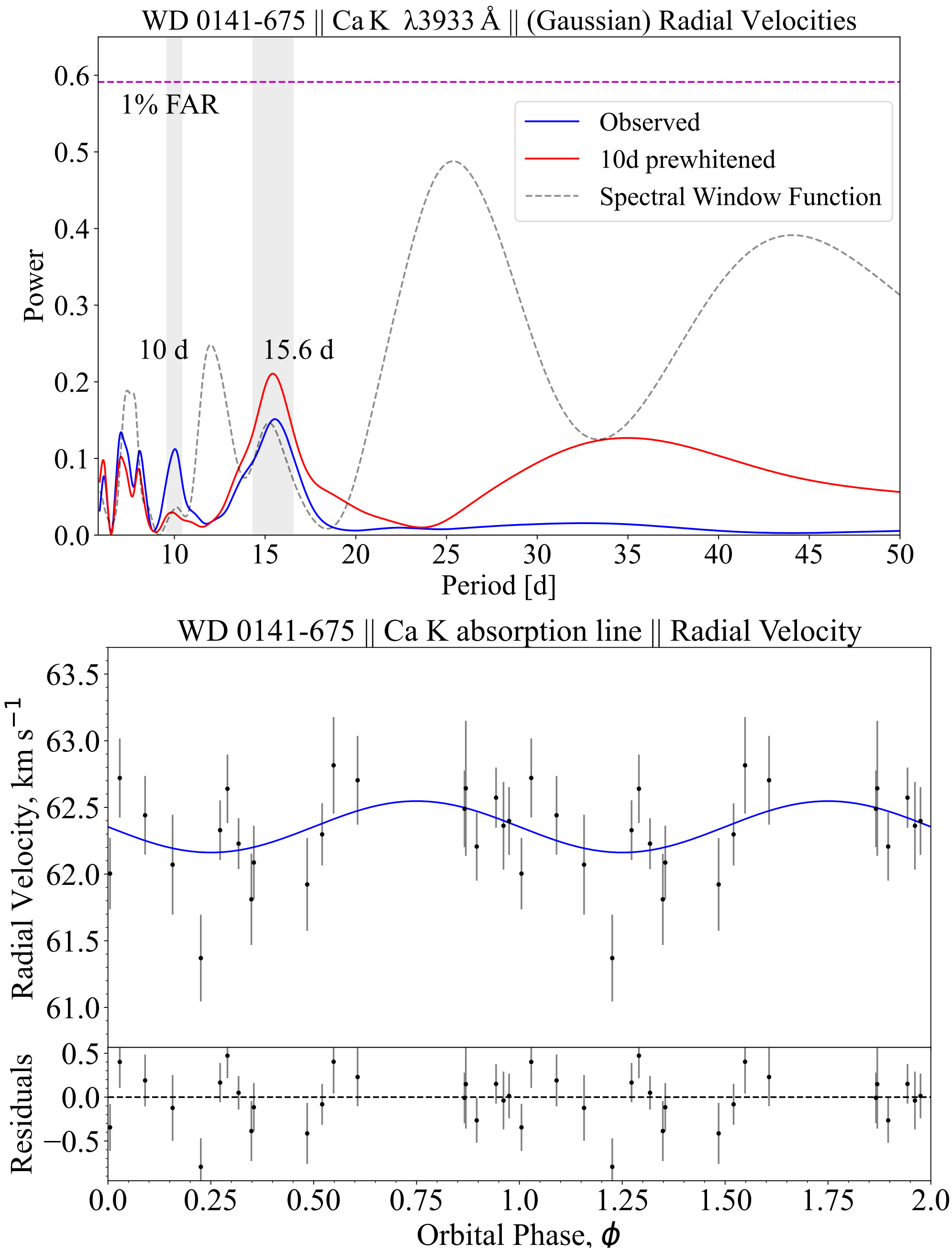

Figure 4.2: Top: LS periodogram of the observed radial velocities obtained for the Ca K absorption line (in blue). The vertical gray bands highlight the strongest powers at 15.6 ± 0.9 d and 10 ± 0.4 d. The red curve is the LS after pre-whitening the $\simeq 10$ d signal. The magenta horizontal dashed line marks the 1 per cent False Alarm Rate. Bottom: Radial velocities of the Ca K absorption line phase-folded on the 15.6 ± 0.9 d period, with the best-fit model of a sine curve overlaid in blue; the residuals are plotted in the bottom panel.

Table 4.2: Optimal sine fit parameters for the radial velocities.

γ [km s^{-1}]	62.35±0.07
K [km s^{-1}]	0.19 ±0.11
t_0 [MJD]	60237.8 ± 1.3
P_{orb} [d]	15.6 ±0.9

Table 4.3: Optimal sine fit parameters for the V/R ratios.

$\gamma^\dagger$	0.992 ± 0.003
$K^\dagger$	0.008 ± 0.004
t_0 [MJD]	60236.2±2.1
P_{orb} [d]	16.7± 1.0

†dimensionless

4.3.3 V/R ratio Analysis

We measured the violet-to-red (V/R) ratio for each ESPRESSO spectrum (e.g. Manser et al., 2019), which is the ratio of blue-shifted to red-shifted flux, centred on the air wavelengths of the Ca K line shifted by the systemic velocity $\gamma = 62.35\,\mathrm{km\,s^{-1}}$ (obtained in Section 4.3.2). The LS periodogram computed from the V/R ratios (Fig. 4.3, left panel) contains a strong signal at $P = 16.1 \pm 0.9\,\mathrm{d}$, which agrees within the uncertainties with the period found in our RV analysis in Section 4.3.2. We note however, that the signal has a high FAR (99 per cent). The periodogram shows two additional comparable signals at $12.5 \pm 0.6\,\mathrm{d}$ and $10.0 \pm 0.3\,\mathrm{d}$.

In contrast to the RV analysis in Section 4.3.2, pre-whitening the $\simeq$10 d signal decreased the power of both the $\simeq$ 16 d and the $\simeq$ 12 d signals. Further pre-whitening of the $\simeq$ 16 d period did not reveal new signals in the LS.

The results of the V/R analysis are sensitive to the interval adopted in the integration of the V/R ratio, whereby wider intervals favoured the strength of the shorter periods, while narrow intervals increased the strength of the $\simeq$ 16 d period. Our final choice was an interval of -35 to $35\,\mathrm{km\,s^{-1}}$ around the core of the line, which yields all three signals with a comparable strength.

We phase-folded the data with the 16.7 d-period and fitted a sine function to the data. The best fit is shown in the right panel of Fig. 4.3, and the corresponding parameters are listed on Table 4.3. As in the RV measurement discussed above, the periodic signal detected in the V/R data is consistent with half of that reported for the retracted planet candidate ($P = 33.65\,\mathrm{d}$). On the other hand, it is worth noting that the amplitude modulation K and systemic offset γ are dimensionless parameters in this analysis, and are therefore not comparable to the parameters obtained in the RV study from Section 4.3.2.

To visualise the variability of the spectra along the orbit, we first computed the average spectrum of all the ESPRESSO observations, subtracted that average from each individual spectrum, and then phase-folded the data on the $\simeq 16$ d period, with the result displayed as a phase-trailed spectrogram in Fig. 4.4. Two tentative sine wave patterns are present in the residual spectrogram (bottom panel of Fig. 4.4), but a spurious origin cannot be discarded without more observations.

We attempted the same V/R analysis on the Ca H line, but similar to Section 4.3.2, the overlapping broad Hϵ absorption impeded a clean V/R measurement.

4.4 Discussion

4.4.1 Systematics Testing

We explored two possible systematic origins for the periodic signals arising in the radial velocity and V/R measurements: The temporal sampling of the ESPRESSO spectra and the lunar cycle. For this purpose we produced 10 000 bootstrap samples of our measurements for which we computed LS periodograms, recording the period with the strongest power in each sample. We then repeated the experiment imposing constraints on the angular separation from the Moon ($> 65°$), the fraction lunar illumination (FLI< 0.85), as well as on the S/N (> 10) around Ca K. We show the histograms of the most frequent strongest periods found in the bootstrap samples in Fig. 4.5. When using the complete set of spectra the same signals dominating the LS periodograms in Sections 4.3.2 and 4.3.3 are those appearing most frequently in the bootstrap histograms. The only exception is the $\simeq 8.0$ d signal in the radial velocity histogram, which is consistent to the harmonic in frequency of the $\simeq$16 d signal. These results suggest that the temporal-sampling is not the cause of the detected signals.

When imposing the lunar and S/N constraints on the radial velocities (top panel of Fig. 4.5), the overall structure remains mostly unaffected. However, in the case of the V/R measurements the signal at $16. \pm 1.0$ d increases its occurrence rate at the expense of a decrease in the occurrence of the $\simeq$10 and 12 d signals.

This marginally hints at sky background contamination as a possible origin for these shorter signals. For this reason, we argue that the signal at $\simeq 16$ d is the best orbital period candidate; but we still issue caution, as further observations are needed to sustain such assessment.

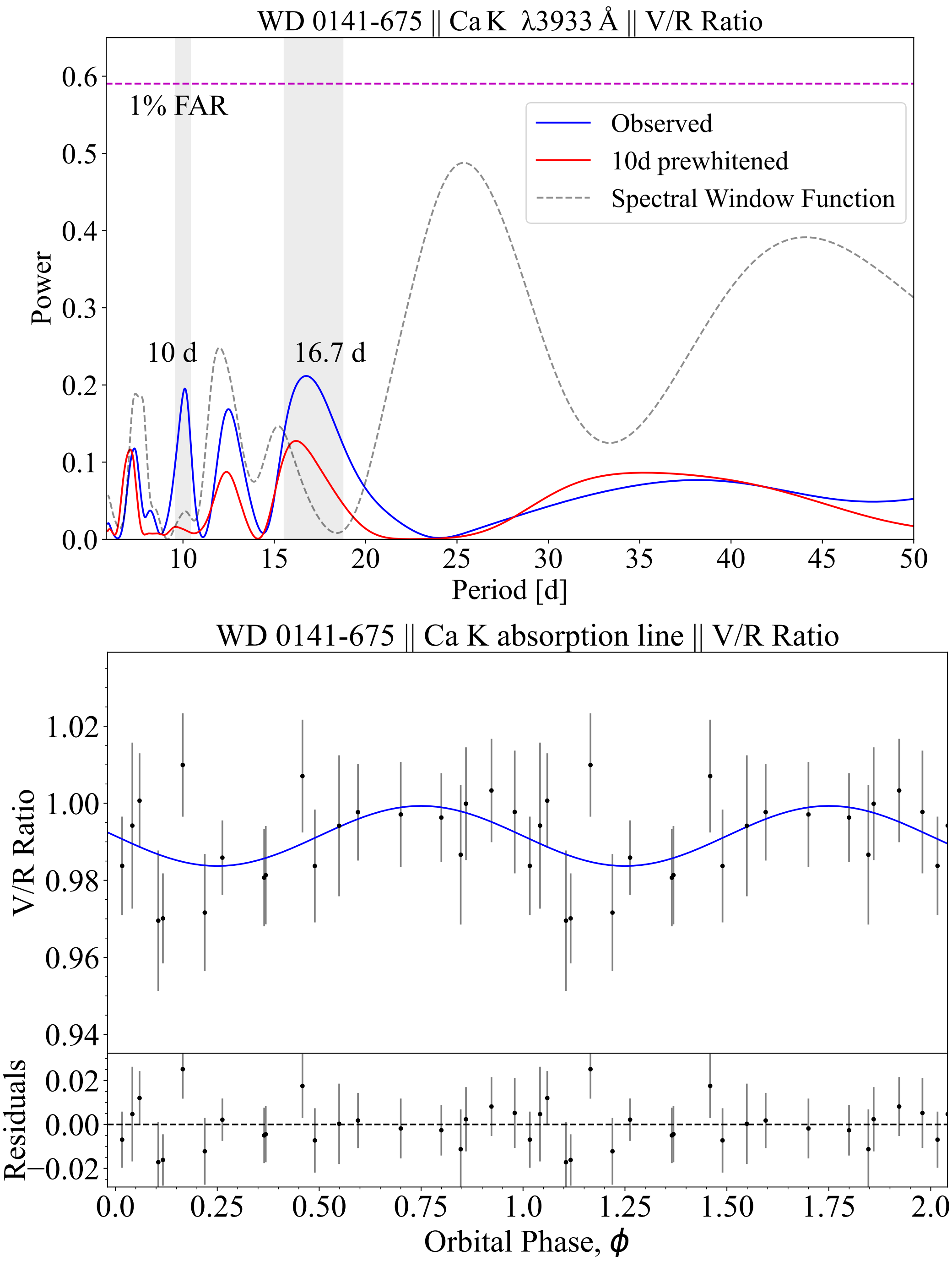

Figure 4.3: Same as Fig. 4.2, but for the V/R ratios of the Ca K line measured from the ESPRESSO spectra. The strongest signals in the LS power spectrum are found at 16.7 ± 0.9 d and 10.0 ± 0.3 d. The right panel depicts the V/R data folded on the 16.7 ± 1.0 d period, overlayed with the best-fit sine function.

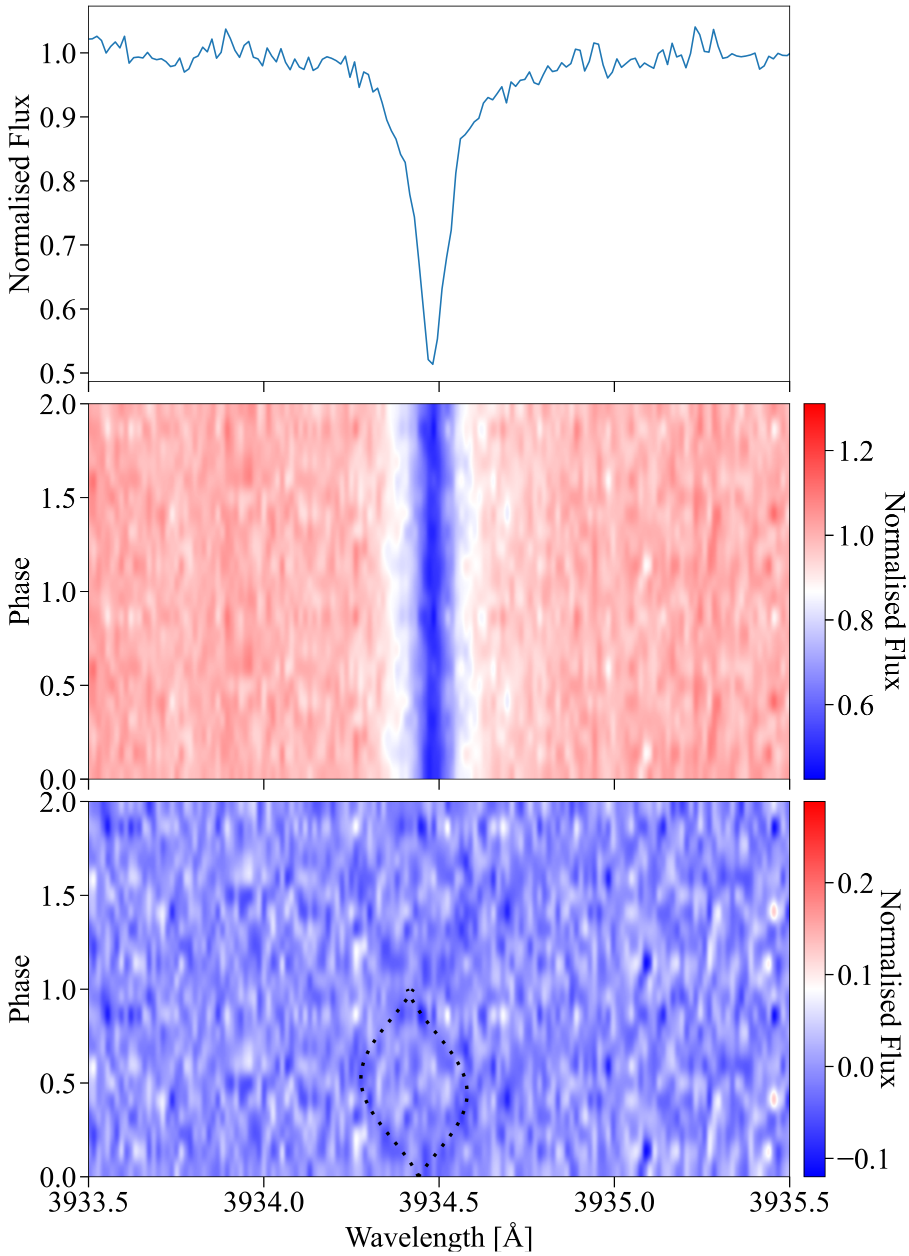

Figure 4.4: Top panel: Continuum normalised average spectrum. Middle panel: Trailed spectrogram constructed from the the time-resolved ESPRESSO data after normalising by the continuum. The individual spectra were folded on the 16.7±1.0 d period and binned in 12 evenly spaced phase bins. We show two phase cycles for visual purposes. Bottom panel: Trailed residuals after subtracting the average spectrum from each exposure. Two sine waves emerge in the residuals which are over-plotted by black dotted sine curves over the first orbit. The latter do not represent a fit to the data but are included only as a guide to the eye.

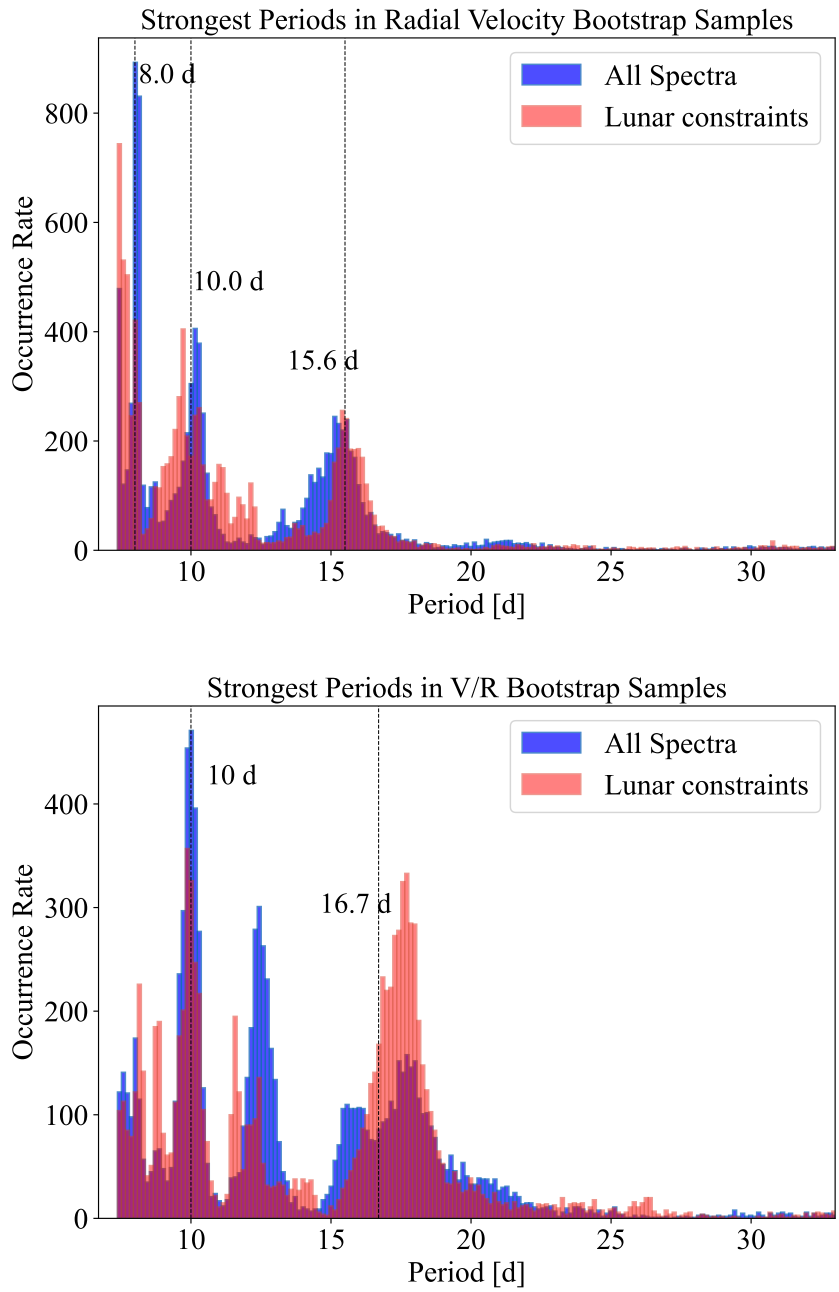

Figure 4.5: Top: Histogram of the strongest periods found in the 10 000 radial velocity bootstrap samples. The blue histogram shows the results of the complete set of spectra. For the red histogram we only considered spectra satisfying the imposed constraints on moon angular separation ($> 65°$), fraction lunar illumination (< 0.85), and S/N (> 10) around Ca K. The vertical dashed lines indicate the position of the strongest periods found in the observed data. Bottom: Same as top panel but for the V/R ratio measurements.

4.4.2 Implications on the Mass Function

In Section 4.3.2, we tentatively detected a radial velocity variation in the Ca K line with $P = 15.6 \pm 0.9$ d and an amplitude of $K = 0.19 \pm 0.11\,\mathrm{km\,s^{-1}}$. Furthermore, a consistent period within the errors of $P = 16.7 \pm 1.0$ d was also found in the V/R analysis (Section 4.3.3). This period agrees within uncertainties with that of the astrometric period candidate ($P = 33.65$ d, Gaia Collaboration et al., 2023a; Holl et al., 2023)

Taking the RV parameters at face value and interpreting them as the circular orbital motion of the white dwarf resulting from a close-in planet leads to the following mass function for the putative companion:

$$f(M_\mathrm{c}) = \frac{PK_\mathrm{wd}^3}{2\pi G} = \frac{(M_\mathrm{c}\sin(i))^3}{(M_\mathrm{wd} + M_\mathrm{c})^2} = 1.20 \times 10^{-5}\,\mathrm{M_{Jup}} \tag{4.1}$$

where G is the gravitational constant and $M_\mathrm{wd} = 0.57 \pm 0.02\,\mathrm{M_\odot}$ the mass of the white dwarf as reported by Rogers et al. (2024a). This mass function constrains the possible values for the inclination (i) and the mass of the companion (M_c), as illustrated in Fig. 4.6. For an orbital inclination $i \lesssim 7^\circ$ the companion would have a mass in the brown dwarf regime, whereas $i \gtrsim 7^\circ$ allows only for a planetary mass companion. The companion mass reported by *Gaia*, $\mathrm{M_c} = 9.26^{+2.64}_{-1.15}\,\mathrm{M_{Jup}}$, yields an orbital inclination of $i = 10.20^\circ$ in our analysis, which is in stark disagreement with the inclination of $i = 87.0 \pm 4.1^\circ$ inferred from Monte Carlo resampling by Gaia Collaboration et al. (2023b). However, we remind the reader that the astrometric solution for WD 0141–675 has been retracted by the *Gaia* team. We also note that while the available *Spitzer* and *WISE* photometry rules out a brown dwarf companion (see section 3.3 of Rogers et al. 2024a for a detailed discussion), a more stringent photometric limit on the existence of a planetary companion could be derived from deep *JWST* infrared observations[3].

In summary, interpreting the radial velocity variation tentatively detected in the ESPRESSO data as the reflex motion of the white dwarf, in conjunction with the existing infrared data on WD 0141–675, implies possible solutions for a planetary companion with a lower limit of $\sim 7^\circ$ on the orbital inclination. We stress, however, that the radial velocity signal in the ESPRESSO data is not sufficiently significant to claim any detection of a companion.

[3]The approved *JWST* program GO 3652 intended to obtain these observations, but was withdrawn in the wake of the retraction of WD 0141–675. We argue that a better constraint on the nature of a possible companion to WD 0141–675 remains of interest.

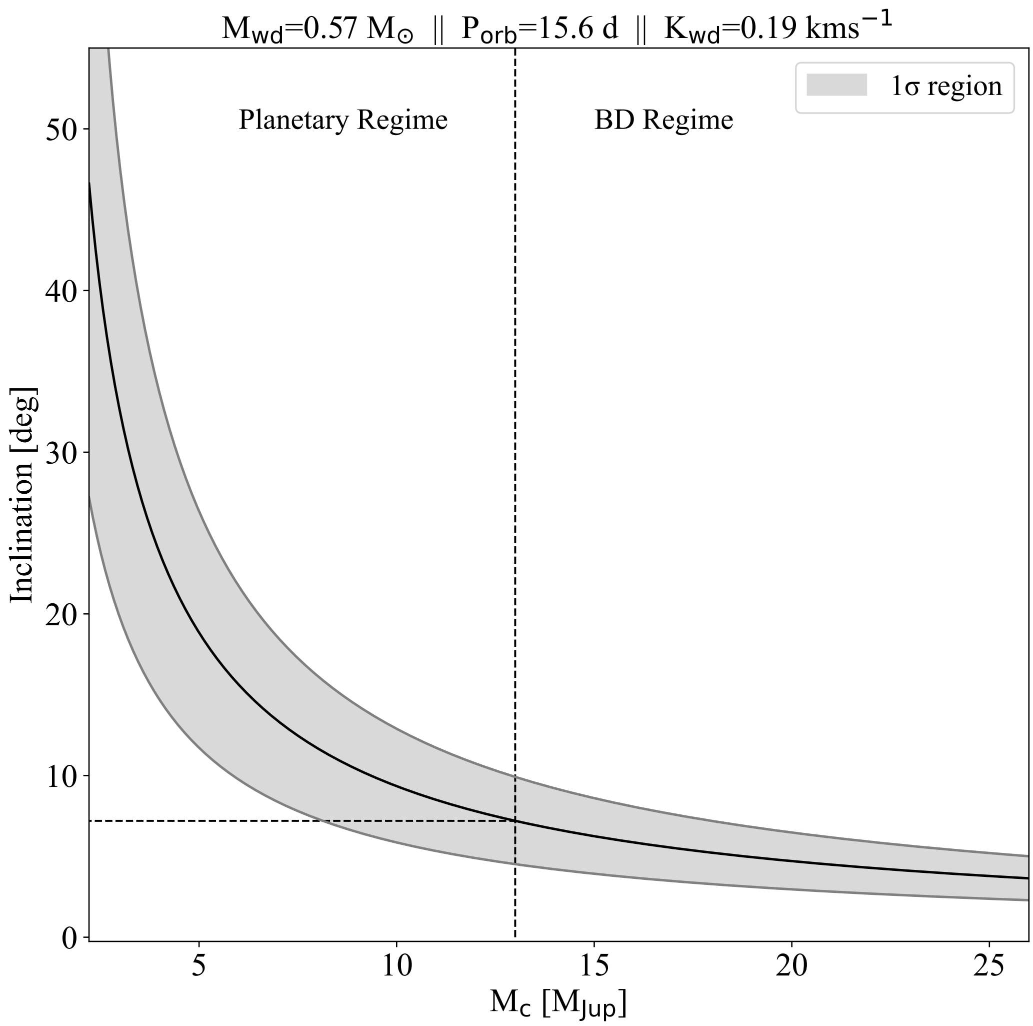

Figure 4.6: Mass function of a putative companion to WD 0141–675, calculated from the orbital parameters measured from the radial velocity analysis (Section 4.3.2, Table 4.2). The black line represents the mass function of the central values corresponding to $P_{\rm orb} = 15.6 \pm 0.9$ d and $K_{\rm wd} = 0.19 \pm 0.11\,{\rm km\,s^{-1}}$. The grey region shows the constraints on the inclination and mass of a possible companion within the 1σ region implied by the uncertainties in our measurements. The dashed vertical line indicates the $13\,{\rm M_{Jup}}$ threshold above which the companion could also be a brown dwarf. Assuming a planetary companion, the mass boundary implies a lower limit on the inclination of $i = 7 \pm 4^{\circ}$, indicated by the dashed horizontal line.

4.5 Conclusions

WD 0141–675 was reported as hosting the first astrometrically detected white dwarf planet candidate (Gaia Collaboration et al., 2023a; Holl et al., 2023), but was later retracted as a false positive. We have obtained time-resolved high-resolution spectroscopy of WD 0141–675 with ESPRESSO, an instrument which allows highly accurate velocity shift measurements (e.g. Pasquini et al., 2023). Adopting the atmospheric parameters from the photometric solution of Rogers et al. (2024a), we obtained a Ca abundance of $\log(\mathrm{Ca/H}) = -10.75 \pm 0.05$ dex, in good agreement with the values reported by these authors. The narrow width of the Ca K lines yielded an upper limit on the rotational broadening of $v \sin i \simeq 5\,\mathrm{km\,s^{-1}}$. This is suggestive of a slow rotator, which is a common result in spectroscopic determinations of rotating rates in white dwarfs (Berger et al., 2005).

Analysing the radial velocities and the V/R ratio of the Ca K line both result in a tentative detection of variability with a period of $\simeq 15 - 16$ d, which cannot be attributed to the temporal sampling. Phase-folding the ESPRESSO spectroscopy on such signal exhibits weak periodical variability in the morphology of Ca K near its core. Fitting the radial velocities with a circular orbit results in an amplitude of $K = 0.19 \pm 0.11\,\mathrm{km\,s^{-1}}$. Interpreting this variation as the (circular) reflex motion of the white dwarf implies that possible solutions to the mass function exist within the planetary mass regime. Therefore, when discarding a brown dwarf companion from existing infrared photometry (Rogers et al., 2024a) a lower limit on the orbital inclination of $i \gtrsim 7°$ is established.

Whereas we stress that the measured radial velocity variation is not statistically significant, our analysis demonstrates that ESPRESSO observations are entirely sensitive to detecting planets on close-in orbits around white dwarfs. We encourage additional ESPRESSO observations, as well as deep infrared photometry to increase the dynamic and photometric constraints on a putative companion to WD 0141–675.

Chapter 5

Through the Looking Gas: A Tomography Atlas of Three White Dwarf Gaseous Debris Discs

"What I tell you three times is true."

Lewis Carrol

5.1 Introduction

Planetary systems are expected to survive the evolution of their host stars into white dwarfs (WDs) (Duncan & Lissauer, 1998; Debes & Sigurdsson, 2002; Villaver & Livio, 2007; Veras & Gänsicke, 2015). A plethora of indirect observational evidence unambiguously confirms this view: metal enrichment of WD atmospheres caused by accretion (Zuckerman et al., 2010; Barstow et al., 2014; Koester et al., 2014); observations of debris transits (Vanderburg et al., 2015); accretion of an evaporating giant planet (Gänsicke et al., 2019); as well as detection of intact exoplanet transits (Vanderburg et al., 2020).

To survive engulfment, these planetary bodies must have migrated onto close-in orbits after the progenitor's giant phase. A mere 1-3 percent of WDs display an infrared excess (Zuckerman & Becklin, 1987; Rocchetto et al., 2015; Dennihy et al., 2016; Vanderburg et al., 2020; Barber et al., 2016) , suggestive that some planetary bodies are gravitationally destabilised onto highly eccentric orbits that take them within the tidal disruption radius ($\simeq 1\,\mathrm{R_\odot}$) (Zuckerman & Becklin, 1987; Farihi, 2009). At this point they become ripped apart forming a dusty debris disc bound to be accreted by the WD (Veras et al., 2014, 2015; Malamud & Perets, 2020).

An even rarer subset of WDs ($\simeq$0.067%, Manser et al., 2020) are found to show a gaseous component co-orbiting with the dust (Melis et al., 2010), principally detected via the Ca II triplet 8600 Å double-peaked emission (e.g. Gänsicke et al., 2006b, 2007). The gas production mechanism remains unclear, but the recent detection of an embedded planetesimal orbiting within the dust disc of SDSS J1228+1040 (Manser et al., 2019), suggests the gaseous component could be a tracer for the presence of planetesimals.

The gaseous emission lines have been observed to show morphological variations on time-scales of years to decades (Wilson et al., 2015; Manser et al., 2016a,b, 2021). This variability has been analysed with Doppler tomography (Marsh & Horne, 1988), whereby the produced maps were interpreted as a constant non-axisymmetric structure precessing around the WD (Manser et al., 2016a, 2021). This agrees with theoretical studies showing that relativistic effects and gas pressure forces should indeed cause the eccentric disc to precess (Miranda & Rafikov, 2018).

Doppler tomography presents a unique opportunity to unveil the disc emission distribution and understand its structure. Despite this, only two precessing discs have been previously mapped (SDSS J1228+1040 and HE 1349–2305, Manser et al., 2016a, 2021). The dearth of mapped systems is owed to the need of continuous spectroscopic monitoring throughout ∼0.5 of the precession period. But the precession cycles tend to be of the order of years to decades, and still unknown for most systems. We refined the precession periods of the published objects and updated their Doppler maps using new spectroscopy from a long monitoring campaign. Most notably, as part of this campaign we computed the first Doppler map of SDSS J1043+0855, making it only the third of the 21 known WD gaseous discs (Gänsicke et al., 2006b, 2007, 2008; Gänsicke, 2011; Melis et al., 2012; Farihi et al., 2012; Wilson et al., 2014; Melis et al., 2020; Dennihy et al., 2020).

HE 1349–2305

HE 1349–2305 has been classified as a helium dominated WD with traces of hydrogen and metals (DBAZ). It shows an infrared excess (Girven et al., 2012), as well as Ca II Triplet emission, betraying the presence of both a dust and gas disc components. The gas emission has been measured to vary morphologically on a time-scale range

$\simeq$ 459-502 d ($\simeq$1.4 yrs, Melis et al., 2012; Dennihy et al., 2018; Manser et al., 2021).

Short cadence ($\simeq$4 min) observations of HE 1349–2305 do not show variability on typical timescales of orbital periods for planetesimals (minutes to hours) (Manser et al., 2021), which would unambiguously indicate the presence of an embedded planetesimal within the disc; as was the case for SDSS J1228+1040, whereby a stable periodic variation of $\simeq$ 123 min was found (Manser et al., 2019). Nonetheless, Manser et al. (2021) studied the variability of HE 1349–2305 with Doppler tomography, which revealed an asymmetric intensity distribution that was interpreted as a fixed precessing structure.

The relatively short precessional cycle of this object makes it a perfect candidate to study the stability of said period. Towards this end, we compiled the observations of HE 1349–2305 covering $\simeq$2 cycles from Dennihy et al. (2018) and Manser et al. (2021), and included new spectra taken from 2020 onwards; thus extending the baseline to $\simeq$ 5 precessional cycles. Finally, with the new spectroscopy we also updated its previously published Doppler Tomography (Manser et al., 2021).

SDSS J1043+0855

SDSS J1043+0855 was discovered by Gänsicke et al. (2007), from the detection of the Ca II Triplet emission. It is a warm (17 879 $\pm$ 195 K, Manser et al., 2016b) metal-enriched hydrogen-dominated WD (DAZ). It has been found to be accreting mantle- and crust-rich material (Melis & Dufour, 2017), and *Spitzer* observations have identified the presence of a dust disc from infrared excess (Brinkworth et al., 2012).

Observations taken throughout a timespan of 9 years revealed morphological variability of the Ca II lines (Manser et al., 2016b), however due to the low number of observations, the variability period was not constrained. We extended the baseline of spectroscopic observations which enabled us to measure the variability period, allowing us in turn to compute the first Doppler Tomography of SDSS J1043+0855.

SDSS J1228+1040

SDSS J1228+1040 became the first discovery of a WD hosting a gaseous debris disc (Gänsicke et al., 2006b), due to the detection of Ca II Triplet emission in spectroscopic observations from the Sloan Digital Sky Survey (SDSS; York et al., 2000). With a warm temperature of $T_{\rm eff}$ = 20 713 $\pm$ 281 K (Koester et al., 2014), this object also exhibits photospheric metal enrichment (Gänsicke et al., 2012) and infrared excess (Brinkworth et al., 2009).

The gaseous debris disc of SDSS J1228+1040 was also the first to be mapped with Doppler tomography (Manser et al., 2016a). Like HE 1349–2305, it exhibited an asymmetric intensity distribution, interpreted as a rigidly precessing eccentric structure; in agreement with theoretical models of the line emission (Goksu et al., 2024). Furthermore, the object also shows short-term periodic variation ($\simeq$123 min) in strength and shape of the Ca II emission, compelling evidence of an orbiting planetesimal within the dust disc (Manser et al., 2019). These findings suggest a link between the gas emission and planetesimals orbiting within the disruption radius of WDs.

Its long precession period was estimated to be of the order of $\simeq$ 27yrs (Manser et al., 2016a), meaning that the gas emission has not yet completed a full cycle since its first spectroscopic observation in 2003 (Gänsicke et al., 2006b). We extend on the previously published observations from (Manser et al., 2016a) to impose stricter contraints on the precessional period and re-compute its Doppler tomography.

5.2 Observations

We compiled optical spectroscopic observations from various instruments for all three objects. We show in Tables 5.1, 5.2 and 5.3, the observations for HE 1349–2305, SDSS J1043+0855, and SDSS J1228+1040, respectively. We note that for HE 1349–2305 the epochs within 2009-05-20 and 2019-06-06 were used to compute its Doppler tomography in Manser et al. (2021). Analogously for SDSS J1228+1040 in Manser et al. (2016a) with the epochs from 2003-03-27 to 2015-05-11. Our follow-up observations were obtained from similar instrumental setups as Manser et al. (2016a) and Manser et al. (2021), where their respective processing is described in detail.

The list of used instruments is as follows: The 2.5 m Sloan Digital Sky Survey (SDSS) telescope, with retrievals from DR7 and DR9 (Gunn et al., 2006; Abazajian et al., 2009; Eisenstein et al., 2006); The Intermediate dispersion Spectrograph and Imaging System (ISIS) on the William Herschel Telescope (WHT); from the Very Large Telescope (VLT): X-shooter (Vernet et al., 2011), FOcal Reducer and low dispersion Spectrograph (FORS2), and the Ultraviolet and Visual Echelle Spectrograph (UVES Dekker et al., 2000), reduced with the REFLEX reduction pipeline (Freudling et al., 2013) and telluric corrected with MOLECFIT (Kausch et al., 2015; Smette et al., 2015); the Goodman High Throughput Spectrograph (Goodman) in the Southern Astrophysical Research (SOAR) telescope, using the 1200l-R grating and reduced with a custom PYTHON toolkit (see Dennihy et al., 2018) based on the methods by Marsh (1989). Magellan/Magellan Inamori Kyocera Echelle (MIKE Bernstein et al., 2003), reduced and extracted using the Carnegie PYTHON MIKE data-reduction pipeline (Kelson, 2003); and finally the Gemini Multi-Object Spectrograph (GMOS-S) mounted on the *Gemini South* (e.g., Gimeno et al., 2016), collected with the R-831 grating, and reduced using a combination of the Gemini IRAF package and a routine described in Marsh (1989).

Table 5.1: Observations and measurements of HE 1349–2305. The epochs from 2009-05-20 to 2019-06-06 were used to compute Doppler Tomography Manser et al. (2021). The epochs from 2020-03-18 onwards are new observations used for the updated Doppler image in Section 5.4.

Date	MJD	Instrument	Velocity [km/s]	V/R dimensionless
2009-05-20	54971	*Magellan*/MIKE	49 ± 66	0.83 ± 0.11
2011-05-27	55708	*VLT*/X-Shooter	-13 ± 12	0.91 ± 0.04
2016-08-21	57621	*SOAR*/Goodman	-186 ± 16	2.77 ± 0.22
2017-01-12	57765	*SOAR*/Goodman	176 ± 44	0.59 ± 0.04
2017-01-25	57778	*SOAR*/Goodman	87 ± 34	0.66 ± 0.04
2017-02-05	57789	*GTC*/OSIRIS	222 ± 57	0.43 ± 0.03
2017-02-09	57793	*SOAR*/Goodman	120 ± 26	0.57 ± 0.03
2017-02-17	57801	*SOAR*/Goodman	209 ± 30	0.38 ± 0.02
2017-03-10	57822	*SOAR*/Goodman	229 ± 15	0.29 ± 0.02
2017-03-14	57826	*SOAR*/Goodman	221 ± 28	0.32 ± 0.04
2017-04-11	57854	*SOAR*/Goodman	247 ± 14	0.19 ± 0.02
2017-04-11	57854	*SOAR*/Goodman	233 ± 10	0.26 ± 0.02
2017-04-23	57866	*SOAR*/Goodman	235 ± 15	0.21 ± 0.03
2017-05-30	57903	*SOAR*/Goodman	212 ± 11	0.25 ± 0.03
2017-06-09	57913	*SOAR*/Goodman	189 ± 30	0.31 ± 0.03
2017-07-25	57959	*SOAR*/Goodman	63 ± 19	0.71 ± 0.04
2017-08-02	57967	*SOAR*/Goodman	97 ± 52	0.74 ± 0.05
2018-02-04	58153	*SOAR*/Goodman	-183 ± 15	3.17 ± 0.30
2018-02-10	58159	*SOAR*/Goodman	-158 ± 16	2.88 ± 0.30
2018-03-27	58204	*SOAR*/Goodman	-55 ± 62	1.44 ± 0.12
2018-04-27	58235	*SOAR*/Goodman	141 ± 56	0.79 ± 0.07
2018-05-15	58253	*VLT*/X-Shooter	87 ± 38	0.82 ± 0.04
2018-06-02	58271	*SOAR*/Goodman	174 ± 45	0.59 ± 0.04

Table 5.1: Observations and measurements of HE 1349–2305 (continued)

Date	MJD	Instrument	Velocity [km/s]	V/R dimensionless
2019-03-09	58551	*Gemini South*/GMOS-S	-243 ± 8	5.55 ± 0.19
2019-03-16	58558	*Gemini South*/GMOS-S	-228 ± 8	5.98 ± 0.18
2019-03-24	58566	*SOAR*/Goodman	-213 ± 11	4.10 ± 0.45
2019-04-23	58596	*SOAR*/Goodman	-213 ± 48	3.43 ± 0.84
2019-05-15	58618	*SOAR*/Goodman	-199 ± 10	3.51 ± 0.33
2019-06-06	58640	*VLT*/X-Shooter	-152 ± 12	2.43 ± 0.11
2020-03-18	58926	FORS2	-76 ± 8	1.23 ± 0.01
2021-07-27	59422	*SOAR*/Goodman	-212 ± 30	2.21 ± 0.47
2022-03-29	59667	*SOAR*/Goodman	235 ± 14	0.23 ± 0.04
2022-04-11	59680	*VLT*/X-Shooter	239 ± 4	0.21 ± 0.01
2022-05-07	59706	*VLT*/X-Shooter	226 ± 4	0.19 ± 0.01
2022-06-24	59754	*VLT*/X-Shooter	33 ± 22	0.78 ± 0.02
2022-07-25	59785	*VLT*/X-Shooter	-99 ± 14	1.27 ± 0.03
2023-01-20	59964	*VLT*/X-Shooter	16 ± 25	0.89 ± 0.02
2023-02-25	60000	*VLT*/X-Shooter	172 ± 20	0.48 ± 0.01
2023-03-19	60022	*VLT*/X-Shooter	258 ± 7	0.17 ± 0.01
2023-04-14	60048	*VLT*/X-Shooter	238 ± 10	0.25 ± 0.01
2023-05-14	60078	*VLT*/X-Shooter	220 ± 6	0.24 ± 0.01
2023-06-12	60107	*VLT*/X-Shooter	182 ± 11	0.40 ± 0.01
2023-06-12	60107	*VLT*/X-Shooter	181 ± 7	0.33 ± 0.01
2023-08-13	60169	*VLT*/X-Shooter	-68 ± 14	1.19 ± 0.03
2025-05-02	60797	*VLT*/X-Shooter	155 ± 9	0.44 ± 0.01
2025-05-20	60815	*VLT*/X-Shooter	131 ± 11	0.59 ± 0.01
2025-06-28	60854	*VLT*/X-Shooter	-82 ± 20	1.23 ± 0.02
2025-07-15	60872	*VLT*/X-Shooter	-158 ± 20	1.72 ± 0.04

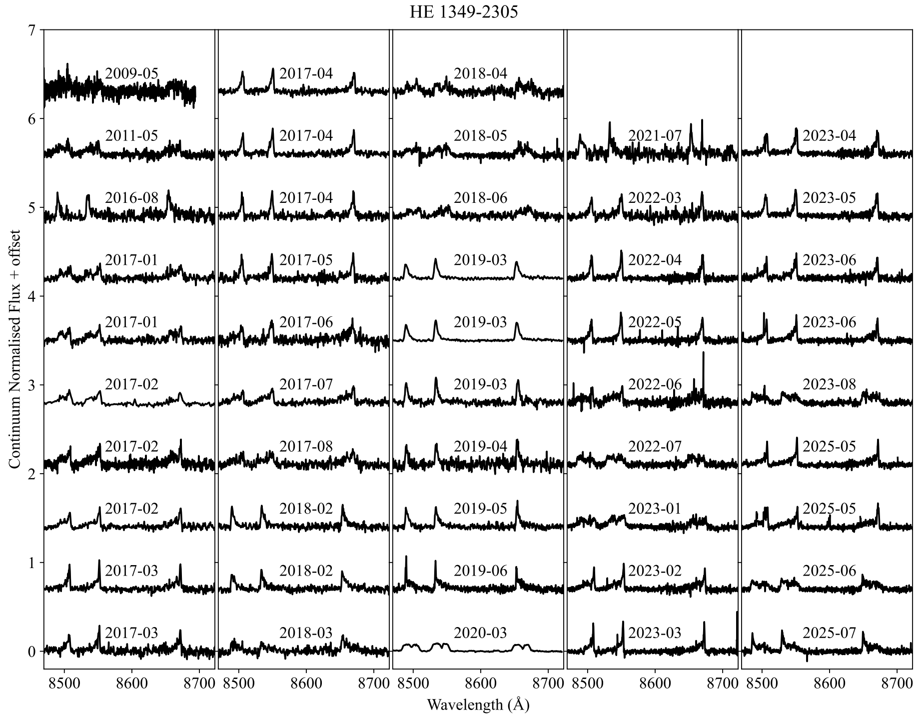

Figure 5.1: Ca II 8600 Å triplet emission profiles of HE 1349–2305 exhibiting morphological variation with a period of ≃1.2 yrs.

Table 5.2: Observations and measurements of SDSS J1043+0855. The complete list of observations on this list were used to compute the first Doppler tomography of SDSS J1043+0855 in Section 5.4.

Date	MJD	Instrument	Velocity (±)	V/R (±)
2003-04-05	52734	SDSS	-237 ± 391	0.90 ± 0.22
2007-02-03	54134	*WHT*/ISIS	30 ± 79	0.96 ± 0.15
2009-02-16	54878	*WHT*/ISIS	41 ± 55	1.37 ± 0.25
2010-04-22	55308	*WHT*/ISIS	-114 ± 36	0.89 ± 0.09
2011-01-29	55590	*VLT*/X-shooter	93 ± 61	0.72 ± 0.02
2011-05-30	55712	*VLT*/X-shooter	131 ± 15	0.77 ± 0.02
2012-01-03	55929	SDSS	176 ± 29	0.85 ± 0.10
2017-03-14	57826	*SOAR*/Goodman	95 ± 45	1.00 ± 0.01
2018-04-08	58216	*VLT*/X-shooter	-9 ± 23	1.23 ± 0.03
2020-03-16	58924	FORS2	-39 ± 50	1.10 ± 0.01
2022-04-06	59675	*VLT*/X-shooter	171 ± 8	0.95 ± 0.02
2023-01-18	59962	*VLT*/X-shooter	1 ± 14	1.16 ± 0.02
2023-03-15	60018	*VLT*/X-shooter	105 ± 26	1.13 ± 0.02
2023-04-14	60048	*VLT*/X-shooter	-115 ± 18	1.26 ± 0.03
2025-04-26	60792	*VLT*/X-shooter	-31 ± 54	0.91 ± 0.02

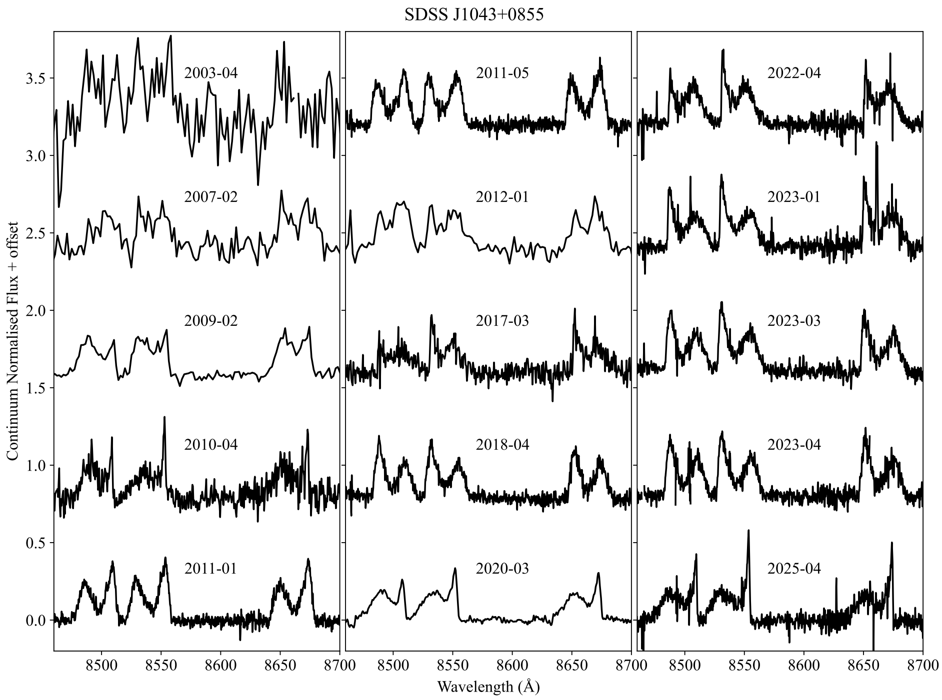

Figure 5.2: Ca II 8600 Å triplet emission profiles of SDSS J1043+0855 exhibiting morphological variation. We note that spectra taken between $\simeq 4-5$ yrs apart show similar structure, in accordance with the selected optimal periods obtained from the velocity centroid and V/R analyses.

Table 5.3: Observations and measurements of SDSS J1228+1040. The epochs from 2003-03-27 to 2015-05-11 were used to compute Doppler Tomography in Manser et al. (2016a). The epochs from 2016-03-07 onwards are new observations used for the updated Doppler image in Section 5.4.

Date	MJD	Instrument	Velocity (±)	V/R (±)
2003-03-27	52725	SDSS	214 ± 33	0.89 ± 0.18
2006-07-01	53917	*WHT*/ISIS	121 ± 5	0.99 ± 0.01
2007-04-07	54197	*VLT*/UVES	69 ± 6	1.02 ± 0.02
2007-06-30	54281	*VLT*/UVES	60 ± 6	1.07 ± 0.02
2007-07-10	54291	*VLT*/UVES	57 ± 4	1.09 ± 0.02
2008-01-10	54475	*VLT*/UVES	63 ± 8	1.11 ± 0.03
2008-06-27	54644	*VLT*/UVES	64 ± 17	1.13 ± 0.05
2008-07-19	54667	*VLT*/UVES	66 ± 5	1.10 ± 0.02
2009-02-03	54865	*VLT*/UVES	74 ± 5	1.05 ± 0.02
2009-04-04	54925	*VLT*/UVES	67 ± 4	1.11 ± 0.02
2010-04-27	55313	*WHT*/ISIS	67 ± 12	1.12 ± 0.03
2011-01-22	55583	*VLT*/X-Shooter	62 ± 2	1.14 ± 0.00
2011-05-29	55710	*VLT*/X-Shooter	85 ± 3	1.08 ± 0.01
2011-06-14	55726	*VLT*/X-Shooter	85 ± 4	1.08 ± 0.01
2012-03-26	56012	*VLT*/X-Shooter	85 ± 4	1.09 ± 0.01
2014-03-06	56722	*VLT*/X-Shooter	92 ± 6	1.04 ± 0.00
2014-06-02	56811	*VLT*/X-Shooter	76 ± 3	1.06 ± 0.00
2015-05-11	57153	*VLT*/X-Shooter	60 ± 3	1.10 ± 0.00
2016-03-07	57454	*VLT*/UVES	78 ± 3	1.00 ± 0.01
2016-05-23	57532	*VLT*/UVES	75 ± 5	0.99 ± 0.02
2017-03-01	57814	*VLT*/UVES	69 ± 3	0.99 ± 0.01
2017-04-05	57848	*VLT*/X-Shooter	56 ± 3	1.01 ± 0.00
2018-03-01	58178	*VLT*/X-Shooter	70 ± 5	0.97 ± 0.00
2018-05-04	58242	*VLT*/X-Shooter	67 ± 4	0.96 ± 0.00
2019-02-19	58533	*VLT*/X-Shooter	42 ± 5	1.01 ± 0.00
2019-04-28	58601	*VLT*/X-Shooter	44 ± 5	1.01 ± 0.00
2025-05-26	60821	X-Shooter	61 ± 4	0.98 ± 0.00

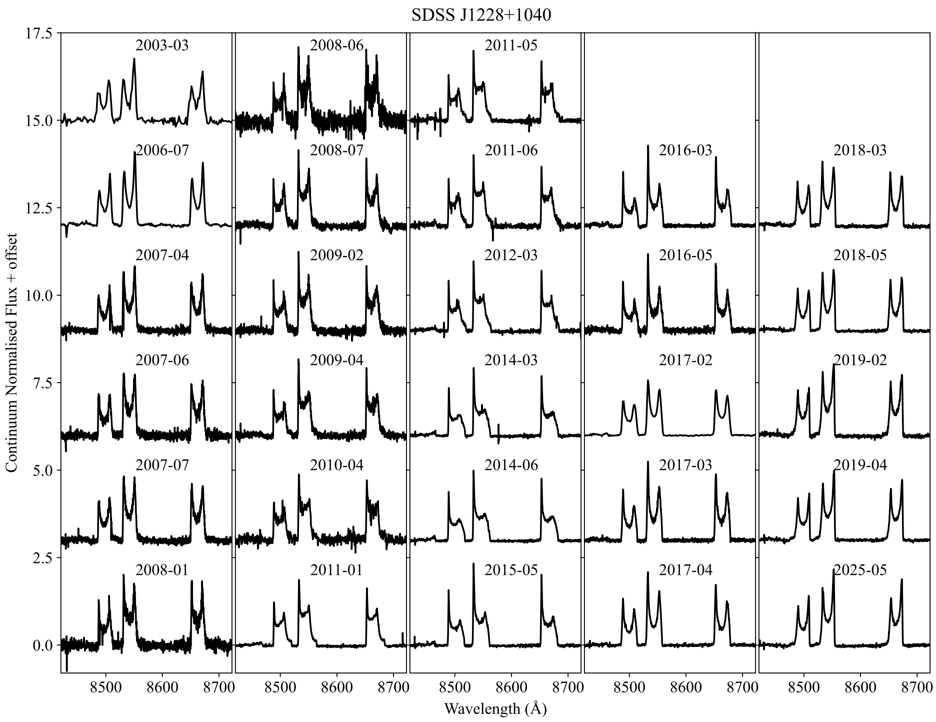

Figure 5.3: Ca II 8600 Å triplet emission profiles of SDSS J1228+1040 exhibiting morphological variation. We note that spectra taken between $\simeq 25$ yrs apart show similar structure, in accordance with the selected optimal periods obtained from the velocity centroid and V/R analyses.

5.3 Period Search of the Ca II triplet emission

We obtained the velocity centroid of the Ca II triplet emission by calculating the cumulative equivalent width, as outlined in Dennihy et al. (2018). These flux-weighted average velocities track the morphological variations of the emission profiles as they oscillate between blue- and red-dominated stages. The weighted average of the velocity centroid of the Ca II triplet were obtained at each epoch. We then used the analysis of variance (ANOVA) method to search for a period in the unevenly sampled data (Schwarzenberg-Czerny, 1996). As a complementary study, we also measured the violet-to-red (V/R) ratio for each spectrum (e.g. Manser et al., 2019; Ramírez et al., 2025), which is the ratio of blue-shifted to red-shifted flux, centred on the air wavelengths of the Ca emission line shifted by the systemic velocity.

Using the measured optimal periods, we phase-folded the velocity centroids and implemented a sinusoidal fit to show the respective periodical variability. We briefly describe the periodograms of each object in the following Sections.

HE 1349–2305

The velocity periodogram of HE 1349–2305 (top left panel of Fig. 5.4) shows a clear maximum at a frequency of 0.002247 ± 0.00002 c/d, corresponding to a period of 445 ± 3d. Two other periods exceed the 99% significance threshold at ~ 325 and 200 d. However, visual inspection of the velocities folded by these signals (and the Ca II profiles in Fig. 5.1) revealed their alias nature. Overall the V/R ratios show the same structure, with the same signals dominating the periodogram. Therefore, we select 445 ± 3d as our optimal period. This breaks the degeneracy of the two periodicities reported in the literature ($\simeq$462 and 502 d, Manser et al., 2021), and comes to show the importance of good orbital coverage as a means of constraining the true period. We note however, that while the phase-folded velocities have a sensible sinusoidal variation, the fit struggles in the phase range of $\simeq 0.75 - 1$. We discuss the stability of the found period in Section 5.5.3

SDSS J1043+0855

Both periodograms of SDSS J1043+0855 show a complex structure with multiple peaks of comparable power exceeding the 99% significance threshold. The phase-folded curve of these peaks were visually inspected with a 1747 d ($\simeq$ 4.7 yrs) period showing the clearest sinusoidal variability. This period agrees well with the theoretical prediction of 4.3 yrs modelled for precession driven by general relativity (Miranda & Rafikov, 2018). Furthermore, inspecting the emission profiles (Fig. 5.2)

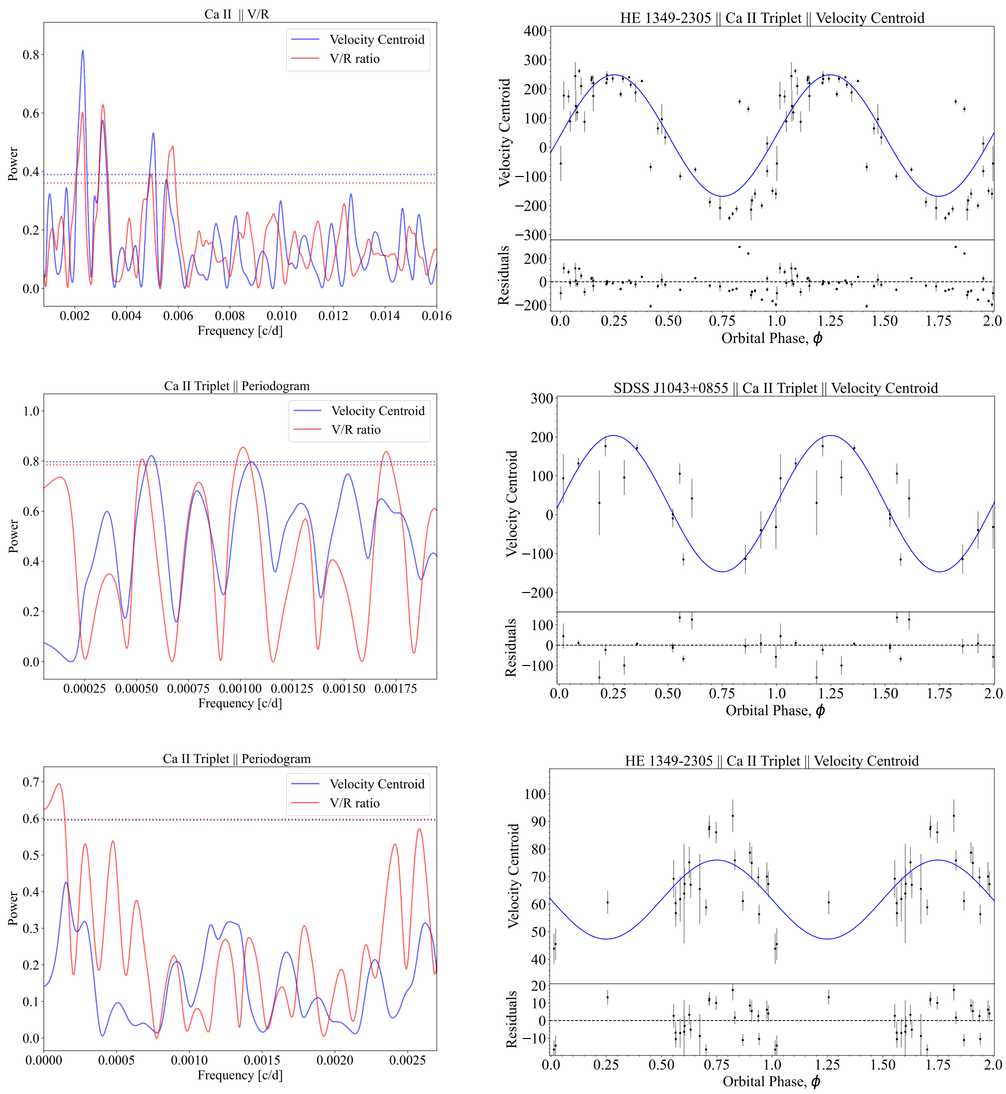

Figure 5.4: Left: Periodograms of the observed radial velocities obtained from the Ca II triplet centroids (in blue). The periodograms of the V/R ratios are also included for comparison (red). The dotted horizontal lines (each in corresponding colour) represent the false alarm rate (FAR) threshold of 0.01. Right: Velocity centroids phase-folded by the selected optimal periods, overlaid by a sinusoidal fit, showing also the residuals underneath each curve. The data is repeated a second orbit for visual purposes. The analyses of the objects are arranged from top to bottom in ascending order of the found precession periods: HE 1349–2305 ($P \simeq 1.2$ yrs), SDSS J1043+0855 ($P \simeq 4.8$ yrs), and SDSS J1228+1040 ($P \simeq 25$ yrs).

shows they recover their morphological structure every $\simeq 4-5$ yrs; in line with our selected period.

The V/R ratio periodogram exhibits a strong peak around this frequency neighbourhood at 1890 d. However similar to the aliases present in the velocity's periodogram, folding by the V/R periods does not result in sinusoidal variability. The selection of the 1747 d period was also confirmed in the Doppler tomography analysis.

SDSS J1228+1040

The velocity periodogram does not show any statistically significant signal. Its strongest signal is at a frequency of 0.00015 ± 0.00002 c/d, corresponding to a precessional period of $\simeq$6477 d ($\simeq$18 yrs). However the emission line profiles complete half a precessional cycle over at least $\simeq 11-12$ yrs (Fig. 5.3). This is in better agreement with the strongest signal yielded by the V/R periodogram of 0.000106 ± 0.00002 c/d ($\simeq$25 yrs). This period is within the constraints estimated in Manser et al. (2016a) of $\simeq 24-27$ yrs. Folding by this period does show a sinusoidal behaviour of the velocities, although, a phase coverage spanning the full orbit is still needed to refine this measurement.

5.4 Doppler Tomography

Doppler tomography is an indirect imaging technique that interprets the morphological variability of phase-resolved emission line profiles, and produces a two-dimensional intensity map in velocity space (see Marsh, 2001b, 2005, for a detailed review). It was originally developed by Marsh & Horne (1988) to study the accretion discs in cataclysmic variables. However its capabilities extend beyond this field. In particular, this method has been employed to study the structure in the WD gaseous discs of SDSS J1228+1040 (Manser et al., 2016a) and HE 1349–2305 (Manser et al., 2021).

We follow-up on this effort by mapping the third of the ~21 known WD gaseous debris discs (Manser et al., 2020):SDSS J1043+0855. Furthermore, with the additional spectroscopy and the refined precessional periods (see Section 5.3) we also produced updated Doppler maps of SDSS J1228+1040 and HE 1349–2305.

We used a Python wrapper [1] (Hernandez Santisteban, 2021) of the FORTRAN routines published by Spruit (1998), which implement the maximum entropy method (Skilling & Bryan, 1984). For each object we show the observed trailed spectra and

[1] Available at https://github.com/Alymantara/pydoppler

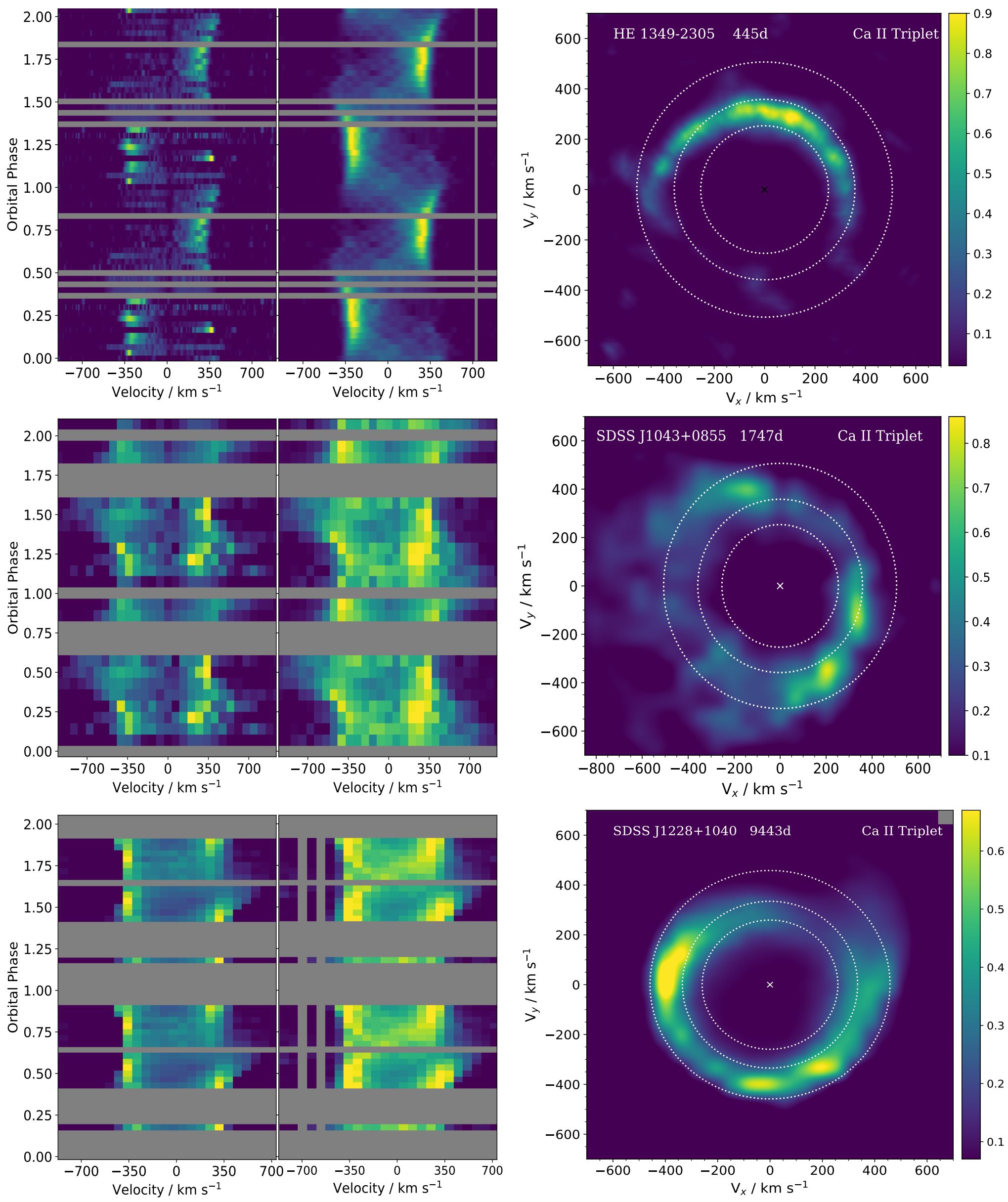

Figure 5.5: Left: Observed trailed spectra. Middle: Trailed spectra reconstructed from the tomography. Right: Doppler Tomography images in velocity space, with the x indicating the center of mass, The dotted white circles indicate the location of material in a Keplerian orbit around the centre of mass, with observed orbital radii, $R \sin^2 i$, of 0.64 (the outermost ring in velocity space), 1.2 and 2 (the innermost ring) $R_{\odot}$. The colorbar indicates the intensity of the normalised flux. The resulting images of the objects are arranged from top to bottom in ascending order of the found precession periods: HE 1349–2305 ($P \simeq 1.2$ yrs), SDSS J1043+0855 ($P \simeq 4.8$ yrs), and SDSS J1228+1040 ($P \simeq 25$ yrs).

the trailed spectra reconstructed from the tomography. We discuss the tomography of each object below.

HE 1349–2305

The tomography of HE 1349–2305 (Fig. 5.5) shows an asymmetric pattern compatible with those computed in Manser et al. (2021), who interpreted it as being caused by a fixed precessing structure. The observed trailed spectra make manifest the dramatic asymmetry of the line profiles, which changes from a fully blue- to fully red-dominated emission (and vice versa) in a small fraction of the precessional cycle. This is well reproduced by the Doppler map, as shown in the reconstructed trailed spectra.

As discussed in Manser et al. (2016a), a weakly constrained variability period can cause artifacts in the tomography, causing it to appear stretched or with unexpected discontinuities for Keplerian trayectories. Due to the better phase coverage, our measured period (445 d; Section 5.3) produces a slightly less angular image with less discontinuities than those from (Manser et al., 2021), particularly in the top right quadrant. This suggests that if indeed stable, our assumed period indeed represents a refining from previous measurements.

SDSS J1043+0855

The first publised tomography of SDSS J1043+0855 (see Fig 5.5) exhibits especially strong emission in the top quadrants centred at $V_x \sim -150$ and $V_x \sim 400$; and in the left bottom quadrant centred at $V_x \sim 300$ and $V_x \sim -200$. It shows a discontinuity appearing in-between the lower quadrant emission, likely being a spurious feature caused from a weakly constrained period. The periodogram in Section 5.3 also displayed a complex structure suggesting that our selected period is not optimal. We recommend further observations to obtain a more precise period measurement.

Nonetheless, despite the need for stricter constraints on the periodicity, the tomography's overall structure resembles that of SDSS J1228+1040. Furthermore, the observed trailed spectra is well recovered by the tomography (see Fig. 5.5). A particular characteristic visible in the trailed spectra is that at phases ~ 0.25 and ~ 0.50 the emission extends to high velocities of $\sim 700\,\mathrm{km\,s^{-1}}$. This can also be appreciated in Fig. 5.2, whereby some spectra develop a shoulder structure in the wings opposite of the dominating peak (e.g. 2020-03, 2022-04, 2025-04). This behaviour is not displayed by the other objects at the same degree: SDSS J1228+1040 shows the red wing reaching velocities of $\sim 500\,\mathrm{km\,s^{-1}}$at phase ~ 0.50, and HE 1349–2305 does not show any hint of extended wings.

SDSS J1228+1040

Our computed tomography of SDSS J1228+1040 (see Fig. 5.5) bears uncanny resemblance to that published in (Manser et al., 2016a). This is not surprising, since the overall structure of the tomography remains unaffected for periods in the range of $\simeq 24-25$ yrs. The observed trailed spectra is well reproduced by the tomography except for the enhanced feature at phase ~ 0.65 crossing from the blue to red wing. This is likely caused from the amorphous high-velocity component visible in the top-right quadrant, suggestive of a spurious nature.

5.5 Discussion

5.5.1 Structure Probing with Doppler Tomography

The use of Doppler tomography to understand the architecture and evolution of WD gaseous debris discs is still at a preliminary stage. Yet, its potential has already been made evident. Our updated tomography of all three objects presented here show non-symmetric emission consistent with previous findings (Manser et al., 2016a, 2019). The results from this small sample suggest the asymmetric tomography structure is quite common among gaseous discs displaying morphological variability. As stated befor, due to the short-cadence variability found in SDSS J1228+1040 (Manser et al., 2019), the asymmetric tomography structure could indicate a planetesimal in an precessing eccentric orbit within the dust disc.

The morphological variability of the emission lines, however, is not homogeneous throughout the sample. The long range of precessional periods has sparked debate as to whether the variability in the sample is caused by the same physical phenomena (Dennihy et al., 2018), further prompted by the non-detection of short-cadence variability in HE 1349–2305 and the short life-expectancy of the gaseous disc eccentricity ($\simeq$ 100 yrs, Miranda & Rafikov, 2018; Goksu et al., 2024). Furthermore, the morphological changes within the small sample are diverse. As an example, the double-peaked lines of SDSS J1043+0855 develop a shoulder extending to high velocities on the wing opposite to the dominating peak; a behaviour not clearly detected in the other objects. the tomography images are all consistent within each other. While this similarity favours a common origin across the small sample, we recommended further spectral observations to improve the quality of the tomographies. If indeed the same mechanism causes the variability in all

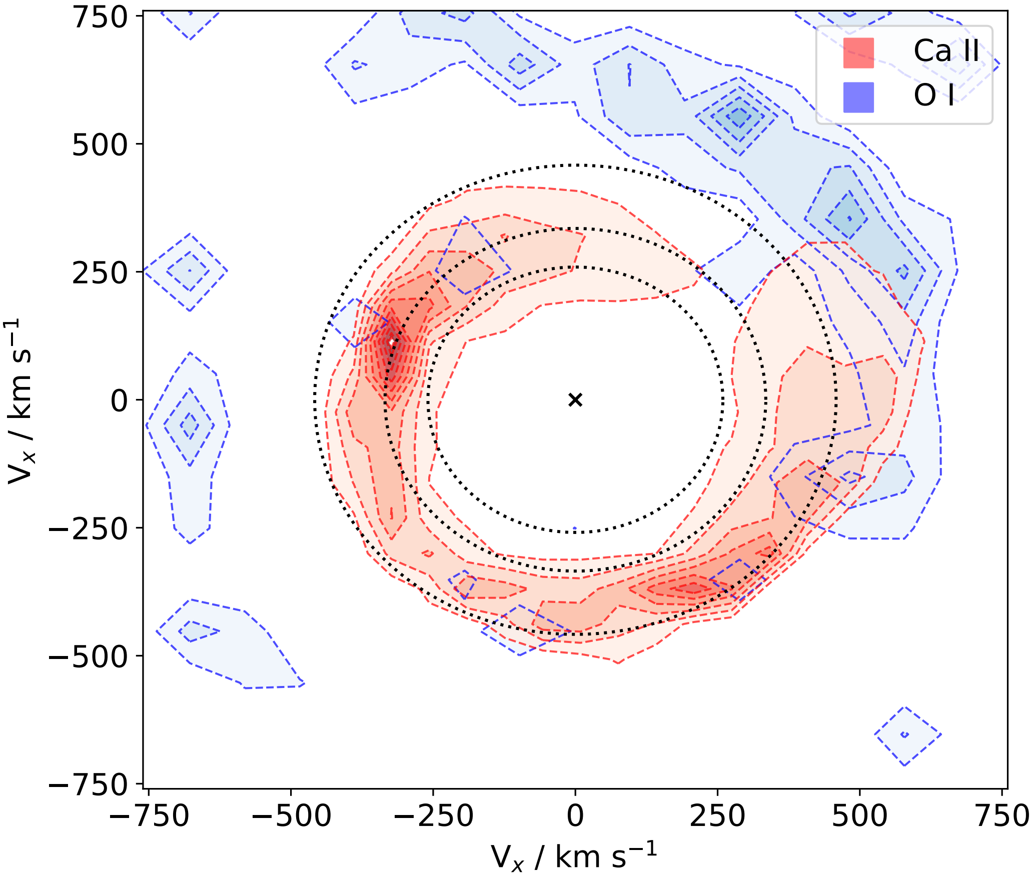

Figure 5.6: Top contours of the Ca II 8542 tomography (red) of SDSS J1228+1040 overlaid with the O I 8446 Å(blue). This configuration is indicative of anti-phase behaviour from these emission lines. The tomography shows that the oxygen line emits at higher velocities, i.e, closer to the white dwarf; in agreement with the higher thermal excitation energy of the O I transition.

three objects, a theoretical framework must account for the different evolution in morphology of the line profiles.

5.5.2 Different Species in the Gaseous Disc

Different elements have been observed to co-orbit (Melis et al., 2020), implicating a mixed structure. With this in mind, we investigated the distribution of species within the disc of SDSS J1228+1040, given that the O I 8446 Å emission line, while weaker than the Ca II Triplet, is also detected in its spectra. Analogous to Manser (2018), we computed the O I tomography with our measured period (1747 d, Section 5.3)) and the additional spectra (see Fig. 5.6). Its tomography shows a slightly

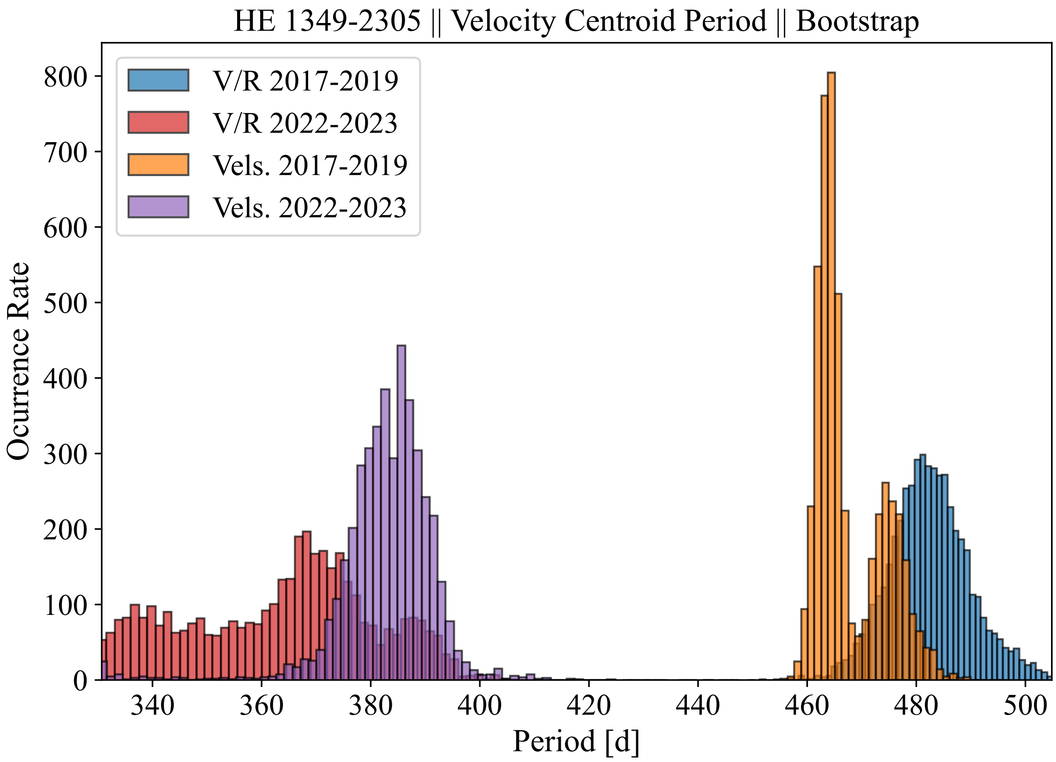

Figure 5.7: Histogram of the strongest periods in the bootstrap samples of the velocity centroids/V-over-R ratios from the 2017-2019 (gold/blue) and 2022-2023 (purple/red) intervals. The two intervals show a clear period difference of $\simeq 80\,$d, suggestive of a dramatic period variation occurring on a time-scale of $\simeq 1$ precessional period.

elongated structure, which could be due to a slightly different variational period of the O I line, or a simple artifact caused by its much lower signal-to-noise ratio. It is notable that the O I is similar in asymmetry to that of the Ca II Triplet. However, the O I emission changes in antiphase with respect to the Ca II Triplet and appears in higher velocities. This implies the Oxygen line is being emitted closer to the white dwarf, which would be expected if considering the higher thermal excitation energy of the O I transition.

This result does not imply a stratified structure, but it demonstrates the potential of Doppler tomography to disentangle the origin of different species within the disc.

5.5.3 Stability of the Precessional Period

Given the relatively short precessional cycle of HE 1349–2305 (Dennihy et al., 2018; Manser et al., 2021), this object is the perfect laboratory to explore period stability in gaseous debris discs. For this purpose we divided the data in two subsets: the first spanning from 2016-08 to 2019-06; and the second from 2022-03 to 2023-08. We then calculated the periodograms of the bootstrap samples of each of the subsets (following the methodology from Section 5.3) and selected the period with highest power for the velocity centroids and the V/R ratios (see Fig. 5.7). We note that our selected subsets contain enough data points to compute a sensible periodogram and are separated from each other by a time-lapse of the order of the precessional cycle ($\simeq 1.2$ yrs).

The velocities from the 2017-2019 epoch show a bimodal distribution with peaks at $\simeq$ 464 and $\simeq$ 470 d, in good agreement with the periods calculated in Manser et al. (2021). The V/R ratios of this same epoch exhibit a peak at a slightly longer period of $\simeq$ 480 d, with the distribution strongly overlapping with that of the velocity centroids. On the other hand the velocities from 2022-2023 peak at a period of $\simeq$ 382 d. The V/R's in this interval show a somewhat broad and uniform distribution with a peak at $\simeq$ 370 d.

Assuming gaussian distributions, the V/R's and velocities of each of the epochs overlap within 3σ, indicative of consistency of the independent measurements. However, when comparing the different epochs, taking the peaks of the distributions at face value implies a dramatic precessional period change of $\simeq$ 80 d in less than $\simeq$ 1.5 yrs. However, its worth noting that the data from the 2022-2023 epoch do not show spectra representative of the full precessional cycle; in particular, blue-peaked phases were not observed in this interval (see Fig. 5.1). Therefore, more observations are recommended in order to improve the precision of the subset periodograms. We therefore adopt a conservative approach and use the precessional period of the complete set (445 ± 3 d) for the Doppler tomography computation in Section 5.4.

5.6 Conclusions

Our small sample of Doppler tomography represents the start of an effort to map the gas discs of a statistically significant population, aimed at understanding the emission distribution of these WD gaseous debris discs. We report the first tomography of SDSS J1043+0855, and present updated images of HE 1349–2305 and SDSS J1043+0855. Our Doppler tomography is overall consistent with those produced by Manser et al. (2016a) and Manser et al. (2021). They all show an asymmetric structure, likely caused by the apsidal precession of the gaseous component. We also used Doppler tomography to explore the origin of different species within the disc of SDSS J1228+1040 and found that the O I emission originates closer than the WD and the Ca II Triplet.

In order to compute the tomography, we made the first measurement of the precessional period of SDSS J1043+0855 and obtained refined measurements for those of SDSS J1228+1040 and HE 1349–2305. Our precessional periods hold consistency with theoretical expectations (Miranda & Rafikov, 2018) and previous measurements (Manser et al., 2016a, 2021). Its worth mentioning the already wide range of precessional periods ($\simeq$1.2-25 yrs) and diversity in morphological evolution of our small sample, for which a theoretical framework must account for.

With multiple observed epochs throughout various precessional cycles, we were able to probe the stability of the precession period on HE 1349–2305. We found a dramatic change of $\simeq$80 d occurring after $\simeq$1 precessional cycle. However, we recommend further observations before conclusively stating an unstable period.

Finally, we insist on the importance of continuing the on-going long-time observational effort, with regular spectroscopic monitoring in order to increase the orbital coverage and improve the quality of the Doppler tomography.

Chapter 6

Conclusions and Future Work

"Go, little book, from this my solitude! I cast thee on the waters—go thy ways!"

Robert Southey

In this thesis I have studied three cases of accreting WDs, all of which have important contributions to their respective type. In this chapter, I highlight the conclusions drawn from each case as well as future work that can supplement the accomplished results.

The first case study was V3101 Cyg (Chapter 3), a catalcysmic variable that went into outburst in 2019 after a long period ($\gtrsim$ 50 yrs) of quiescence. Using HST COS observations, the mass of the WD was directly measured, being amongst the lowest ($\simeq 0.47\,\mathrm{M}_{\odot}$) within the CV population (Pala et al., 2020). In conjunction to the mass ratio obtained from superhump-period excess (Tampo et al., 2020), a donor mass of $\simeq 0.041\,\mathrm{M}_{\odot}$ was derived, thus making V3101 Cyg the only known CV with a low-mass WD and substellar donor. Retrieving archival photometry I measured the effective temperature of the components during quiescence yielding low values of $T_{\mathrm{eff,wd,q}} \simeq 7500\,\mathrm{K}$ and $T_{\mathrm{eff,bd,q}} \simeq 1300\,\mathrm{K}$, for the white dwarf and companion, respectively. MESA modelling using these parameters distinctively favours a detached BD+WD progenitor, over the standard MS channel. This makes this object the best candidate known to date to observationally confirm the long-predicted BD+WD descendants.

Future work regarding V3101 Cyg requires infrared observations to directly measure the mass of the companion (e.g. Hamilton et al., 2011), as opposed to that derived indirectly from the superhump periods. Although high sensitivity instrumentation is suggested for dwarf novae (Dhillon et al., 2000).

As explained in Section 3.2.2, the luminosity of V3101 Cyg has not yet reached its pre-outburst levels. Therefore, continuous monitoring of this object can be elucidating. Specifically, time-resolved optical spectroscopy is recommended to produce Doppler tomography as the disc recovers its secular quiescent stage (Section 2.4 and Chapter 5); analogous to the work by Tovmassian et al. (2022), who produced tomograms at different stages of the superoutburst of the WZ Sge object V455 And, showing an evolving disc structure (see their Fig. 7).

In Chapter 4, I studied an accreting WD with a likely mass ratio far more extreme ($\lesssim$0.012) than that in CVs with brown dwarf donors: WD 0141–675. This is a WD that attracted attention after being declared the first astrometric detection of a WD planet with a period of $P \simeq 33.65$ d and a mass of $M \simeq 9.26 M_{\rm Jup}$ (Holl et al., 2023), but was retracted not long afterwards. I conducted two independent studies to search for a possible modulation: (1) a radial velocity analysis and (2) a violet-over-red line profile analysis. Both methods yielded a weak, but consistent period of $\simeq$ 16 d, which intriguinly coincides with half the period of the retracted astrometric detection. Taking these tentative signal at face value, combined with previously published infrared constraints (Rogers et al., 2024a), implies a close-in giant planetary companion (e.g. Vanderburg et al., 2020) with low binary inclination. If confirmed, this study demonstrates that ESPRESSO observations are well capable of detecting short-period (days to weeks) giant planets around WDs. Furthermore, at $\simeq$ 9 pc, WD 0141–675 would become the closest known planet around a WD.

However, further work for WD 0141–675, requires strengthening the signal detection, since my reported period signals have a high false-alarm probability. To this effect, follow-up ESPRESSO spectroscopy could confirm the signals. And while the sensitivity at the wavelength range of *Spitzer* and *WISE* were insufficient for an excess detection, the Mid-InfraRed Instrument on the *JWST* is expected to readily find the excess with its longer wavelength capabilities (5.6-25.5μm) (Rogers et al., 2024a). This sensitivity suitability was made evident for the close-in giant planet WD 1856+534 b (Limbach et al., 2025b) orbiting a cool WD of similar characteristics to WD 0141–675.

Finally, when planets or planetesimals are perturbed within the tidal disruption radius, they become shredded into dusty (Swan et al., 2019, 2021) and gaseous discs (e.g. Manser et al., 2016b, 2020). In particular the gaseous discs typically show the Ca II triplet in emission (Gänsicke et al., 2006b), which typically displays variability in both morphology and strength, in timescales of years to decades. In Chapter 5, I analysed optical spectroscopy from various instruments of three warm ($\sim$20 000)WDs hosting gaseous debris discs. Two of them have constraints on their periods and have been mapped with Doppler tomography (SDSS J1228+1040, HE 1349–2305, Manser et al., 2016a, 2021). With follow-up X-Shooter spectroscopy I updated their period measurements and re-computed their tomography. Furthermore, I computed the first tomography image of SDSS J1043+0855 (Gänsicke et al., 2007).

All three images are consistent with previous results in exhibiting a non-symmetric emission in velocity space, suggestive of a common origin. The diversity of variability periods ($\simeq$1.2-25 yrs) have sparked debate on the driving physical phenomena. A planetesimal detected within the disc of SDSS J1228+1040, prompted the idea that the variability period might be caused by the precession of the orbit (Manser et al., 2019), naturally explaining the diversity in periods. This agrees with theoretical predictions that model the emission variability with relativistic precession of an eccentric structure (Miranda & Rafikov, 2018; Goksu et al., 2024). These models, however, assume fixed precessional cycles. I tested the stability of the variability on HE 1349–2305, whose short period ($\simeq$1.2 yrs) allowed to take two subsets separated by at least a precessional cycle. My analysis shows a dramatic decrease of $\simeq$ 80 d in the period, although its causes remain unknown. Further observations of this object should help constrain this period variability and shed light on the matter.

Future work in WD gas discs would require follow-up spectroscopy of the mapped objects, to improve the quality of the tomography. This further observations should also help to impose stricter constraints on the precessional cycles and probe for their stability; additionally sufficient time-resolved spectroscopy of the rest of WD gas discs is also recommended, in order to increase the reduced sample of Doppler mapped objects. Finally, the use of the code CLOUDY (Ferland et al., 1998) can be used to model the composition of the circumstellar material and compare it with the photospheric metal abundances, analogous to the work done by Gänsicke et al. (2019) and Xu et al. (2024).

Overall this work highlights the use of standard methods in spectroscopy across diverse sub-fields of accreting white dwarfs. A perfect example of this is Doppler Tomography, capable of extracting information either from cataclysmic variables (see Section 2.4.1) or discs made from disruption events of planetesimals (Chapter 5). Likewise, modulation analyses were made on all the systems to impose constraints on the periods, which prove invaluable in understanding their architecture and evolution. The results in this thesis make evident the link between white dwarfs with accreting companions, regardless of the nature of the donor.

Bibliography

Abazajian K. N., et al., 2009, ApJS, 182, 543

Alexandrov S., Ivanova J., Dankov K., 2026, New Astron. Rev., 102, 101736

Althaus L. G., Córsico A. H., Isern J., García-Berro E., 2010, Astron. Astrophys. Rev., 18, 471

Althaus L. G., Miller Bertolami M. M., Córsico A. H., 2013, Astron. Astrophys., 557, A19

Amantayeva A., Zharikov S., Page K. L., Pavlenko E., Sosnovskij A., Khokhlov S., Ibraimov M., 2021, Astrophys. J., 918, 58

Angulo C., et al., 1999, Nuclear Physics A, 656, 3

Armitage P., 2010, in American Astronomical Society Meeting Abstracts #216. p. 108.01

Arney G., et al., 2026, arXiv e-prints, p. arXiv:2601.09766

Astropy Collaboration et al., 2022, Astrophys. J., 935, 167

Augusteijn T., van der Hooft F., de Jong J. A., van Paradijs J., 1996, Astron. Astrophys., 311, 889

Baluev R. V., 2008, Mon. Not. R. Astron. Soc., 385, 1279

Barber S. D., Belardi C., Kilic M., Gianninas A., 2016, Mon. Not. R. Astron. Soc., 459, 1415

Barstow M. A., Barstow J. K., Casewell S. L., Holberg J. B., Hubeny I., 2014, MNRAS, 440, 1607

Bauer E. B., Bildsten L., 2018, ApJ Lett., 859, L19

Baumeister P., et al., 2025, Space Sci. Rev., 221, 123

Bédard A., 2024, Astrophys. Space Sci., 369, 43

Belloni D., Schreiber M. R., 2023a, in , Handbook of X-ray and Gamma-ray Astrophysics. p. 129, doi:10.1007/978-981-16-4544-0˙98-1

Belloni D., Schreiber M. R., 2023b, Astron. Astrophys., 678, A34

Belloni D., Schreiber M. R., Zorotovic M., Iłkiewicz K., Hurley J. R., Giersz M., Lagos F., 2018, Mon. Not. R. Astron. Soc., 478, 5626

Belloni D., Schreiber M. R., Pala A. F., Gänsicke B. T., Zorotovic M., Rodrigues C. V., 2020, Mon. Not. R. Astron. Soc., 491, 5717

Berger L., Koester D., Napiwotzki R., Reid I. N., Zuckerman B., 2005, A&A, 444, 565

Berger T. A., Schlieder J. E., Huber D., 2026, Astron. J., 171, 23

Bernstein R., Shectman S. A., Gunnels S. M., Mochnacki S., Athey A. E., 2003, in Iye M., Moorwood A. F. M., eds, Society of Photo-Optical Instrumentation Engineers (SPIE) Conference Series Vol. 4841, Instrument Design and Performance for Optical/Infrared Ground-based Telescopes. pp 1694–1704, doi:10.1117/12.461502

Beuermann K., Burwitz V., Reinsch K., Schwope A., Thomas H. C., 2020, Astron. Astrophys., 634, A91

Bhattacharjee S., et al., 2025, Publ. Astron. Soc. Pac., 137, 074202

Blondin S., 2026, in Encyclopedia of Astrophysics, Volume 3. pp 404–422 (`arXiv:2411.09740`), doi:10.1016/B978-0-443-21439-4.00101-2

Bodenheimer P., Pollack J. B., 1986, Icarus, 67, 391

Bonsor A., 2026, in Encyclopedia of Astrophysics. pp 564–572, doi:10.1016/B978-0-443-21439-4.00020-1

Bonsor A., Veras D., 2015, MNRAS, 454, 53

Brinkworth C. S., Gänsicke B. T., Marsh T. R., Hoard D. W., Tappert C., 2009, ApJ, 696, 1402

Brinkworth C. S., Gänsicke B. T., Girven J. M., Hoard D. W., Marsh T. R., Parsons S. G., Koester D., 2012, ApJ, 750, 86

Bryant J., 2005, Plotting the Roche Potential Surface of a Cataclysmic Binary Star System

Buchan A. M., Tremblay P.-E., Bédard A., Bauer E. B., Cunningham T., 2025, Mon. Not. R. Astron. Soc., 544, 2098

Burleigh M. R., et al., 2006, MNRAS, 373, 1416

Camisassa M. E., Althaus L. G., Córsico A. H., Vinyoles N., Serenelli A. M., Isern J., Miller Bertolami M. M., García–Berro E., 2016, Astrophys. J., 823, 158

Camisassa M. E., Althaus L. G., Rohrmann R. D., García-Berro E., Torres S., Córsico A. H., Wachlin F. C., 2017, Astrophys. J., 839, 11

Camisassa M. E., et al., 2019, Astron. Astrophys., 625, A87

Camisassa M., Fuentes J. R., Schreiber M. R., Rebassa-Mansergas A., Torres S., Raddi R., Dominguez I., 2024, Astron. Astrophys., 691, L21

Carroll B. W., Ostlie D. A., 1996, An Introduction to Modern Astrophysics

Casewell S. L., et al., 2018, Mon. Not. R. Astron. Soc., 476, 1405

Casewell S. L., et al., 2020, Mon. Not. R. Astron. Soc., 497, 3571

Cassan A., et al., 2012, Nat, 481, 167

Cassisi S., Potekhin A. Y., Pietrinferni A., Catelan M., Salaris M., 2007, Astrophys. J., 661, 1094

Cauley P. W., Farihi J., Redfield S., Bachman S., Parsons S. G., Gänsicke B. T., 2018, Astrophys. J. Lett., 852, L22

Chandrasekhar S., 1931, Astrophys. J., 74, 81

Chandrasekhar S., 1935, MNRAS, 95, 207

Chayer P., Dupuis J., 2010, in Werner K., Rauch T., eds, 17$^{\text{th}}$ European White Dwarf Workshop. No. 1273 in AIP Conf. Ser.. AIP, pp 394–399

Chen X., Han Z., Tout C. A., 2011, Astrophys. J. Lett., 735, L31

Cherepashchuk A. M., 2022, Astronomy Reports, 66, S412

Chin C.-W., Chiu H.-Y., Stothers R., 1966, Astron. J., 71, 380

Chomiuk L., Metzger B. D., Shen K. J., 2021, Annu. Rev. Astron. Astrophys., 59, 391

Chugunov A. I., Dewitt H. E., Yakovlev D. G., 2007, Phys. Rev. D, 76, 025028

Clavier S., Rey M., Buldyreva J., 2026, J. Quant. Spectrosc. Radiat. Transf., 350, 109758

Comins N., Kaufmann W., eds, 1999, Discovering the universe. Freeman, New York

Coutu S., Dufour P., Bergeron P., Blouin S., Loranger E., Allard N. F., Dunlap B. H., 2019, ApJ, 885, 74

Crumpler N. R., et al., 2024, Astrophys. J., 977, 237

Cunningham T., Tremblay P.-E., Freytag B., Ludwig H.-G., Koester D., 2019, MNRAS, 488, 2503

Cunningham T., et al., 2025, Mon. Not. R. Astron. Soc., 540, 633

Cyburt R. H., et al., 2010, Astrophys. J. Suppl. Ser., 189, 240

D'Antona F., Mazzitelli I., 1990, Annu. Rev. Astron. Astrophys., 28, 139

Debes J. H., Kilic M., 2010, in Werner K., Rauch T., eds, AIP Conf. Proc. Vol. 1273, 17th European White Dwarf Workshop. Am. Inst. Phys., New York, p. 488

Debes J. H., Sigurdsson S., 2002, ApJ, 572, 556

Debes J. H., Kilic M., Faedi F., Shkolnik E. L., Lopez-Morales M., Weinberger A. J., Slesnick C., West R. G., 2012, ApJ, 754, 59

Dekker H., D'Odorico S., Kaufer A., Delabre B., Kotzlowski H., 2000, in Iye M., Moorwood A. F., eds, Society of Photo-Optical Instrumentation Engineers (SPIE) Conference Series Vol. 4008, Optical and IR Telescope Instrumentation and Detectors. pp 534–545

Dennihy E., Debes J. H., Dunlap B. H., Dufour P., Teske J. K., Clemens J. C., 2016, ApJ, 831, 31

Dennihy E., Clemens J. C., Dunlap B. H., Fanale S. M., Fuchs J. T., Hermes J. J., 2018, ApJ, 854, 40

Dennihy E., et al., 2020, Astrophys. J., 905, 5

Dewi J. D. M., Tauris T. M., 2000, A&A, 360, 1043

Dhillon V. S., Littlefair S. P., Howell S. B., Ciardi D. R., Harrop-Allin M. K., Marsh T. R., 2000, MNRAS, 314, 826

Doyle A. E., et al., 2023, Astrophys. J., 950, 93

Drew J. E., et al., 2005, Mon. Not. R. Astron. Soc., 362, 753

Duncan M. J., Lissauer J. J., 1998, Icarus, 134, 303

Dunlap B. H., Clemens J. C., 2015, in Dufour P., Bergeron P., Fontaine G., eds, Astronomical Society of the Pacific Conference Series Vol. 493, 19th European Workshop on White Dwarfs. p. 547

Dupuis J., Fontaine G., Pelletier C., Wesemael F., 1993, ApJS, 84, 73

Duquennoy A., Mayor M., 1991, A&A, 248, 485

Echevarría J., et al., 2019, Revista Mexicana de Astronomia y Astrofisica, 55, 21

Eggleton P. P., 1983, Astrophys. J., 268, 368

Eisenstein D. J., et al., 2006, ApJS, 167, 40

El-Badry K., Rix H.-W., 2018, MNRAS, 480, 4884

Ely J., Bourque M., Debes J., Kriss G., McCullough P. R., 2015, in IAU General Assembly. p. 2258383

Farihi J., 2009, MNRAS, 398, 2091

Farihi J., 2016, New Astron. Rev., 71, 9

Farihi J., Christopher M., 2004, AJ, 128, 1868

Farihi J., Becklin E. E., Zuckerman B., 2005, ApJS, 161, 394

Farihi J., Jura M., Zuckerman B., 2009, ApJ, 694, 805

Farihi J., Brinkworth C. S., Gänsicke B. T., Marsh T. R., Girven J., Hoard D. W., Klein B., Koester D., 2011, ApJ Lett., 728, L8

Farihi J., Gänsicke B. T., Steele P. R., Girven J., Burleigh M. R., Breedt E., Koester D., 2012, MNRAS, 421, 1635

Farihi J., Gänsicke B. T., Koester D., 2013, Science, 342, 218

Farihi J., et al., 2018, Mon. Not. R. Astron. Soc., 481, 2601

Farihi J., et al., 2022, MNRAS, 511, 1647

Feline W. J., Dhillon V. S., Marsh T. R., Stevenson M. J., Watson C. A., Brinkworth C. S., 2004, MNRAS, 347, 1173

Ferguson J. W., Alexander D. R., Allard F., Barman T., Bodnarik J. G., Hauschildt P. H., Heffner-Wong A., Tamanai A., 2005, Astrophys. J., 623, 585

Ferland G. J., Korista K. T., Verner D. A., Ferguson J. W., Kingdon J. B., Verner E. M., 1998, PASP, 110, 761

Fetherolf T., Welter S. G., Ostberg C. M., Kane S. R., Barnes R., Simpson E. R., 2026, Astron. J., 171, 83

Fetzner Keniger M. A., Armstrong D., Brogi M., Gandhi S., Lafarga M., 2025, RAS Techniques and Instruments, 4, rzaf041

Figueira P., et al., 2025, Astron. Astrophys., 700, A174

Fontaine G., 2001, in von Hippel T., Simpson C., Manset N., eds, Astronomical Society of the Pacific Conference Series Vol. 245, Astrophysical Ages and Times Scales. p. 173

Frazer E. M., Sankrit R., Fischer W., 2024, The Spectral Extraction Reference Files for COS/FUV G130M at LP5 and G140L/800 at LP3, Instrument Science Report COS 2024-17, 36 pages

Freedman R., Kaufmann W. J., 2002, Universe, 6th edition

Freedman R. S., Marley M. S., Lodders K., 2008, Astrophys. J. Suppl. Ser., 174, 504

Freedman R. S., Lustig-Yaeger J., Fortney J. J., Lupu R. E., Marley M. S., Lodders K., 2014, Astrophys. J. Suppl. Ser., 214, 25

Freudling W., Romaniello M., Bramich D. M., Ballester P., Forchi V., García-Dabló C. E., Moehler S., Neeser M. J., 2013, A&A, 559, A96

Frewen S. F. N., Hansen B. M. S., 2014, MNRAS, 439, 2442

Fuller G. M., Fowler W. A., Newman M. J., 1985, Astrophys. J., 293, 1

Gagnier D., Leidi G., Vetter M., Andrassy R., Röpke F. K., 2026, arXiv e-prints, p. arXiv:2601.04188

Gaia Collaboration et al., 2021, Astron. Astrophys., 649, A1

Gaia Collaboration et al., 2023a, A&A, 674, A1

Gaia Collaboration et al., 2023b, A&A, 674, A34

Gänsicke B. T., 2011, in Schuh S., Drechsel H., Heber U., eds, American Institute of Physics Conference Series Vol. 1331, American Institute of Physics Conference Series. pp 211–214, doi:10.1063/1.3556202

Gänsicke B. T., Beuermann K., Thomas H. C., 1997, Mon. Not. R. Astron. Soc., 289, 388

Gänsicke B. T., Sion E. M., Beuermann K., Fabian D., Cheng F. H., Krautter J., 1999, Astron. Astrophys., 347, 178

Gänsicke B. T., Fried R. E., Hagen H.-J., Beuermann K., Engels D., Hessman F. V., Nogami D., Reinsch K., 2000, A&A, 356, L79

Gänsicke B. T., et al., 2003, ApJ, 594, 443

Gänsicke B. T., de Martino D., Marsh T. R., Haswell C. A., Knigge C., Long K. S., Shore S. N., 2006a, Astrophys. Space Sci., 306, 177

Gänsicke B. T., Marsh T. R., Southworth J., Rebassa-Mansergas A., 2006b, Science, 314, 1908

Gänsicke B. T., Marsh T. R., Southworth J., 2007, MNRAS, 380, L35

Gänsicke B. T., Koester D., Marsh T. R., Rebassa-Mansergas A., Southworth J., 2008, MNRAS, 391, L103

Gänsicke B. T., et al., 2009, Montly Notices of the Royal Astronomical Society, 397, 2170

Gänsicke B. T., Koester D., Farihi J., Girven J., Parsons S. G., Breedt E., 2012, MNRAS, 424, 333

Gänsicke B. T., Schreiber M. R., Toloza O., Fusillo N. P. G., Koester D., Manser C. J., 2019, Nat, 576, 61

Gardner J. P., et al., 2006, in Mather J. C., MacEwen H. A., de Graauw M. W. M., eds, Society of Photo-Optical Instrumentation Engineers (SPIE) Conference Series Vol. 6265, Space Telescopes and Instrumentation I: Optical, Infrared, and Millimeter. p. 62650N, doi:10.1117/12.670492

Gentile Fusillo N. P., et al., 2019, MNRAS, 482, 4570

Ghezzi L., Costa-Almeida E., Loaiza-Tacuri V., Cunha K., 2026, arXiv e-prints, p. arXiv:2601.00962

Gimeno G., et al., 2016, in American Astronomical Society Meeting Abstracts #227. p. 445.01

Girven J., Brinkworth C. S., Farihi J., Gänsicke B. T., Hoard D. W., Marsh T. R., Koester D., 2012, ApJ, 749, 154

Godon P., Sion E. M., 2022, Astrophys. J., 928, 26

Godon P., Shara M. M., Sion E. M., Zurek D., 2017, Astrophys. J., 850, 146

Goksu O. A., Kutra T., Wu Y., 2024, Astron. J., 167, 236

Goliasch J., Nelson L., 2015, Astrophys. J., 809, 80

González Hernández J. I., Pepe F., Molaro P., Santos N. C., 2018, in Deeg H. J., Belmonte J. A., eds, , Handbook of Exoplanets. p. 157, doi:10.1007/978-3-319-55333-7˙15710.1007/978-3-319-30648-3-157-1

Graham J. R., Matthews K., Neugebauer G., Soifer B. T., 1990, ApJ, 357, 216

Green M. J., et al., 2020, Mon. Not. R. Astron. Soc., 496, 1243

Grether D., Lineweaver C. H., 2006, Astrophys. J., 640, 1051

Guess A. W., 1962, Astrophys. J., 135, 855

Guidry J. A., et al., 2021, ApJ, 912, 125

Guidry J. A., et al., 2025, Astrophys. J., 992, 167

Gunn J. E., et al., 2006, Astron. J., 131, 2332

Hameury J. M., 2020, Advances in Space Research, 66, 1004

Hameury J.-M., 2025, arXiv e-prints, p. arXiv:2512.21188

Hameury J. M., Lasota J. P., 2021, Astron. Astrophys., 650, A114

Hameury J. M., Lasota J. P., Huré J. M., 1997, MNRAS, 287, 937

Hameury J. M., Lasota J. P., Warner B., 2000, A&A, 353, 244

Hamilton R. T., Harrison T. E., Tappert C., Howell S. B., 2011, Astrophys. J., 728, 16

Harlaftis E. T., Steeghs D., Horne K., Martín E., Magazzú A., 1999, Mon. Not. R. Astron. Soc., 306, 348

Harrison T. E., 2016, Astrophys. J., 816, 4

Hause C., Sion E. M., Godon P., Gänsicke B. T., Szkody P., de Martino D., Pala A., 2017, Astron. J., 154, 48

Hawley J. F., Balbus S. A., 1998, in Howell S., Kuulkers E., Woodward C., eds, Astronomical Society of the Pacific Conference Series Vol. 137, Wild Stars in the Old West. p. 273

Hayashi C., 1966, Annu. Rev. Astron. Astrophys., 4, 171

He M. Y., Ford E. B., 2026, arXiv e-prints, p. arXiv:2601.13480

Hellier C., 2001, Cataclysmic Variable Stars. Springer

Hermes J. J., et al., 2017, ApJS, 232, 23

Hernández-Díaz S., Stelzer B., Schwope A., Muñoz-Giraldo D., 2025, Astron. Astrophys., 703, A166

Hernandez Santisteban J. V., 2021, PyDoppler: Wrapper for Doppler tomography software, Astrophysics Source Code Library, record ascl:2106.003 (ascl:2106.003)

Hernández Santisteban J. V., et al., 2016, Nature, 533, 366

Hernández Santisteban J. V., Knigge C., Pretorius M. L., Sullivan M., Warner B., 2018, Mon. Not. R. Astron. Soc., 473, 3241

Hernández Santisteban J. V., et al., 2019, Monthly Notices of the Royal Astronomical Society, 486, 2631

Herwig F., Blöcker T., Langer N., Driebe T., 1999, A&A, 349, L5

Hillman Y., Prialnik D., Kovetz A., Shara M. M., 2016, Astrophys. J., 819, 168

Hintzen P., Jensen E., 1979, PASP, 91, 492

Hirose M., Osaki Y., 1990, PASJ, 42, 135

Hjellming M. S., 1989, PhD thesis, (Illinois Univ. at Urbana-Champaign, Savoy)

Holl B., et al., 2023, A&A, 674, A10

Horne K., 1985, MNRAS, 213, 129

Horne K., Marsh T. R., 1986, MNRAS, 218, 761

Horne K., Marsh T. R., Cheng F. H., Hubeny I., Lanz T., 1994, ApJ, 426, 294

Hoskin M. J., et al., 2020, MNRAS, 499, 171

Howell S. B., 2001, Publ. Astron. Soc. Jpn, 53, 675

Iben Jr. I., 1967, Annu. Rev. Astron. Astrophys., 5, 571

Iben I. J., Livio M., 1993, PASP, 105, 1373

Iglesias C. A., Rogers F. J., 1993, Astrophys. J., 412, 752

Iglesias C. A., Rogers F. J., 1996, Astrophys. J., 464, 943

Inight K., Gänsicke B. T., Breedt E., Marsh T. R., Pala A. F., Raddi R., 2021, MNRAS, 504, 2420

Inight K., et al., 2023, Mon. Not. R. Astron. Soc., 525, 3597

Isern J., García-Berro E., Külebi B., Lorén-Aguilar P., 2017, ApJ Lett., 836, L28

Itoh N., Hayashi H., Nishikawa A., Kohyama Y., 1996, Astrophys. J. Suppl. Ser., 102, 411

Ivanova N., Taam R. E., 2004, ApJ, 601, 1058

Ivanova N., et al., 2013, A&AR, 21, 59

Izquierdo P., Toloza O., Gänsicke B. T., Rodríguez-Gil P., Farihi J., Koester D., Guo J., Redfield S., 2021, Mon. Not. R. Astron. Soc., 501, 4276

Jermyn A. S., Schwab J., Bauer E., Timmes F. X., Potekhin A. Y., 2021, Astrophys. J., 913, 72

Jermyn A. S., et al., 2023, Astrophys. J. Suppl. Ser., 265, 15

Jinno T., Saitoh T. R., Funato Y., Makino J., 2026, arXiv e-prints, p. arXiv:2601.20348

Johnson T. M., Klein B. L., Koester D., Melis C., Zuckerman B., Jura M., 2022, Astrophys. J., 941, 113

Jura M., 2003, ApJ Lett., 584, L91

Jura M., 2008, AJ, 135, 1785

Jura M., Farihi J., Zuckerman B., 2007, ApJ, 663, 1285

Kato T., 2015, Publ. Astron. Soc. Jpn, 67, 108

Kato T., Osaki Y., 2013, Publ. Astron. Soc. Jpn, 65, 115

Kato T., Osaki Y., 2014, Publ. Astron. Soc. Jpn, 66, L5

Kato T., et al., 2009, PASJ, 61, 395

Kato T., et al., 2014, Publ. Astron. Soc. Jpn, 66, 90

Kausch W., et al., 2015, A&A, 576, A78

Kelson D. D., 2003, Publ. Astron. Soc. Pac., 115, 688

Kenyon S. J., Bromley B. C., 2017, ApJ, 844, 116

Kilic M., von Hippel T., Leggett S. K., Winget D. E., 2005, ApJ Lett., 632, L115

Kilic M., Bergeron P., Kosakowski A., Brown W. R., Agüeros M. A., Blouin S., 2020, Astrophys. J., 898, 84

King A. R., 1988, QJRAS, 29, 1

Kinnear T., 2011, Master's thesis, University of Warwick

Klein B. L., Doyle A. E., Zuckerman B., Dufour P., Blouin S., Melis C., Weinberger A. J., Young E. D., 2021, ApJ, 914, 61

Knigge C., 2006, Mon. Not. R. Astron. Soc., 373, 484

Knigge C., Baraffe I., Patterson J., 2011, Astrophys. J. Suppl. Ser., 194, 28

Koester D., 2009, A&A, 498, 517

Koester D., 2010, Memorie della Societa Astronomica Italiana, 81, 921

Koester D., Wolff B., 2000, A&A, 357, 587

Koester D., Schulz H., Weidemann V., 1979, Astron. Astrophys., 76, 262

Koester D., Provencal J., Shipman H. L., 1997, A&A, 320, L57

Koester D., Dreizler S., Weidemann V., Allard N. F., 1998, A&A, 338, 612

Koester D., Gänsicke B. T., Farihi J., 2014, A&A, 566, A34

Kolb U., 1993, Astron. Astrophys., 271, 149

Kolb U., Baraffe I., 1999, Mon. Not. R. Astron. Soc., 309, 1034

Kraft R. P., 1958, Astrophys. J., 127, 625

Lagos F., Schreiber M. R., Zorotovic M., Gänsicke B. T., Ronco M. P., Hamers A. S., 2021, MNRAS, 501, 676

Langanke K., Martínez-Pinedo G., 2000, Nuclear Physics A, 673, 481

Larson R. B., 2003, Reports on Progress in Physics, 66, 1651

Lasota J.-P., 2001, New Astronomy Review, 45, 449

Limbach M. A., et al., 2025a, A Search for Life Around Two Dead Stars, JWST Proposal. Cycle 4, ID. #7564

Limbach M. A., et al., 2025b, Astrophys. J. Lett., 984, L28

Lin D. N. C., Papaloizou J., 1979, Mon. Not. R. Astron. Soc., 186, 799

Littlefair S. P., Dhillon V. S., Marsh T. R., Gänsicke B. T., 2006, MNRAS, 371, 1435

Littlefair S. P., Dhillon V. S., Marsh T. R., Gänsicke B. T., Baraffe I., Watson C. A., 2007, Mon. Not. R. Astron. Soc., 381, 827

Littlefair S. P., et al., 2014, Mon. Not. R. Astron. Soc., 445, 2106

Littlefair S. P., Rodríguez-Gil P., Marsh T. R., Parsons S. G., Dhillon V. S., 2024, Mon. Not. R. Astron. Soc., 527, 4353

Livio M., Soker N., 1984, MNRAS, 208, 783

Livio M., Soker N., 1988, ApJ, 329, 764

Lodders K., 2003, Astrophys. J., 591, 1220

Lomb N. R., 1976, Astrophys. Space Sci., 39, 447

Long K. S., Gilliland R. L., 1999, Astrophys. J., 511, 916

Long K. S., Helfand D. J., Grabelsky D. A., 1981, ApJ, 248, 925

Longstaff E. S., Casewell S. L., Wynn G. A., Page K. L., Williams P. K. G., Braker I., Maxted P. F. L., 2019, Mon. Not. R. Astron. Soc., 484, 2566

Madurga Favieres C., Kissler-Patig M., Xu S., Bonsor A., 2024, Astron. Astrophys., 688, A168

Malamud U., 2026, in Encyclopedia of Astrophysics, Volume 1. pp 553–563 (arXiv:2403.07427), doi:10.1016/B978-0-443-21439-4.00001-8

Malamud U., Perets H. B., 2020, MNRAS, 492, 5561

Malamud U., Grishin E., Brouwers M., 2021, Mon. Not. R. Astron. Soc., 501, 3806

Manser C. J., 2018, PhD thesis, University of Warwick

Manser C. J., et al., 2016a, MNRAS, 455, 4467

Manser C. J., Gänsicke B. T., Koester D., Marsh T. R., Southworth J., 2016b, MNRAS, 462, 1461

Manser C. J., et al., 2019, Science, 364, 66

Manser C. J., Gänsicke B. T., Gentile Fusillo N. P., Ashley R., Breedt E., Hollands M., Izquierdo P., Pelisoli I., 2020, MNRAS, 493, 2127

Manser C. J., et al., 2021, MNRAS, 508, 5657

Marchant P., 2026, in Encyclopedia of Astrophysics. pp 264–278, doi:10.1016/B978-0-443-21439-4.00072-9

Marsh T. R., 1989, PASP, 101, 1032

Marsh T. R., 2001a, in Lázaro F. C., Arévalo M. J., eds, , Vol. 563, Binary Stars: Selected Topics on Observations and Physical Processes. p. 151

Marsh T. R., 2001b, in Boffin H. M. J., Steeghs D., Cuypers J., eds, , Vol. 573, Astrotomography, Indirect Imaging Methods in Observational Astronomy. p. 1, doi:10.48550/arXiv.astro-ph/0011020

Marsh T. R., 2005, Astrophys. Space Sci., 296, 403

Marsh T. R., Horne K., 1988, MNRAS, 235, 269

Marsh T. R., Dhillon V. S., Duck S. R., 1995, MNRAS, 275, 828

Matsuda T., Sekino N., Shima E., Sawada K., Spruit H., 1990, Astron. Astrophys., 235, 211

Maxted P. F. L., Napiwotzki R., Dobbie P. D., Burleigh M. R., 2006, Nature, 442, 543

Mayor M., Queloz D., 1995, Nat, 378, 355

McAllister M., et al., 2019, Mon. Not. R. Astron. Soc., 486, 5535

McCleery J., et al., 2020, Mon. Not. R. Astron. Soc., 499, 1890

Melis C., Dufour P., 2017, ApJ, 834, 1

Melis C., Jura M., Albert L., Klein B., Zuckerman B., 2010, ApJ, 722, 1078

Melis C., et al., 2012, ApJ Lett., 751, L4

Melis C., Klein B., Doyle A. E., Weinberger A., Zuckerman B., Dufour P., 2020, Astrophys. J., 905, 56

Metzger B. D., Rafikov R. R., Bochkarev K. V., 2012, MNRAS, 423, 505

Metzger B. D., Zenati Y., Chomiuk L., Shen K. J., Strader J., 2021, Astrophys. J., 923, 100

Mineshige S., Osaki Y., 1985, Publ. Astron. Soc. Jpn, 37, 1

Miranda R., Rafikov R. R., 2018, ApJ, 857, 135

Muñoz-Giraldo D., Stelzer B., Schwope A., 2024, Astron. Astrophys., 687, A305

Nelemans G., Tout C. A., 2005, MNRAS, 356, 753

Nelemans G., Verbunt F., Yungelson L. R., Portegies Zwart S. F., 2000, A&A, 360, 1011

Nelson L., Schwab J., Ristic M., Rappaport S., 2018, Astrophys. J., 866, 88

Neustroev V. V., Mäntynen I., 2023, Mon. Not. R. Astron. Soc., 523, 6114

Neustroev V. V., Zharikov S. V., 2020, Astron. Astrophys., 642, A100

Neustroev V. V., Zharikov S. V., Borisov N. V., 2016, Astron. Astrophys., 586, A10

Neustroev V., et al., 2019, The Astronomer's Telegram, 13009, 1

O'Brien M. W., et al., 2024, Mon. Not. R. Astron. Soc., 527, 8687

O'Donoghue D., 1990, Mon. Not. R. Astron. Soc., 246, 29

Ochem E., Marrocchi Y., 2026, Icarus, 445, 116859

Oda T., Hino M., Muto K., Takahara M., Sato K., 1994, Atomic Data and Nuclear Data Tables, 56, 231

Offner S. S. R., Moe M., Kratter K. M., Sadavoy S. I., Jensen E. L. N., Tobin J. J., 2023, in Inutsuka S., Aikawa Y., Muto T., Tomida K., Tamura M., eds, Astronomical Society of the Pacific Conference Series Vol. 534, Protostars and Planets VII. p. 275 (arXiv:2203.10066), doi:10.48550/arXiv.2203.10066

Ogilvie G. I., 2002, Mon. Not. R. Astron. Soc., 330, 937

Osterman S., et al., 2011, Astrophys. Space Sci., 335, 257

Paczyński B., 1971, ARA&A, 9, 183

Paczyński B., 1967, Acta Astron., 17, 287

Paczyński B., 1971, Annu. Rev. Astron. Astrophys., 9, 183

Paczynski B., 1976, in Eggleton P., Mitton S., Whelan J., eds, IAU Symposium Vol. 73, Structure and Evolution of Close Binary Systems. p. 75

Pala A. F., et al., 2017, Mon. Not. R. Astron. Soc., 466, 2855

Pala A. F., et al., 2019, Mon. Not. R. Astron. Soc., 483, 1080

Pala A. F., et al., 2020, Mon. Not. R. Astron. Soc., 494, 3799

Pala A. F., et al., 2022, Mon. Not. R. Astron. Soc., 510, 6110

Palla F., Stahler S. W., 1999, Astrophys. J., 525, 772

Paquette C., Pelletier C., Fontaine G., Michaud G., 1986a, ApJS, 61, 177

Paquette C., Pelletier C., Fontaine G., Michaud G., 1986b, Astrophys. J. Suppl. Ser., 61, 197

Parsons S. G., et al., 2017, Mon. Not. R. Astron. Soc., 471, 976

Parsons S. G., et al., 2025, Mon. Not. R. Astron. Soc., 537, 2112

Parsons S. G., et al., 2026, Mon. Not. R. Astron. Soc.,

Pasquini L., Pala A. F., Salaris M., Ludwig H. G., Leão I., Weiss A., de Medeiros J. R., 2023, Mon. Not. R. Astron. Soc., 522, 3710

Patterson J., 1984, Astrophys. J. Suppl. Ser., 54, 443

Patterson J., 2011, Mon. Not. R. Astron. Soc., 411, 2695

Patterson J., Zuckerman B., Becklin E. E., Tholen D. J., Hawarden T., 1991, Astrophys. J., 374, 330

Patterson J., et al., 2005, PASP, 117, 1204

Patterson J., Thorstensen J. R., Knigge C., 2008, PASP, 120, 510

Paxton B., Bildsten L., Dotter A., Herwig F., Lesaffre P., Timmes F., 2011, Astrophys. J. Suppl. Ser., 192, 3

Paxton B., et al., 2013, Astrophys. J. Suppl. Ser., 208, 4

Paxton B., et al., 2015, Astrophys. J. Suppl. Ser., 220, 15

Paxton B., et al., 2018, Astrophys. J. Suppl. Ser., 234, 34

Paxton B., et al., 2019, Astrophys. J. Suppl. Ser., 243, 10

Payne M. J., Veras D., Holman M. J., Gänsicke B. T., 2016, MNRAS, 457, 217

Payne M. J., Veras D., Gänsicke B. T., Holman M. J., 2017, MNRAS, 464, 2557

Peacock S., et al., 2025, Astron. J., 170, 293

Pepe F., et al., 2021, A&A, 645, A96

Phillips M. W., et al., 2020, Astron. Astrophys., 637, A38

Pineda J. S., Bellotti S., Villadsen J., Vidotto A., Morin J., Folsom C. P., 2026, Astrophys. J., 997, 172

Planquart L., Jorissen A., Van Winckel H., 2025, Astron. Astrophys., 694, A85

Politano M., 2004, Astrophys. J., 604, 817

Politano M., Weiler K. P., 2007, ApJ, 665, 663

Pols O. R., Tout C. A., Eggleton P. P., Han Z., 1995, Mon. Not. R. Astron. Soc., 274, 964

Postnov K. A., Yungelson L. R., 2014, Living Reviews in Relativity, 17, 3

Potekhin A. Y., Chabrier G., 2010, Contributions to Plasma Physics, 50, 82

Pringle J. E., Wade R. A., 1985, Astronomy Express, 1, 159

Raddi R., Gänsicke B. T., Koester D., Farihi J., Hermes J. J., Scaringi S., Breedt E., Girven J., 2015, MNRAS, 450, 2083

Rafikov R. R., 2011a, MNRAS, 416, L55

Rafikov R. R., 2011b, ApJ Lett., 732, L3

Rafikov R. R., Garmilla J. A., 2012, ApJ, 760, 123

Raghavan D., et al., 2010, Astrophys. J. Suppl. Ser., 190, 1

Ramírez S. H., Echevarría J., 2021, Mon. Not. R. Astron. Soc., 508, 665

Ramírez S. H., Segura Montero O., Michel R., Echevarría J., 2022, Rev. Mexicana Astron. Astrofis., 58, 47

Ramírez S. H., Gänsicke B. T., Koester D., Lafarga M., Gentile-Fusillo N. P., 2025, Mon. Not. R. Astron. Soc., 539, 2884

Rappaport S., Joss P. C., Webbink R. F., 1982, ApJ, 254, 616

Rappaport S., Verbunt F., Joss P. C., 1983, Astrophys. J., 275, 713

Rappaport S., et al., 2017, Mon. Not. R. Astron. Soc., 471, 948

Rebassa-Mansergas A., Nebot Gómez-Morán A., Schreiber M. R., Girven J., Gänsicke B. T., 2011, MNRAS, 413, 1121

Ritter H., 1976, MNRAS, 175, 279

Ritter H., 1988, Astron. Astrophys., 202, 93

Ritter H., Burkert A., 1986, A&A, 158, 161

Ritter H., Kolb U., 1998, A&AS, 129, 83

Ritter H., Kolb U., 2003, A&A, 404, 301

Rocchetto M., Farihi J., Gänsicke B. T., Bergfors C., 2015, MNRAS, 449, 574

Rodriguez A. C., et al., 2025, Publ. Astron. Soc. Pac., 137, 014201

Rogers F. J., Nayfonov A., 2002, Astrophys. J., 576, 1064

Rogers L. A., Seager S., 2010, ApJ, 712, 974

Rogers L. K., et al., 2024a, MNRAS, 527, 977

Rogers L. K., et al., 2024b, Mon. Not. R. Astron. Soc., 532, 3866

Rogers L. K., et al., 2025, Mon. Not. R. Astron. Soc., 542, 293

Rolland B., Bergeron P., Fontaine G., 2018, Astrophys. J., 857, 56

Rosenbush A., 2020a, arXiv e-prints, p. arXiv:2007.10480

Rosenbush A., 2020b, arXiv e-prints, p. arXiv:2007.11025

Rybicki K. R., Denis C., 2001, Icarus, 151, 130

Sabach E., Hillel S., Schreier R., Soker N., 2017, Mon. Not. R. Astron. Soc., 472, 4361

Sala G., Brandenstein C., Baum S., Graham P. W., 2026, Phys. Rev. D, 113, 123022

Salpeter E. E., 1961, Astrophys. J., 134, 669

Saumon D., Chabrier G., van Horn H. M., 1995, Astrophys. J. Suppl. Ser., 99, 713

Saumon D., Blouin S., Tremblay P.-E., 2022, Phys. Rep., 988, 1

Savedoff M. P., van Horn H. M., Vila S. C., 1969, Astrophys. J., 155, 221

Savoury C. D. J., et al., 2011, MNRAS, 415, 2025

Scargle J. D., 1982, Astrophys. J., 263, 835

Schaefer B. E., 2023, Mon. Not. R. Astron. Soc., 524, 3146

Schatzman E., 1948, Nat, 161, 61

Schenker K., 2005, in ASP Conf. Ser. 334: 14th European Workshop on White Dwarfs. p. 351

Schenker K., Kolb U., Ritter H., 1998, MNRAS, 297, 633

Schenker K., King A. R., Kolb U., Wynn G. A., Zhang Z., 2002, MNRAS, 337, 1105

Schneider D. P., Young P., 1980, ApJ, 240, 871

Schreiber M. R., Zorotovic M., Wijnen T. P. G., 2016, Mon. Not. R. Astron. Soc., 455, L16

Schreiber M. R., Belloni D., van Roestel J., 2023, Astron. Astrophys., 679, L8

Schreiber M. R., Belloni D., Schwope A. D., 2024, Astron. Astrophys., 682, L7

Schröder K., Connon Smith R., 2008, MNRAS, 386, 155

Schwarzenberg-Czerny A., 1996, ApJ Lett., 460, L107

Shafter A. W., 1985, in Lamb D. Q., Patterson J., eds, Cataclysmic Variables and Low-Mass X-ray Binaries. p. 355, doi:10.1007/978-94-009-5319-2˙43

Shafter A. W., Szkody P., Thorstensen J. R., 1986, ApJ, 308, 765

Shakura N. I., Sunyaev R. A., 1973, A&A, 24, 337

Shariat C., El-Badry K., 2026, arXiv e-prints, p. arXiv:2601.00439

Shen K. J., Quataert E., 2022, Astrophys. J., 938, 31

Shields A. L., Wolf E. T., Agol E., Tremblay P.-E., 2025, Astrophys. J., 979, 45

Shu F. H., Lizano S., Adams F. C., 1987, in Peimbert M., Jugaku J., eds, IAU Symposium Vol. 115, Star Forming Regions. pp 417–433

Siess L., 2007, Astron. Astrophys., 476, 893

Skilling J., Bryan R. K., 1984, Mon. Not. R. Astron. Soc., 211, 111

Smak J., 1971, Acta Astron., 21, 15

Smette A., et al., 2015, A&A, 576, A77

Soderblom D. R., 2023, in , Vol. 15, COS Instrument Handbook v. 15.0. STScI, p. 15

Sokoloski J. L., 2003, JAAVSO, 31, 89

Solheim J.-E., 2010, Publ. Astron. Soc. Pac., 122, 1133

Southworth J., Gänsicke B. T., Marsh T. R., de Martino D., Aungwerojwit A., 2007, MNRAS, 378, 635

Spruit H. C., 1998, arXiv e-prints, pp astro–ph/9806141

Spruit H. C., Matsuda T., Inoue M., Sawada K., 1987, Mon. Not. R. Astron. Soc., 229, 517

Steeghs D., Harlaftis E. T., Horne K., 1997, Mon. Not. R. Astron. Soc., 290, L28

Steeghs D., Marsh T., Knigge C., Maxted P. F. L., Kuulkers E., Skidmore W., 2001, ApJ Lett., 562, L145

Steele P. R., Burleigh M. R., Dobbie P. D., Jameson R. F., Barstow M. A., Satterthwaite R. P., 2011, MNRAS, 416, 2768

Sullivan K., Dattilo A., Batalha N. M., 2026, Astron. J., 171, 53

Sun Q., 2026, Astrophys. J. Suppl. Ser., 282, 37

Swan A., Farihi J., Wilson T. G., 2019, MNRAS, 484, L109

Swan A., Kenyon S. J., Farihi J., Dennihy E., Gänsicke B. T., Hermes J. J., Melis C., von Hippel T., 2021, Mon. Not. R. Astron. Soc., 506, 432

Szkody P., 1985, AJ, 90, 1837

Szkody P., et al., 2011, AJ, 142, 181

Tampo Y., et al., 2020, Publ. Astron. Soc. Jpn, 72, 49

Tappert C., Gänsicke B. T., Schmidtobreick L., Ribeiro T., 2011, Astron. Astrophys., 532, A129

Thorstensen J. R., Fenton W. H., Patterson J. O., Kemp J., Krajci T., Baraffe I., 2002, Astrophys. J. Lett., 567, L49

Timmes F. X., Swesty F. D., 2000, Astrophys. J. Suppl. Ser., 126, 501

Tobin J. J., et al., 2022, Astrophys. J., 925, 39

Toloza O., et al., 2016, Mon. Not. R. Astron. Soc., 459, 3929

Toloza O., et al., 2023, The Messenger, 190, 4

Toulhoat H., Zgonnik V., 2022, Astrophys. J., 924, 83

Tovmassian G., Gänsicke B. T., Echevarria J., Zharikov S., Ramirez A., 2022, Astrophys. J., 939, 14

Townsley D. M., Bildsten L., 2002, in Gänsicke B. T., Beuermann K., Reinsch K., eds, Astronomical Society of the Pacific Conference Series Vol. 261, The Physics of Cataclysmic Variables and Related Objects. p. 31 (arXiv:astro-ph/0112267), doi:10.48550/arXiv.astro-ph/0112267

Townsley D. M., Bildsten L., 2003, ApJ Lett., 596, L227

Townsley D. M., Gänsicke B. T., 2009, Astrophys. J., 693, 1007

Trifonov T., 2026, in Encyclopedia of Astrophysics, Volume 1. pp 320–341 (arXiv:2410.11424), doi:10.1016/B978-0-443-21439-4.00022-5

Truran J. W., Starrfield S. G., Strittmatter P. A., Wyatt S. P., Sparks W. M., 1977, Astrophys. J., 211, 539

Tutukov A., Yungelson L., 1979, in Conti P. S., De Loore C. W. H., eds, IAU Symposium Vol. 83, Mass Loss and Evolution of O-Type Stars. pp 401–406

Unger N., Ségransan D., Barbato D., Delisle J.-B., Sahlmann J., Holl B., Udry S., 2023, Astron. Astrophys., 680, A16

Uthas H., Knigge C., Long K. S., Patterson J., Thorstensen J., 2011, Mon. Not. R. Astron. Soc., 414, L85

Valencia D., Sasselov D. D., O'Connell R. J., 2007, ApJ, 665, 1413

VanderPlas J. T., 2018, Astrophys. J. Suppl. Ser., 236, 16

Vanderbosch Z., et al., 2020, ApJ, 897, 171

Vanderbosch Z. P., et al., 2021, ApJ, 917, 41

Vanderburg A., et al., 2015, Nat, 526, 546

Vanderburg A., et al., 2020, Nat, 585, 363

Veras D., 2021, in , Oxford Research Encyclopedia of Planetary Science. p. 1, doi:10.1093/acrefore/9780190647926.013.238

Veras D., Gänsicke B. T., 2015, MNRAS, 447, 1049

Veras D., Leinhardt Z. M., Bonsor A., Gänsicke B. T., 2014, MNRAS, 445, 2244

Veras D., Leinhardt Z. M., Eggl S., Gänsicke B. T., 2015, MNRAS, 451, 3453

Vernet J., et al., 2011, A&A, 536, A105

Villaver E., Livio M., 2007, ApJ, 661, 1192

Vogt N., Krzeminski W., Sterken C., 1980, A&A, 85, 106

Warner B., 2003, Cataclysmic Variable Stars. Cambridge University Press, doi:10.1017/CBO9780511586491

Warner B., Nather R. E., 1971, Mon. Not. R. Astron. Soc., 152, 219

Webb N. A., 2023, arXiv e-prints, p. arXiv:2303.10055

Webb N. A., et al., 2020, Astron. Astrophys., 641, A136

Webbink R. F., 1984, Astrophys. J., 277, 355

Werner M. W., 2005, Advances in Space Research, 36, 1048

Whitehurst R., 1988, Mon. Not. R. Astron. Soc., 232, 35

Wijnen T. P. G., Zorotovic M., Schreiber M. R., 2015, Astron. Astrophys., 577, A143

Wildi F., Chazelas B., Pepe F., 2012, in McLean I. S., Ramsay S. K., Takami H., eds, Society of Photo-Optical Instrumentation Engineers (SPIE) Conference Series Vol. 8446, Ground-based and Airborne Instrumentation for Astronomy IV. p. 84468E, doi:10.1117/12.926841

Williams R. E., 1980, Astrophys. J., 235, 939

Williams J. T., Gänsicke B. T., Swan A., O'Brien M. W., Izquierdo P., Cutolo A.-M., Cunningham T., 2024, Astron. Astrophys., 691, A352

Williams J. T., et al., 2025, Mon. Not. R. Astron. Soc., 541, 1377

Wilson D. J., Gänsicke B. T., Koester D., Raddi R., Breedt E., Southworth J., Parsons S. G., 2014, MNRAS, 445, 1878

Wilson D. J., Gänsicke B. T., Koester D., Toloza O., Pala A. F., Breedt E., Parsons S. G., 2015, MNRAS, 451, 3237

Winters J. G., et al., 2019, Astron. J., 157, 216

Witham A. R., et al., 2006, Mon. Not. R. Astron. Soc., 369, 581

Witham A. R., Knigge C., Drew J. E., Greimel R., Steeghs D., Gänsicke B. T., Groot P. J., Mampaso A., 2008, Mon. Not. R. Astron. Soc., 384, 1277

Wolf W. M., Bildsten L., Brooks J., Paxton B., 2013, ApJ, 777, 136

Wolszczan A., Frail D. A., 1992, Nat, 355, 145

Wright J. T., 2018, in Deeg H. J., Belmonte J. A., eds, , Handbook of Exoplanets. p. 4, doi:10.1007/978-3-319-55333-7˙4

Wright E. L., et al., 2010, AJ, 140, 1868

Wynn G. A., King A. R., Horne K., 1997, Mon. Not. R. Astron. Soc., 286, 436

Xu S., Jura M., 2014, Astrophys. J. Lett., 792, L39

Xu S., Jura M., Dufour P., Zuckerman B., 2016, ApJ Lett., 816, L22

Xu S., et al., 2018, ApJ, 866, 108

Xu S., et al., 2024, Astron. J., 167, 248

Yarza R., Everson R. W., Ramirez-Ruiz E., 2022, arXiv e-prints, p. arXiv:2210.00010

Yarza R., et al., 2023, Astrophys. J., 954, 176

York D. G., et al., 2000, AJ, 120, 1579

Zhu W., Dong S., 2021, Annu. Rev. Astron. Astrophys., 59, 291

Zorotovic M., Schreiber M. R., Gänsicke B. T., Nebot Gómez-Morán A., 2010, A&A, 520, A86

Zorotovic M., Schreiber M. R., Gänsicke B. T., 2011, Astron. Astrophys., 536, A42

Zuckerman B., Becklin E. E., 1987, Nat, 330, 138

Zuckerman B., Koester D., Reid I. N., Hünsch M., 2003, ApJ, 596, 477

Zuckerman B., Koester D., Melis C., Hansen B. M., Jura M., 2007, ApJ, 671, 872

Zuckerman B., Melis C., Klein B., Koester D., Jura M., 2010, ApJ, 722, 725

de Kool M., 1990, Astrophys. J., 358, 189 de Wit J., et al., 2025, Research Notes of the American Astronomical Society, 9, 270

van Horn H. M., 1968, Astrophys. J., 151, 227

van Maanen A., 1917, PASP, 29, 258

van den Heuvel E. P. J., Bhattacharya D., Nomoto K., Rappaport S. A., 1992, A&A, 262, 97